國立臺灣大學工學院材料科學與工程學系暨研究所

博士論文

Department of Materials Science and Engineering
College of Engineering
National Taiwan University
Doctoral Dissertation

層間反對稱交互作用: 物理行為以及三維磁元件的自旋工程

Interlayer Dzyaloshinskii-Moriya interaction: Physical behaviors and spin engineering in three-dimensional devices

黃宇豪

Yu-Hao Huang

指導教授：白奇峰 博士

Advisor: Chi-Feng Pai, Ph.D.

中華民國 113 年 7 月

July, 2024

doi:10.6342/NTU202404434

國立臺灣大學博士學位論文
口試委員會審定書
DOCTORAL DISSERTATION ACCEPTANCE CERTIFICATE
NATIONAL TAIWAN UNIVERSITY

（論文中文題目）
(Chinese title of Doctor's Thesis)
層間反對稱交互作用：物理行為以及三維磁元件的自旋工程

（論文英文題目）
(English title of Doctor's Thesis)
Interlayer Dzyaloshinskii-Moriya interaction: Physical behaviors and spin engineering in three-dimensional devices

本論文係 **黃宇豪** f08527069 在國立臺灣大學 材料科學與工程學系 完成之博士學位論文，於民國 113 年 07 月 18 日承下列考試委員審查通過及口試及格，特此證明。

The undersigned, appointed by the Department / Graduate Institute of Materials Science and Engineering on 18 July 2024 have examined a Doctoral Dissertation entitled above presented by **Yu-Hao Huang** f08527069 candidate and hereby certify that it is worthy of acceptance.

口試委員
Oral examination committee:

白奇峰 白奇峰
（指導教授 Advisor）

徐斌睿 徐斌睿

許紘瑋 許紘瑋

黃斯衍 黃斯衍

曲丹茹 曲丹茹

系（所、學位學程）主管 Director：蔡豐羽 蔡豐羽

doi:10.6342/NTU202404434

誌謝

2019 年初的春天，我從台大材料系畢業。誠心而言，當時對未來的想像充滿著不確定。四年半的大學生涯中，材料系教授的學科不少，對首重通用教育的大學生而言卻著重在廣博，無法達到精深。我始終認為選擇一個有趣、有前景的主題深入了解是十分必要的，作為自己學術上的”一技之長”，更能加入競爭力強的高科技產業。

加入白奇峰教授的 SCREAM Team 是無心之舉，因為大學初期迷茫了一段時期，我並沒有設定自己應該在特定哪個領域做研究，而是秉持著只要能有一番建樹，能在業界立足就功德圓滿了。從結果而言，選擇白老師的實驗室可說是無心插柳，轉瞬間五年過去了，而在經過了一個豐富充實的研究生生涯已經抵達學業的末端，我站在博士學位的門前。與學士生涯相比能有如此大的轉變，我必須感謝 SCREAM Team 的所有人，白老師上課時曾講了一句肺腑之言:”學習與做研究總是痛苦的”。這句話啟發我至深，遇到挫折與失敗時不再陷入沮喪與絕望的矛盾螺旋。無論在碩士還是博士期間，挫折仍然沒有離開我，但與之相對的，步步前行的經驗都成了我的助力，最終成功在研究這條路上有所斬獲。

首先要致謝的人是實驗室大家長白奇峰老師。在我對研究方向仍然懵懂時提供研究方向並在與我的交流中提出諸多建議，尤其是老師祥和的態度，讓人能以最舒適的態度待在這個大家庭中，激盪出有趣又重要的結果。實驗室的陳天玥、陳宗奕學長在我研究生涯初期提供莫大助力，建議了我首先以 L-MOKE 為基礎的方向，雖然起初挫折之多令我措手不及，但我在架設儀器的難關攻克中對實驗運作、資料處理以及 DC/lock-in 儀器原理有深入的了解。這些經驗對我博士的研究助益極多。感謝胡宸瑜以及劉彥廷學長在諸多實驗想法中的建議與交流，以及他們不吝分享關於自旋軌道矩效率提升，以及 type-*x* 系統中的實驗以及模擬的奧妙。我在兩位前輩睿智獨到的思路、各自的狂野人生故事以及經驗中獲益良多。感謝廖唯邦學長，沒有他作為領頭人實驗室就會重重卡關，同時也在很多實驗架構、可行性上給了我寶貴的建議。感謝與韓瑞旭、MIT 大佬黃兆中、Max Plank 強者李永誠的合作文章中多次的腦力激盪，沒有他們，諸多 Interlayer DMI 的研究就不可能完整。特別是有了兆中聯手 MIT 的蔡佳晉與冠豪處理需要深度學習才能校正的向量磁鐵，才有

doi:10.6342/NTU202404434

機會一窺 Interlayer DMI 的各種特性。我同樣要感謝蕭佑展，在我苦手的程式上面提出建議，讓資料處理以及實驗介面的更動成為可能(可見分工也是研究重要的一部分)。感謝詩哲、建平、東岳、俊逸等人與我分享各自的成果，我獲益良多，實驗室也因為你們而能融洽歡樂，順利進行。

我必須感謝一路支持我的家人、女友。謝謝父母在我逃避時的理解與鼓勵，讓我能走到當今一步，謝謝女友的陪伴，有個溫暖的傾聽者。我最後再次感謝白奇峰老師的指導，有他們才有我的研究生涯，才能有這論文。

中文摘要

近年來，Dzyaloshinskii-Moriya 交互作用（DMI）因其在產生非共線鐵磁性方面的關鍵作用而受到了不少關注，它在手性磁域壁的形成以及穩定斯格明子等拓撲結構等情況中至關重要。科學家們已經探索了各種創新性的想法，嘗試通過電流來操縱這些具有 DMI 結構，以期創造可行的基於自旋的賽道/邏輯元件。不過，由於薄膜的堆疊順序可以自然產生垂直平面的對稱性破缺，DMI 至今主要被限制於介面的情況中。在這篇論文中，我將展示如何通過引入一個平面內的對稱性破缺，將 DMI 擴充到一個新穎的（IL-DMI）的情況。在這個系統中，被一個非磁性的間隔層分開的兩個磁化量會因 IL-DMI 而傾向垂直排列。

首先，我在具有正交磁化量的磁多層膜系統中觀察到了不低的 IL-DMI。通過利用特殊設計的變角度的磁場掃描，在實驗中觀察到了 IL-DMI 的反對稱性質及其飽和行為。利用反常霍爾效應（AHE）和橫向磁光克爾效應（L-MOKE）探測分別具有垂直磁化（PMA）和平面內磁化（IMA）的兩個鐵磁層，我在驗證了 IL-DMI 的對稱性的同時計算了 IL-DMI 的強度。透過同時觀測兩個鐵磁層並在實驗上證明兩者同時發生磁化翻轉的行為，我展示了如何通過 IL-DMI 將針對特定磁化的操縱轉移到與其正交的另一個鐵磁層上。

隨後，我對不同對稱性破缺要素的有效性進行了研究。首先，我將 IL-DMI 的重要性與 PMA 層中的傾斜磁各向異性進行了比較，這兩種效應由於在材料成長中使用了斜角沉積（OAD）而會共存於磁薄膜中。我接著通過 IMA 和 PMA 的磁化翻轉特性的比較確認了 IL-DMI 的重要性。其次，與 OAD 不同，我研究了實現平面內對稱性破缺的另一種方法：在外加的平面場 H_{ext} 下進行樣品生長。我確認了雖

doi:10.6342/NTU202404434

然 OAD 和使用 H_{ext} 都能在 IMA 層中產生磁各向異性，但基於磁異向性的的對稱性破壞對 IL-DMI 的強度和方向幾無影響，這強烈暗示了 IL-DMI 的起源是結構性的。

接著通過利用多個 OAD 膜層，我發現了 IL-DMI 的整體強度和方向是由各個楔形層的貢獻所決定。這些獨立貢獻與總體強度之間明顯的線性關係，以及觀察到的相反特徵方向都啟發了我，發展了基於 Fert-Lévy 三位元點模型的玩具模型。此一模型可以良好的整合實驗結果並解釋 IL-DMI 的物理起源。此外，通過適當的 OAD 設計策略，可以抑制由 OAD 引起的空間不均勻性的同時最小化對 IL-DMI 強度的降低，對元件的實用化有益。最後，我明確展示了當相互作用由 Ru 傳導時，IL-DMI 強度有明顯的阻尼振盪行為。根據理論預測的擬和得出約 1 納米的振盪週期證實了理論預測，即 DMI 是 RKKY 相互作用的一個附加項。

關鍵字：自旋電子學、磁化翻轉、賈洛申斯基-守谷交換作用、楔型沉積、人工反鐵磁、磁性隨機存取記憶體

Abstract

In recent years, Dzyaloshinskii-Moriya interaction (DMI) has garnered enormous attention for its pivotal role in facilitating noncollinear magnetism, such as the formation of chiral domain walls and stabilizing topologically distinct structures like magnetic skyrmions. Various innovative proposals have been explored to manipulate these DMI mediated structures via electric currents, to create viable spin-based racetrack/logic devices. Thus far, DMI has primarily been confined to an interfacial case due to the out-of plane symmetry breaking naturally generated by the film's stacking order. In this dissertation, I showcase that by introducing an in-plane symmetry breaking element, DMI can be extended to a novel interlayer scenario (IL-DMI). Here, perpendicular alignment of spins is mediated between two discrete magnetizations, separated by a nonmagnetic spacer.

Firstly, sizable IL-DMI is observed within a multilayer system with orthogonal magnetic orientations. The antisymmetric nature of IL-DMI and its saturating behavior are both experimentally observed utilizing an angle-dependent field-scan protocol. The directionality of IL-DMI is confirmed to obey the symmetry pointed out by Moriya. By probing both perpendicularly magnetized (PMA) and in-plane magnetized (IMA) layers via anomalous Hall effect (AHE) and longitudinal magneto-optical Kerr effect (L-MOKE), respectively, the reciprocity of IL-DMI is verified, with the strength of IL-DMI estimated. Particularly, supported by the coherent switching of both IMA and PMA magnetizations, I demonstrate how manipulation of one magnetization can be transposed to an orthogonal axis through IL-DMI.

The efficacy of different symmetry breaking factors are subsequently investigated.

First, the importance of IL-DMI is compared to the tilted magnetic anisotropy in the PMA layer where both effects coexist due to the oblique angle deposition (OAD). Their relative magnitudes are evaluated, affirming the importance of IL-DMI by comparing the IMA and PMA switching characteristics. Secondly, in contrast to the OAD process, we investigate an alternative means of achieving in-plane symmetry breaking: sample growth under an external in-plane field H_{ext}. It's concluded that while both OAD and H_{ext} can induce magnetic anisotropy in the IMA layer, magnetically based symmetry breaking factor has a negligible impact on IL-DMI's strength and direction. This strongly suggests that the origin of IL-DMI is structural.

Lastly, by exploiting multiple OAD opportunities, I unveil the overall strength and direction of IL-DMI to be governed by individual wedged layer's contributions. The evident linearity, and the opposite characteristic directions observed among these individual contributions inspired the development of a toy model based on the Fert-Lévy three site model. This model can explain the physical origin of the IL-DMI while incorporating experimental findings. Furthermore, by implementing proper OAD design strategies, spacial inhomogeneity created by OAD can be suppressed while minimizing the reduction in IL-DMI strength. Finally, I definitively showcase a damped oscillation of IL-DMI when the interaction is mediated by Ru, a conventional Ruderman-Kittel-Kasuya-Yoshida (RKKY) interaction spacer. The identical oscillation period of ~ 1 nm confirms the theoretical prediction that DMI arises from an additional term in RKKY interaction.

Keywords: Spintronics, Magnetization switching, Dzyaloshinskii-Moriya interaction, Wedge deposition, synthetic antiferromagnets, Magnetic random-access memory

CONTENTS

doi:10.6342/NTU202404434

LIST OF FIGURES

doi:10.6342/NTU202404434

doi:10.6342/NTU202404434

doi:10.6342/NTU202404434

LIST OF TABLES

doi:10.6342/NTU202404434

Chapter 1 Introduction

1.1 Exchange interactions

The concept of exchange is fundamental to understanding the magnetic properties of materials. These interactions arise from the interplay between the quantum mechanical principle governing electron behavior, namely, the Pauli exclusion principle (since electrons are Fermions), and the Coulomb repulsion. In an intuitive picture, a single electron exerts an “exchange void” around its vicinity, repelling other electrons with an identical spin due to the Pauli exclusion principle [1]. Regardless of the various types of exchange, different exchange interactions govern the spin alignment in magnetism, including ferromagnetic, antiferromagnetic, ferrimagnetic or even more exotic configurations, in which one branch of them will be the main focus of this thesis. Fig. 1-1 provides an overview of the various exchange interactions based on whether the coupling length is short enough such that there’s significant overlap between their wavefunctions, or on the contrary, over large distances.

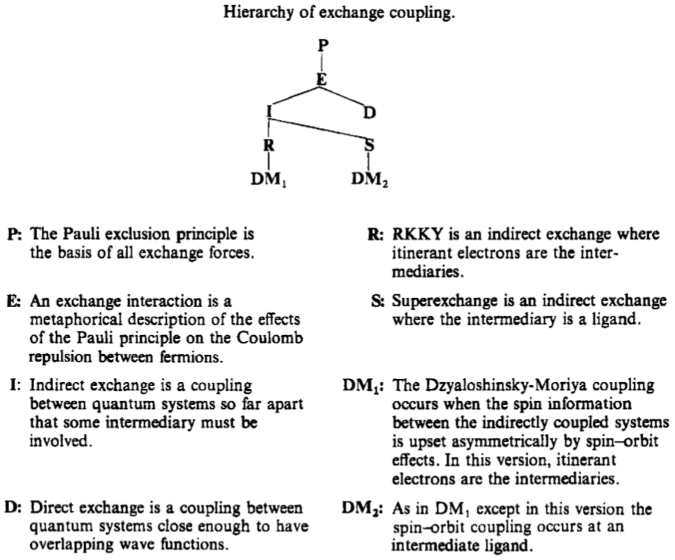

Hierarchy of exchange coupling.

P: The Pauli exclusion principle is the basis of all exchange forces.

E: An exchange interaction is a metaphorical description of the effects of the Pauli principle on the Coulomb repulsion between fermions.

I: Indirect exchange is a coupling between quantum systems so far apart that some intermediary must be involved.

D: Direct exchange is a coupling between quantum systems close enough to have overlapping wave functions.

R: RKKY is an indirect exchange where itinerant electrons are the intermediaries.

S: Superexchange is an indirect exchange where the intermediary is a ligand.

DM_1: The Dzyaloshinsky-Moriya coupling occurs when the spin information between the indirectly coupled systems is upset asymmetrically by spin–orbit effects. In this version, itinerant electrons are the intermediaries.

DM_2: As in DM_1 except in this version the spin–orbit coupling occurs at an intermediate ligand.

Fig. 1-1 Hierarchy of various exchange interactions. Reprinted from [1]

doi:10.6342/NTU202404434

1.1.1 Direct Exchange

If a system with two identical electrons is considered, its Hamiltonian must be invariant under a permutation which means the spatial wavefunction must be either symmetric or antisymmetric. Furthermore, due to the Pauli exclusion principle, the total wavefunction (including the spatial part and the spin part) must be antisymmetric. As a result, if the spatial part of the wavefunction is symmetric (or bonding), then the spin part must be antisymmetric, represented by the singlet $1/\sqrt{2}(\uparrow\downarrow-\downarrow\uparrow)$ (arrows representing the spin up/down of the electrons). On the other hand, for an antisymmetric (anti-bonding) spatial part, the spin part is symmetric, represented by the triplet $\{\uparrow\uparrow,\ \downarrow\downarrow,\ 1/\sqrt{2}(\uparrow\downarrow+\downarrow\uparrow)\}$. Overall, the singlet has total spin $S = 0$ (corresponding to spin magnetic quantum number $m_s = 0$) while the triplet has $S = 1$ (corresponding to $m_s = \{-1, 0, +1\}$). We can write the energies corresponding to the singlet and triplet as $E_\mathrm{S} = \int\Psi_\mathrm{s}^* \widehat{H}\Psi_\mathrm{s} d\mathbf{r}_1 d\mathbf{r}_2$ and $E_\mathrm{T} = \int\Psi_\mathrm{T}^* \widehat{H}\Psi_\mathrm{T} d\mathbf{r}_1 d\mathbf{r}_2$, respectively ($\Psi_\mathrm{s}$ and Ψ_T are the total wavefunctions). Subsequently, the difference between these two energies can be parametrized by $\mathbf{S}_1 \cdot \mathbf{S}_2$. This is demonstrated as follows. If considering a joint entity, the total spin is represented by

$$\mathbf{S}^{\mathrm{tot}} = \mathbf{S}_1 + \mathbf{S}_2 \tag{1.1}$$

so that

$$(\mathbf{S}^{\mathrm{tot}})^2 = (\mathbf{S}_1)^2 + (\mathbf{S}_2)^2 + 2\,\mathbf{S}_1 \cdot \mathbf{S}_2 \tag{1.2}$$

Since $S = 0$ or 1, the eigenvalue value of $(\mathbf{S}^{\mathrm{tot}})^2$ is $S(S+1)\hbar^2$, and the eigenvalues of both $(\mathbf{S}_1)^2$ and $(\mathbf{S}_2)^2$ are $3\hbar^2/4$ (both $\mathbf{S}_1$ and $\mathbf{S}_2$ have $s = 1/2$ individually), the expectation value of $\mathbf{S}_1 \cdot \mathbf{S}_2$ for the singlet and triplet state is therefore $-3\hbar^2/4$ and $\hbar^2/4$, respectively. We can

doi:10.6342/NTU202404434

subsequently write the spin dependent term of the Hamiltonian as [2]

$$\widehat{H}_{\text{eff}} = \frac{1}{4}(E_{\text{S}} + 3E_{\text{T}}) - \frac{1}{\hbar^2}(E_{\text{S}} - E_{\text{T}})\,\mathbf{S}_1 \cdot \mathbf{S}_2 \tag{1.3}$$

It's verifiable that eqn. (1.3) leads to $\widehat{H}_{\text{eff}} = E_{\text{T}}$ for the anti-bonding (triplet) state and $\widehat{H}_{\text{eff}} = E_{\text{S}}$ for the singlet state. In addition, the first part of eqn.(1.3) is a constant that can be absorbed into other energy terms, leaving the second part as the spin-dependent term. Hence, the spin dependent Hamiltonian is further simplified to

$$\widehat{H}_{\text{eff}} = -2J\,\mathbf{S}_1 \cdot \mathbf{S}_2 \tag{1.4}$$

Where $J = [(E_{\text{S}} - E_{\text{T}})/2]\hbar^2$ is the exchange constant. When $J > 0$ the triplet (antibonding) state is favored, and when $J < 0$ the singlet (bonding) state is favored. Note that if the two electrons are on the same atom, J is usually positive leading to an antisymmetric spatial state. This is in fact the Hund's first rule, where parallel spins are spatially apart to minimize the Coulomb repulsion.

While eqn. (1.4) only applies to a system of two electrons (spins), and generalizing it to describe a many-body system is an extremely difficult process, it nonetheless motivates the development of the Heisenberg model by recognizing that the relationship shared between two spins as described by eqn. (1.4) likely applies to all neighboring spins, resulting in [3]

$$\widehat{H} = -\sum_{i,j} J_{ij}\,\mathbf{S}_i \cdot \mathbf{S}_j \tag{1.5}$$

Which is the famous Heisenberg model. An important perceptive originated from the Heisenberg model is the Bethe-Slater curve. When the interatomic spacing (*a*) of an element is small, the spatial overlap of the electron wavefunctions is significant, resulting in a negative J_{ij} and antiparallel (triplet) spin configuration. On the contrary, a larger interatomic-spacing results in the anti-bonding sate, therefore positive J_{ij} and a parallel (singlet) spin configuration. While rather heuristic, using the radius (*r*) of the more magnetically active *d* orbitals as a normalizing factor, the Bethe-Slater curve (as shown in Fig. 1-2) represents the transition from antiferromagnetic (AFM) to ferromagnetic (FM) as the ratio of a/r increases, with the three iconic FM elements (α-Fe, Co, Ni) having $J > 0$ located at sufficiently high a/r while Mn and Cr with low a/r has $J < 0$ therefore showing AFM.

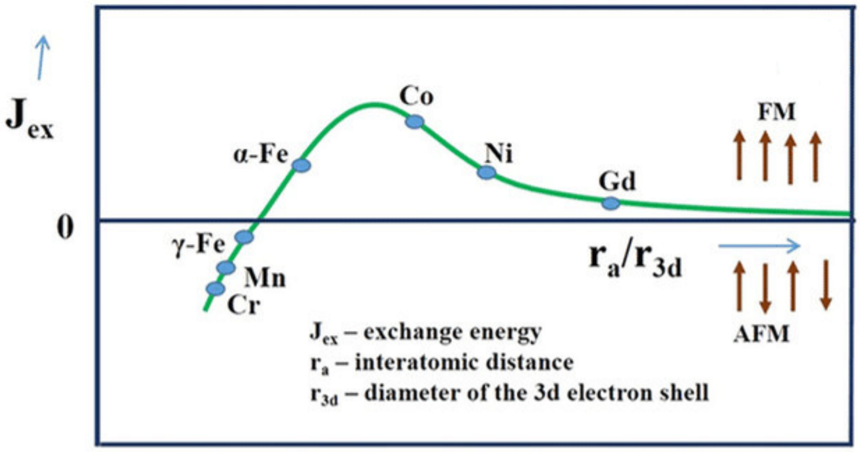

Fig. 1-2 The Bethe-Slater curve. Using the value of interatomic distance (*a*) divided by the radius (*r*) of the 3*d* electrons as a figure of merit, the ferromagnetism and antiferromagnetism in 3*d* transition metals can be explained. Figure reprinted from [4].

doi:10.6342/NTU202404434

1.1.2 Indirect exchange: Superexchange

While the direct exchange and the Heisenberg model can account for some magnetic properties when direct overlap is significant between neighboring magnetic orbitals, it fails to explain the magnetic behaviors in systems where the overlap between individual orbitals are weak. For example, the 4*f* elements where orbitals are highly localized near the atomic nucleus, and the existence of ionic, oxide ferrimagnets such as spinel ferrites[3,5]. This is where the indirect exchange comes in to explain the origin of these magnetic orderings. This "indirect" means that the exchange is mediated by ions in the case of superexchange, and itinerant electrons in the case of RKKY.

For of superexchange, let's consider an ionic transition metal monoxide. As shown in Fig. 1-3, when one of the two electrons with p_x orbital is excited into a *d* orbital due to the ionic bonding (a σ bond, for example), the other electron can also be excited to another *d* orbital of the transition metal ion located on the opposite side. In this configuration, the occupied *d* orbitals from the two ions must be filled with opposite spins to satisfy the Pauli exclusion principle (Fig. 1-3 lower half). Notice that under this picture, superexchange is almost exclusively antiferromagnetic though if one of the metal ions have filled orbitals, or have none 180° bond angles, then ferromagnetism may occur [6].

doi:10.6342/NTU202404434

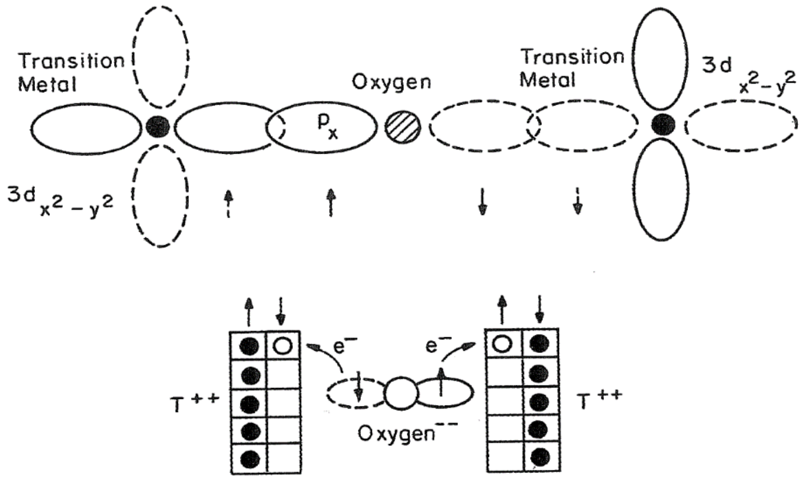

Fig. 1-3 Graphical representation of two 3*d* orbitals mediated by superexchange due to the oxygen's 2*p* orbitals, in a transition metal monoxide. The solid/dashed lines represent the positive/negative phase of the respective wavefunctions. The two electrons of the filled $2p_x$ orbitals have opposite spins. The lower part of the graph depicts how electrons are filled when considering the Pauli exclusion principle. Reprinted from [5].

1.1.3 Indirect exchange: RKKY Interaction

In rare-earth metals the 4*f* electrons are highly localized due to them lying very close to the nucleus. This results in little probability for the direct exchange, where some wavefunction overlap is required. Therefore, similar to superexchange, some kind of exchange takes place via an intermediary, which turns out to be the itinerant electrons in metals in the case of RKKY.

Ruderman, Kittel, Kasuya and Yoshida [7-9] proposed a model based on the effect of screening exerted on the conduction electrons. Without going into the mathematically abstruse details, a physically intuitive picture is as follows. Take the aforementioned 4*f* orbitals as example, this highly localized 4*f* moment polarizes the conduction electrons

doi:10.6342/NTU202404434

nearby, which then communicate this spin information to other magnetic sites due to their extended wavefunctions [1,5]. This process occurs due to the background charge trying to screen (neutralize) the charge of an impurity when said impurity is placed in the electron gas, and the electron gas will analogously try to screen out the magnetic moment with their own spins. However, the altered wavefunctions of the electron gas have a limited range of wavelengths to choose from due to the Fermi energy, $\hbar^2 k_F{}^2/2m_e$ (m_e being the effective mass of an electron), where the lowest wavelength is characterized by $k \geq k_F$. One can imagine trying to generate a Fourier expansion for a non-oscillatory function but there is always a residual oscillatory term due to the limitation on the Fourier components in this case imposed by $k \geq k_F$. Overall, non-zero and oscillatory spin polarization exist near the magnetic site for the itinerant electrons.

The RKKY interaction can be mathematically expressed similar to eqn. (1.5) but now the oscillatory J depends on k_F and the distance from the magnetic site

$$\widehat{H} = -\sum_{i,j} J(r)\, \mathbf{S}_i \cdot \mathbf{S}_j \tag{1.6}$$

Where J can be calculated to be [10]

$$J \propto \frac{\sin(2k_F r)}{(2k_F r)^2} \tag{1.7}$$

The damped oscillatory exchange strength is evident from the sine term in eqn. (1.7).

doi:10.6342/NTU202404434

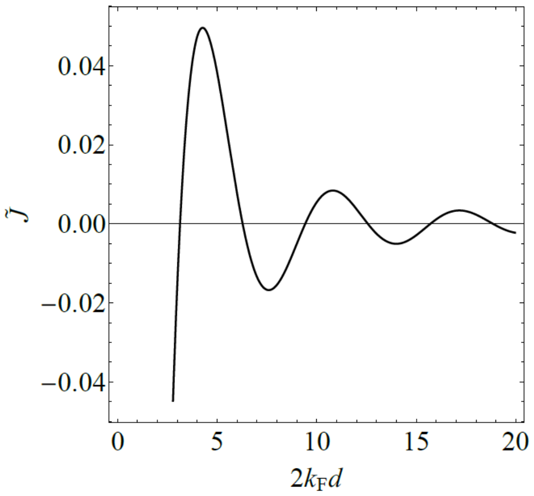

Fig. 1-4 The dimensionless oscillatory RKKY coupling constant as a function of Fermi wavelength times the distance (*d* is used instead of *r* in this figure). Reprinted from [10].

RKKY has become extremely important in contemporary spintronic applications because the interlayer distance (and the interlayer material) between two magnetic moments can be engineered to give rise to either FM ($J > 0$) or AFM coupling ($J < 0$). This is achieved by utilizing the synthetic antiferromagnetic (SAF) structure in the AFM region to pin the reference layer within a magnetic tunnel junction (MTJ), making it more resistant to perturbation (see Fig. 1-5(a)). It has also been proposed to serve as a more stable free layer [11]. Parkin [12] has demonstrated that elements such as Ru, Ir, Rh etc. are large RKKY mediators (Utilization of Ru has become a staple in spin valve and MTJ structures), while several other metals such as Cr, Cu etc. mediates weak but still observable RKKY interaction (refer to Fig. 1-5(b)).

doi:10.6342/NTU202404434

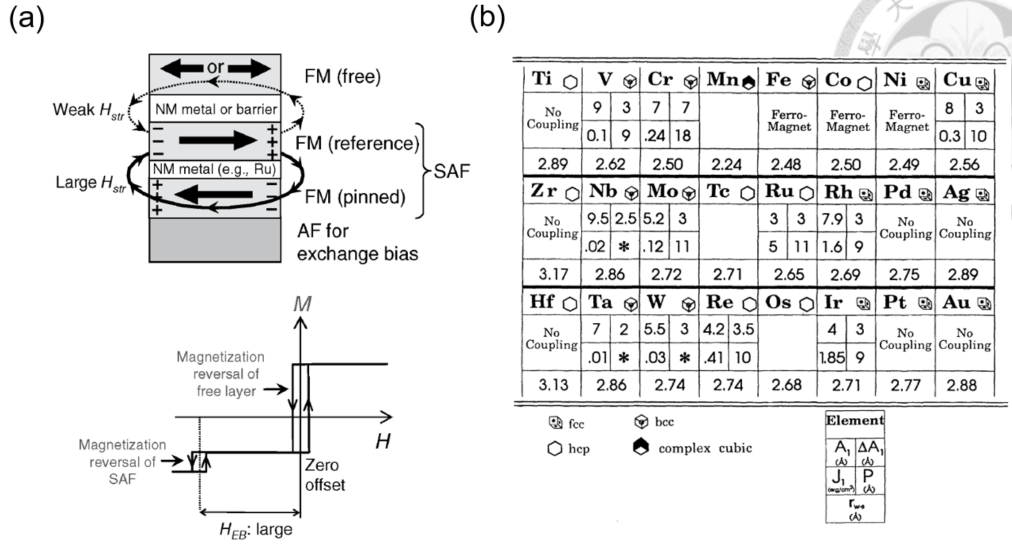

Element	A_1 (Å)	ΔA_1 (Å)	J_1 (erg/cm²)	P (Å)	$r_{w\text{-}s}$ (Å)
Ti	No Coupling				2.89
V	9	3	0.1	9	2.62
Cr	7	7	.24	18	2.50
Mn					2.24
Fe	Ferro-Magnet				2.48
Co	Ferro-Magnet				2.50
Ni	Ferro-Magnet				2.49
Cu	8	3	0.3	10	2.56
Zr	No Coupling				3.17
Nb	9.5	2.5	.02	*	2.86
Mo	5.2	3	.12	11	2.72
Tc					2.71
Ru	3	3	5	11	2.65
Rh	7.9	3	1.6	9	2.69
Pd	No Coupling				2.75
Ag	No Coupling				2.89
Hf	No Coupling				3.13
Ta	7	2	.01	*	2.86
W	5.5	3	.03	*	2.74
Re	4.2	3.5	.41	10	2.74
Os					2.68
Ir	4	3	1.85	9	2.71
Pt	No Coupling				2.77
Au	No Coupling				2.88

Fig. 1-5 (a) A representative spin-valve/MTJ structure where the reference layer is pinned by the pinned layer via RKKY. The advantage of this is two-fold, the first being a large exchange bias that makes the reference layer resistant to perturbation, and the second being the minimal stray field exerted on the free layer, due to the “flux closure” in the SAF trilayers. Reprinted from [13]. (b) A list of 3*d*, 4*d* and 5*d* transition metal’s efficacy at moderating RKKY between discrete magnetic layers. A_1 is the thickness where the first peak of AFM occurs. ΔA_1 denotes the length of the first AFM region. J_1 is the energy density corresponding to the maximum AFM coupling strength. P is the oscillation period. Note that a substantial amount of these transition metals can more or less mediate RKKY. Reprinted from [12]

1.1.4 Dzyaloshinskii-Moriya Interaction

Dzyaloshinskii-Moriya Interaction, or DMI in short, is a very unique type of exchange. Unlike other exchange interactions represented by an inner product (thus promoting the parallel/antiparallel spin alignments), DMI is characterized by a cross product energy term

doi:10.6342/NTU202404434

$$\widehat{H}_{\mathrm{DMI}} = -\mathbf{D}_{ij} \cdot (\mathbf{S}_i \times \mathbf{S}_j) \tag{1.8}$$

The DMI theory was originally developed to explain the weak ferromagnetism in α-Fe_2O_3 by Dzyaloshinskii [14]. Moriya [15] then pointed out that the spin interaction that lead to spin canting in a specific state of α-Fe_2O_3 (which leads to weak ferromagnetism) takes an antisymmetric form (eqn. (1.8)). The physical picture of DMI is in fact based on the superexchange and the RKKY exchange [1,16], for ionic materials and metallic systems, respectively. Its physical picture goes something like the following. The interaction arises due to the spin information sharing, say, in the superexchange, is normally collinear. However, the superexchange can be upset if sizable spin-orbit coupling (SOC) exists in the mediating anion orbitals, and the electron hopping in superexchange can be accompanied by a spin-flipping process. This process has a net effect of zero unless the inversion symmetry is broken, and therefore the characteristic vector $\mathbf{D}_{ij}$ is dictated by the broken inversion symmetry as well as the crystal structure.
A similar scenario is deduced by Smith [17] in 1976 where spin-orbit scattering of the conduction electrons (by nonmagnetic impurities) could give rise to a DMI term from the RKKY mechanism.

DMI is found responsible for the formation of exotic spin textures, notably magnetic skyrmions and Néel domain walls in magnetic thin films. These spin textures are rich in physics and simultaneously influential to the development of future spintronic devices.

In two dimensional materials such as $MnPS_3$ [18], DMI and its corresponding **D** vectors are nonzero due to intrinsically broken inversion symmetry stemming from its crystal structure. Fig. 1-6(a) (top) provides a viewpoint on why the **D** vector points out of plane. The chiral Néel domain walls can be formed due to the interfacial DMI (Fig. 1-6(a)

doi:10.6342/NTU202404434

bottom), which is advantageous over conventional Bloch walls in current-driven dynamics. Fig. 1-6(b) demonstrates how chiral Néel walls can be driven by SOT, while Bloch walls can only be driven by spin-transfer torque [19-22]. Parkin et al. introduced the idea of racetrack memory by capitalizing on this fast motion of domain walls (Fig. 1-6(c) left) [23,24]. Fert et al. further proposed skyrmion racetrack memory which has a similar concept since similar to a domain wall, skyrmions can be driven into motion by a sizable spin current [25].

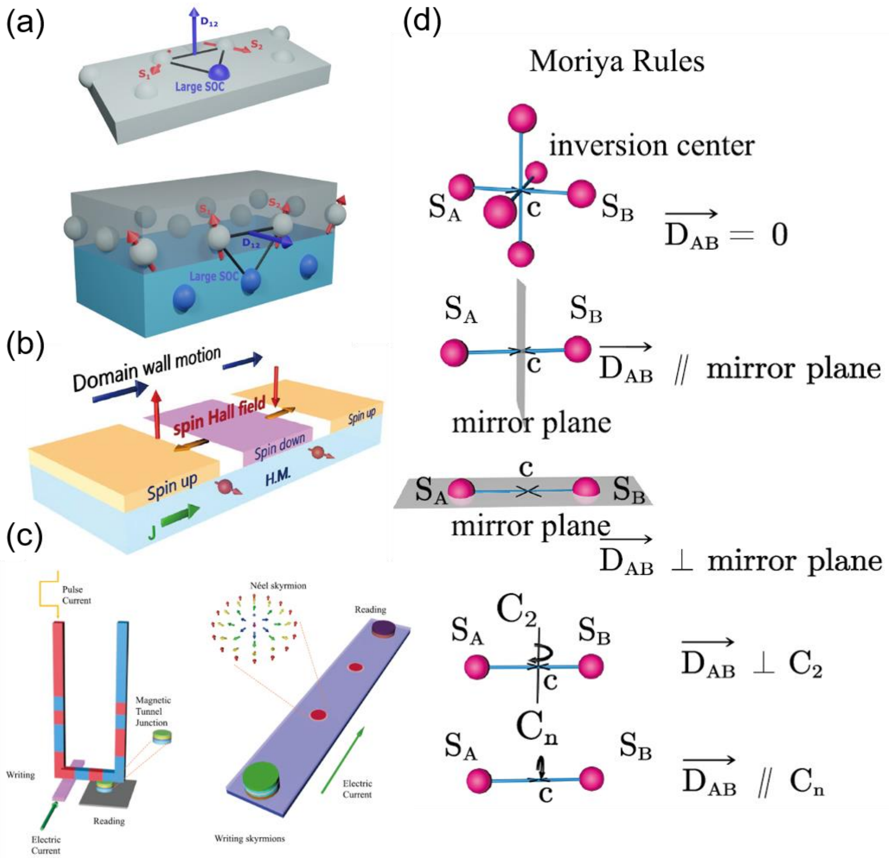

Fig. 1-6 (a) (top) The interaction between two spins with a neighboring nonmagnetic atom with large SOC yields DMI. The $\mathbf{D}_{12}$ points out of the sample plane due to the direction of the symmetry breaking. (Bottom) In thin films, existence of interfacial DMI and the corresponding **D** vector is due to the inversion asymmetry from the stacking order of the different layers. Adapted from [26]. (b) The effect of SOT on chiral Néel walls. (c) Domain wall (left) and skyrmion (right) racetrack memory concepts. Reprinted from [16]. (d) The five symmetry-dependent Moriya rules. Reprinted from [16].

It can be seen that DMI is closely related to RKKY (such as the similarities involved during their respective derivation), but the key difference is the clear directionality exhibited in DMI due to the characteristic vector $\mathbf{D}_{ij}$, while RKKY simply enforces parallel/antiparallel spin configuration between magnetic layers. Moriya, in his original paper [15] provides us a glimpse on how symmetry affects DMI by deriving a set of “Moriya rules”, involving two magnetic ions located at points A and B, and the center of $\overline{AB}$ denoted as C. These five rules are as follows [16]:

1. When an inversion center is located at point C, then $\mathbf{D}_{AB} = 0$.
2. If a mirror plane contains C and is perpendicular to $\overline{AB}$ then $\mathbf{D}_{AB} \perp \overline{AB}$.
3. When a mirror plane includes both A and B, then $\mathbf{D}_{AB} \perp$ mirror plane.
4. When there’s a two-fold rotation axis that passes through C and if said axis $\perp \overline{AB}$, $\mathbf{D}_{AB} \perp$ two-fold axis.
5. If there’s a n-fold ($n \geq 2$) rotational axis along $\overline{AB}$, $\mathbf{D}_{AB} \parallel \overline{AB}$.

The graphical representation of these rules is provided in Fig. 1-6(d). It’s apparent that these symmetry rules are suitable for crystals (such as the previously mentioned $MnPS_3$), and for material systems with innately higher symmetry (such as amorphous/polycrystal thin films) we’ll further elaborate how the 3rd Moriya rule is especially useful to describe the energy landscape of IL-DMI, in section 2.1.

1.2 Transport Phenomena

In most of this work, the monitoring of the magnetic moments is achieved by electrical transport measurements, alongside MOKE techniques. These techniques measure either the longitudinal resistance of a magnetic heterostructure (magnetoresistance, MR) or the transverse resistance (Hall effect), therefore allow us to capture the interplay of exotic exchange interaction with local magnetic moments.

1.2.1 Anomalous Hall Effect and Spin Hall Effect

The widely known ordinary Hall effect (OHE) was first observed by Edwin Hall in 1879. When a z directional magnetic field (H_z) is applied to a normal metal conductor, a voltage (V_H) is detected transverse to the applied current, as shown in Fig. 1-7(a). This can be understood by the Lorentz force exerted on the charge carriers due to the application of H_z. The polarity of V_H depends on the charge carrier's type of the material (either electrons or electric holes).

Also observed by Edwin Hall is the anomalous Hall effect (AHE). AHE is an additional contribution to the Hall signal which directly depends on the z directional magnetization (m_z) of the material, rather than the external field, as shown in Fig. 1-7(b). Therefore, experimentally speaking, the observed V_H can be expressed as

$$V_H = V_{OHE}H_z + V_{AHE}m_z \tag{1.9}$$

Where V_{OHE} and V_{AHE} are the coefficients for OHE and AHE, respectively. The "anomalous" part of AHE is that its magnitude is often much larger than OHE [27], as represented by Fig. 1-7(c). Importantly, the monitoring of V_{AHE} (assuming negligible contribution from V_{OHE}) enables electrical detection of the magnetization, and many other experimental techniques [28,29].

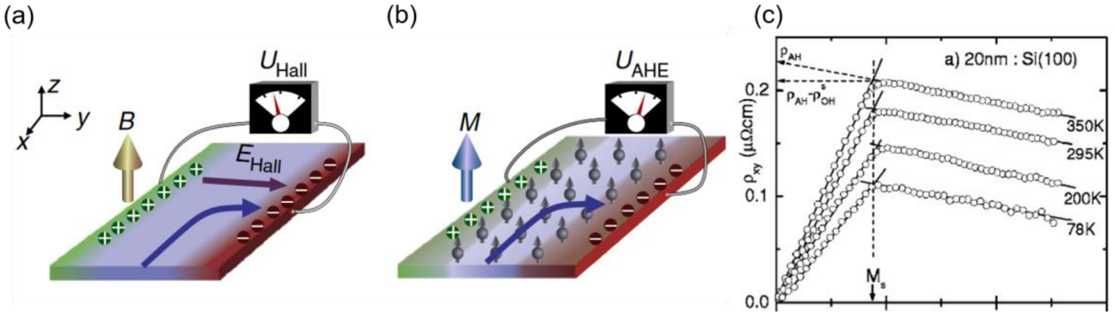

Fig. 1-7 Schematics of (a) OHE and (b) anomalous Hall effect. Adopted from [30] (c) The orthogonal resistivity of a 20 nm thick Co film under varied H_z. Note the clear saturating behavior when saturation of the magnetization (M_s) is reached, and the superposition of OHE and AHE to the overall transverse resistivity.

The origin of the AHE is still shrouded in some debate. However, there are three generally accepted mechanisms: skew scattering, side jump and intrinsic scattering. At first the skew scattering was believed to be the primary source of the AHE [31]. Skew scattering can be pictured as follows: when an electron encounters a moving impurity, this impurity is approaching at some speed which radiates an oersted field (**H)** around this impurity (assuming the impurity is charged). Electrons with like spins passing by the right side and the left side of the impurity will experience **H** in opposite directions, but since the force exerted on the electrons takes the form $\mathbf{F} = \nabla (\mathbf{s} \cdot \mathbf{H})$ [31], the electrons with like spins are collectively scattered to the same direction. On the other hand, side jump is also extrinsic, but in this mechanism the electron experiences a sideways shift during scattering, leading to a transverse displacement [27,31]. Lastly, the intrinsic scattering arises from the band structure of the FM material, where the Berry curvature of the crystal structure gives rise to an effective magnetic field in the momentum space, leading to a spin-dependent transverse velocity [27,31]. A graphical compilation of these three mechanisms are compiled in Fig. 1-8.

Regardless of the mechanism, the spin up and spin down will be deflected to opposite directions, and due to the existence of majority and minority spins within the ferromagnetic material, a detectable charge accumulation is generated along the transverse direction of the applied current.

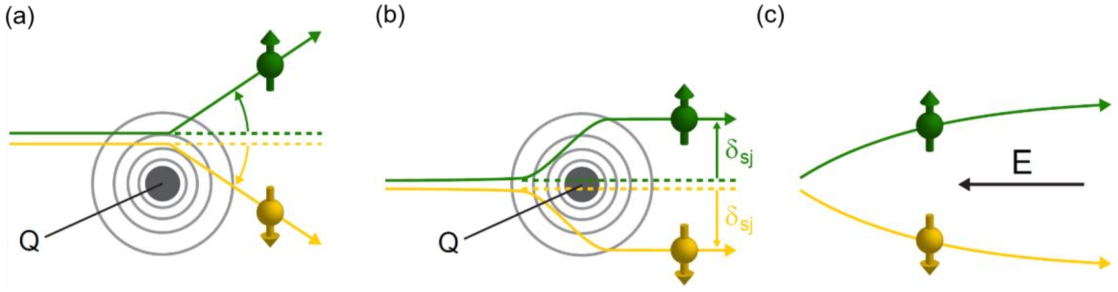

Fig. 1-8 Three widely accepted mechanisms of AHE. (a) Skew scattering (b) Side jump are both extrinsic and (c) Intrinsic scattering. Reprinted from [32].

The spin Hall effect (SHE) is a close relative to AHE that occurs in materials with high SOC [33,34]. SHE’s underlying mechanisms are almost identical to that of AHE (see Fig. 1-8), though with some subtle differences. For example, since the population of spin-up and spin-down electrons are identical in a non-magnetic material, SHE is not identifiable by a transverse Hall voltage (such as AHE), but a spin current perpendicular to the charge current will occur, which is expressed as

$$J_s = \frac{\hbar}{2e}\theta_{SH}(\boldsymbol{\sigma} \times J_c) \tag{1.10}$$

Where θ_{SH} is the spin Hall angle which quantifies the charge-to-spin conversion capability of a specific material, $\boldsymbol{\sigma}$ is the spin polarization direction and e is an elementary charge. Conventionally speaking, elements with high SOC (4d or 5d transition metals, for example) such as Pt, W, Ta has a high θ_{SH} [35].

The importance of SHE here is its capability to supply sizable spin current to the interface of an adjacent FM layer. This spin accumulation then exerts SOT on the FM layer according to the Landau-Lifshitz-Gilbert-Slonczewski (LLGS) equation [29]

$$\frac{d\mathbf{m}}{dt} = -\gamma\mathbf{m}\times\mathbf{H_{eff}} + \alpha\mathbf{m}\times\frac{d\mathbf{m}}{dt} + \beta\xi_{DL}\mathbf{m}\times(\boldsymbol{\sigma}\times\mathbf{m}) - \beta\xi_{FL}\mathbf{m}\times\boldsymbol{\sigma} \tag{1.11}$$

Where γ is the gyromagnetic ration, α the damping constant, β the current density, ξ_{DL} and ξ_{FL} the damping-like (DL) and field-like (FL) SOT efficiency, respectively. One can picture this as the local magnetic moment exchanging angular momentum with the accumulated spins via the exchange interaction. Overall, the local magnetization can be manipulated by the SOT originated from SHE, even achieving magnetization switching [36].

1.2.2 Unidirectional Magnetoresistance

Unidirectional magnetoresistance (UMR) occurs when the spin accumulation (induced by SHE, for example) is parallel/antiparallel to the FM's magnetization direction. The origin of UMR is related to the splitting of the spin-dependent electrochemical potentials, leading to different transmission coefficient (therefore different interface resistance) when $\boldsymbol{\sigma} \parallel \mathbf{m}$ (high resistance) or $\boldsymbol{\sigma} \parallel -\mathbf{m}$ (low resistance) [31], as schematically shown in Fig. 1-9(a). One of the great practical utilization of UMR is that it provides differentiable electrical signal when the magnetization of an in-plane magnetized (IMA) layer is switched, allowing the IMA layer to be probed electrically. This UMR signal difference is shown in Fig. 1-9(b) during field scan, while detection of SOT-induced magnetization switching is demonstrated in Fig. 1-9(c).

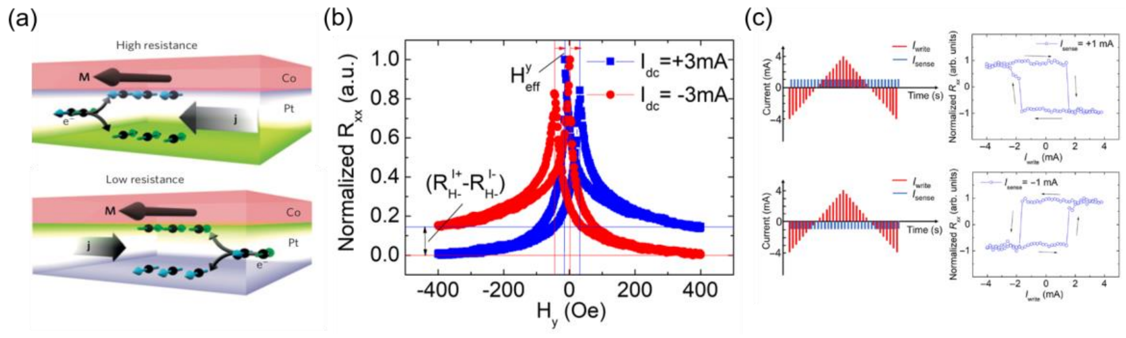

Fig. 1-9 (a) the high/low resistance state of UMR originated from the reflection/transmission coefficient of electrons. Reprinted from [37]. (b) Reversed UMR polarity when the magnetization is switched by an *y*-directional field H_y. (c) By consecutively changing the polarity of the read current, hysteresis behavior during the SOT induced magnetization switching can be probed. (b) & (c) reprinted from [38].

1.3 Magneto-optical Kerr effect (MOKE)

The electrical detection of magnetic layers possessing in-plane magnetic anisotropy (IMA) are often challenging. While real-time monitoring of layers with PMA can be done exploiting the AHE enabling easy and real-time observations, fast and electric based detection is lacking, conventionally only accessible by MTJ fabrication and utilize the TMR effect for readout, which requires extensive fabrication expertise and resources. This is where the optical detection comes in, utilizing the longitudinal Magneto-Optical Kerr effect (L-MOKE). Using this optical method, magnetic behaviors can be extracted. This homemade L-MOKE setup, in conjunction with other less straightforward detection scheme such as the unidirectional magnetoresistance (UMR) [38,39] measurement, makes the detection of IMA's behaviors possible.

1.3.1 Overview of the MOKE signal

In the simpliest terms, MOKE arises due to the Lorentz force. The electric field of a linearly polarized light excites the impacted material's electrions, and in the case of a nonmagnetic material, electrons simply oscillate parallel to the incident polarization (and so is the emitted reflective light's polarization). When the material is magnetic, however, the Lorentz force induces a small polarization component (the Kerr component) that is perpendicular to both the original polarization direction and the magnetization's orientation, when the material's electrons oscillate. This is the direct result of the Lorentz force creating an orthogonal electric field [40]. Therefore, by detecting this additional "Kerr component", the magnetic behavior of the magnetization can be reconstructed.

It's helpful to differentiate the three types of MOKE, namely P-MOKE, T-MOKE and L-MOKE where the prefix indicates the relations between light's incident plane and the magnetization direction, as seen in Fig. 1-10. In P-MOKE and L-MOKE signal originates from magnetization parallel to the plane normal, and magnetization in the plane of the sample while parallel to the incident plane, respectively. In T-MOKE the magnetization is also in the plane of the sample, but is perpendicular to the incident plane.

doi:10.6342/NTU202404434

In this setup, the L-MOKE configuration is employed.

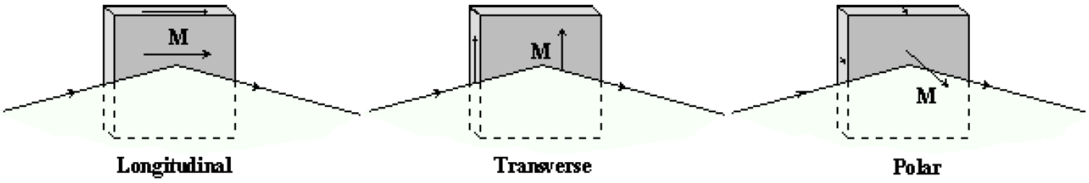

Fig. 1-10 Longitudinal, transverse and polar Kerr effects, adopted from [40].

In essence, the MOKE signal we need to measure is a rotation of s or p polarized light reflected from the ferromagnetic sample surface (Fig. 1-11) [41,42]. For example, if the incident light is, say, purely p polarized (with amplitude E_p) after traveling through a polarizer plate, then the reflected light would include a small s component (with amplitude E_s), and therefore the Kerr rotation can be subsequently expressed as $\theta_k = E_s/E_p$ [43]. Experimentally, another polarizing plate (called the analyzer) is placed between the reflected light and the photodetector to extract the value of θ_k. In our experimental setup, the analyzer is some angle δ away from the s axis. The intensity I measured at the photodiode then can be expressed as:

$$I = |E_p \sin\delta + E_s \cos\delta|^2 \approx |E_p\delta + E_s|^2 \tag{1.12}$$

for a small enough δ. By substituting $\theta_k = E_s/E_p$ into eqn. (1.12) we get:

$$I = |E_p|^2 |E_k|^2 \approx |E_p|^2 \left(\delta^2 + 2\delta\theta_k\right) \tag{1.13}$$

If the magnetization switches direction, however, the E_s part also reverses sign giving:

$$I \approx |E_p|^2 (\delta^2 - 2\delta\theta_k) \tag{1.14}$$

This intensity disparity between different magnetization states as represented by eqn. (1.13) and (1.14) is what enables the MOKE magnetometer to capture the hysteresis behavior of the IMA magnetization.

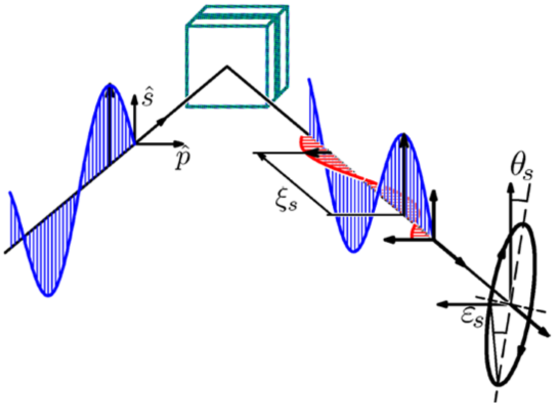

Fig. 1-11 Demonstration of a *s* polarized incident light gaining an additional *p* component after reflecting from a magnetic surface, reprinted from [43].

1.3.2 L-MOKE instrument setup and verification

Our homemade MOKE setup integrated an AC laser, Lock-in amplifier, Helmholtz coil and a rotary stage for accurate thin film characteristics analysis. Since the analyzer and polarizer operates nearly at orthogonal (polarizers crossed), the lock-in detection scheme eliminates the need for a dark room, which is mandatory for DC measurement. The additional rotary xy-stage enables angle-dependent measurements, and the coreless Helmholtz coil provides an in-plane field of up to 270 Oe while simultaneously suppressing magnetic remanence to less than 0.25 Oe. Overall, the layout of the MOKE equipment setup can be seen in Fig. 1-12 (a) with a typical hysteresis loop shown in Fig. 1-12 (b).

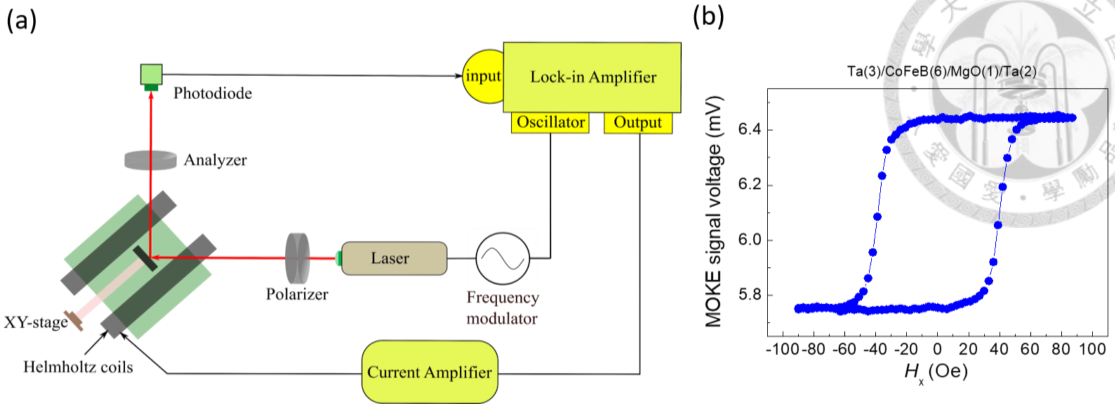

Fig. 1-12 (a) Schematic layout of the AC L-MOKE setup, and a representative hysteresis loop. (b) A representative field scan hysteresis loop measuring a typical Ta(3)/CoFeB(6)/MgO(1)/Ta(2) sample using said L-MOKE setup.

Calculations done by Allwood et.al. [42] provides a straightforward means of benchmarking this setup's capability and reliability. By incorporating a depolarization ratio γ_D which accounts for the imperfect setup along the optical path (such as the relative angle between the polarizers and the laser beam), a "fractional L-MOKE signal" can be deduced from eqn. (1.13) and eqn. (1.14):

$$\frac{\Delta V}{V_0} \approx \frac{2\theta_k \sin 2\delta}{\sin^2 \delta + \gamma_D} \tag{1.15}$$

With V_0 denoting the average intensity of a hysteresis loop, and ΔV is the signal difference between the two magnetic states. Calculated $\Delta V/V_0$ via eqn. (1.15) using $\gamma_D = 2.1 \times 10^{-4}$ and different θ_k are plotted in Fig. 1-13(a) [42], this curve provides invaluable insight into designing and testing of a MOKE magnetometer. Experimentally, an identical test has been conducted by our L-MOKE setup, producing a similar graph in which both θ_k and γ_D can be extracted from a typical IMA thin film (the structure being

W(4)/CFB(10)/MgO(1)/Ta(3)). Clearly, the results from the initially unoptimized setup (Fig. 1-13(b)) cannot be well fitted by eqn. (1.15). After optimizing the optical path, $\Delta V/V_0$ can be well fitted by eqn. (1.15) (Fig. 1-13(c)) where the fitted Kerr rotation of 4.117 mrad and depolarizing factor of 4.19×10^{-5} agrees well with typical results [44,45]. These results show the viability of our setup, giving credibility to future experiments done by the MOKE system.

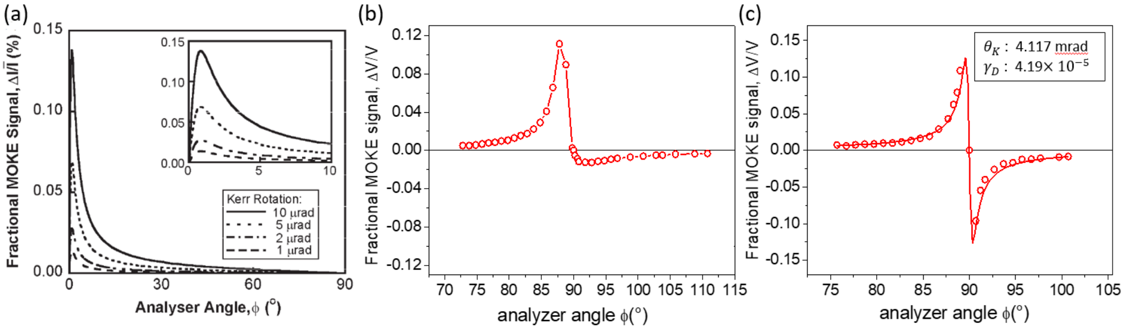

Fig. 1-13 (a) Calculated fractional MOKE signal as a function of analyzer angle ϕ for different Kerr rotation angles as stated in the inset (reprinted from [42]). (b) Fractional MOKE signal measured from a W(4)/CFB(10)/MgO(1)/Ta(3) sample with nonideal optical path. (c) Identical sample in (b) measured with an optimized setup, from eqn. (1.15) a fitting curve is obtained (red solid line). Inset shows the fitted Kerr rotation and depolarization factor.

The primary usage of this L-MOKE magnetometer is to capture the IMA layer's hysteresis behavior, which as we'll elaborate later, might be influenced by the existence of interlayer Dzyaloshinskii–Moriya interaction. Furthermore, we'll also elucidate the possible causality between magnetic related symmetry breaking and interlayer Dzyaloshinskii–Moriya interaction via L-MOKE analysis.

1.4 Motivations

Be it in academia or industry, researches into magnetic phenomenon have sparked numerous breakthroughs. From the earlier magnetic tape recording, to the state of the art STT and SOT-MRAM currently being evaluated by big foundries, there are numerous novel possibilities to be opened up for improvements. The vast majority of magnetic investigations up until the first decade of the 21st century focused on collinear magnetism, or the well-known ferromagnets and antiferromagnets (for example, Fe and NiO, respectively). However, with the introduction of symmetry breaking, especially due to the creation of distinct interfaces, a clear energy preference for noncollinear rotational chirality is formed [14,15,46]. The reason behind this is the creation of *interfacial* Dzyaloshinskii–Moriya interaction (DMI), due to which noncolinear magnetic structure within the magnetic layer is formed at the interface, this includes Néel type domain walls [22,47,48] and skyrmions [49-51].

Following these progresses, we're intrigued by the possibility of extending the DMI to an *interlayer* case, where the orthogonal configuration of spins (magnetizations) are now separated by a spacer layer. Starting from the investigation of wedge-deposition related in-plane magnetic anisotropy via a homemade MOKE system, attempts are made to leverage this effect as the symmetry breaking element. What we unexpectedly found is the fascinating generation of interlayer DMI (IL-DMI), where a clear configurational chirality is indeed preferred between the two magnetic layers involved. We subsequently intended to characterize the strength and characteristic direction of this interaction. IL-DMI paves the way to exciting future applications, such as combining conventional interfacial DMI with IL-DMI to create arrays of tunable 3-dimentional structures (i.e.

doi:10.6342/NTU202404434

skyrmions), or even assist in the development of the long-promoted racetrack memory [16,24]. Here, we experimentally demonstrate and model how field-free current induced switching can be achieved, which is mediated by IL-DMI across the two magnetizations.

Motivated by the successful generation of IL-DMI and demonstrating its practical usage by achieving field-free current induced switching, we're interested in controlling IL-DMI's strength and direction in various systems via growth condition control, and through careful comparisons with control samples, different symmetry breaking methods and consulting previous works, eventually, we established a model that can appropriately account for the microscopic origin of IL-DMI while satisfying the various experimental data we obtained. By understanding these various properties, a clearer picture about IL-DMI can be obtained, we eventually aim to learn more about the relationship between the RKKY interaction and IL-DMI.

doi:10.6342/NTU202404434

Chapter 2 Observation of Interlayer Dzyaloshinskii-Moriya interaction in symmetry broken systems

Theoretical and experimental investigations into DMI has been numerous since the early 2010s, where researchers are immensely interested in DMI's key role in noncollinear magnetism and topologically non-trivial spin structures. DMI is an antisymmetric interaction that promotes orthogonal arrangement between neighboring spins. An indispensable requirement of DMI generation is the breaking of symmetry, which is often naturally achieved by the formation of an interface between different layers. Therefore, generation and detection of DMI are traditionally focused on the *interfacial* case where the orthogonally aligned spins belong to the same FM layer such as the formation of chiral Néel domain wall and its proposed domain wall logic [23], as well as skyrmions based racetrack memory [25]. Recent theoretical calculations and experimental reports, extends DMI from the *interfacial* case to the *interlayer* scenario where the antisymmetric chirality is induced across discrete magnetic layers [52]. This chapter details our initial observation and characterization of IL-DMI in two orthogonally magnetized ferromagnetic layers separated by a Pt coupling spacer. The importance of in-plane symmetry breaking is emphasized through wedge deposition of the samples. As a proof-of concept of IL-DMI's utility in practical devices, deterministic current-driven field-free magnetization switching in the perpendicularly magnetized FM layer is also achieved. This chapter primarily includes content from my published article "Growth-Dependent Interlayer Chiral Exchange and Field-Free Switching" [53] along with some

doi:10.6342/NTU202404434

additional information.

2.1 Generation and Detection of IL-DMI

2.1.1 In-plane symmetry breaking

In general, DMI arises from strong SOC and symmetry breaking at the FM/NM interface [16,54-56]. In the case of interfacial DMI, the inversion symmetry breaking causes the antisymmetric interaction to occur within the FM layer, as experimentally observed by Chauleau et al. [57]. As seen in Fig. 2-1(a)&(b), the reversed stacking order (thus an opposite broken inversion symmetry) directly changes its chiral behavior (clockwise or counterclockwise). This observation serves as a vivid example of how the directionality of symmetry breaking dictates DMI's configuration. Extending this physical picture, Han et al. [26,58] argued that if the symmetry breaking factor is rotated from the out-of plane direction into the plane of the thin film, then the orthogonal spin structure should also be rotated therefore mediated between discrete magnetic layers, creating the IL-DMI scenario (Fig. 2-1(c)&(d)). To date, two approaches have been reported in literature to generate the required in-plane symmetry breaking. The first is the utilization of oblique angle (wedge) deposition where the rotation of the sample is disabled during the growth of specific layers (Fig. 2-2(a)) [58-61]. The second is the application of an external field during growth (Fig. 2-2(b)) [62-64]. Here, the wedge deposition method is chosen, though investigations into the viability of the second method will be detailed in section 3.2. In addition, the two magnetic layers are orthogonally magnetized to take advantage of the fact that DMI's magnitude is maximized when the two magnetic moments are perpendicular to each other.

doi:10.6342/NTU202404434

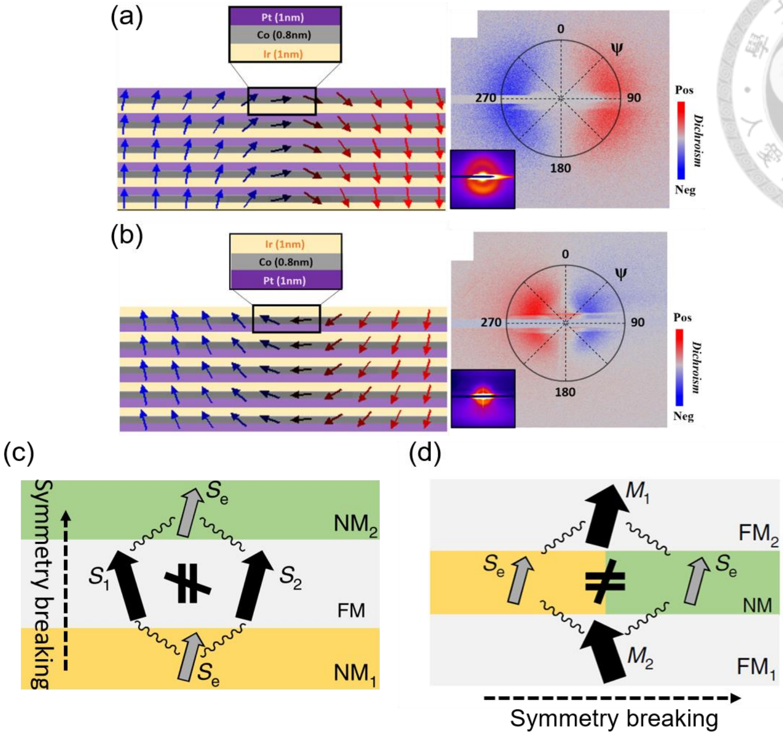

Fig. 2-1 The influence of symmetry breaking on DMI. (a), (b) The opposite magnetic winding configuration due to the reversed Ir/Co/Pt (Pt/Co/Ir) stacking order. The dichroism signal comes from the fact that the diffracted X-ray's dichroic diffraction pattern rotates oppositely for opposite DMI chiralities (reprinted from [57]). (c), (d) The requirement of an in-plane symmetry breaking is instrumental to IL-DMI's generation (reprinted from [58]). Note that symmetrically speaking, the IL-DMI scenario in (d) can be considered a coordination rotation from (c), thus the inversion asymmetry becomes less important.

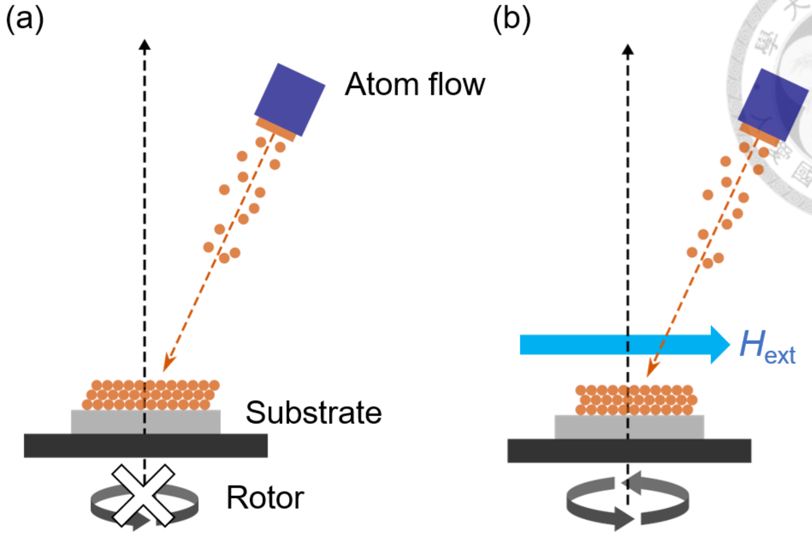

Fig. 2-2 Illustration of two means of creating in-plane symmetry breaking (a) Schematics of the oblique (wedge) deposition. The symmetry breaking factor is determined by the atom flux direction when the rotor is disabled. (b) Schematics of the sample growth with an external in-plane field H_{ext}. The symmetry breaking direction is determined by H_{ext}. For a comprehensive view on how oblique (wedge) deposition is controlled within our sputtering system, refer to the appendix at section 6.1.

2.1.2 Observation of IL-DMI

Based on the criteria above, a series of specimens with the structure of CoFeB(2)/Pt(2.5)/Co(0.6)/Pt(2.5) (values in parentheses are in nanometers) was fabricated using a high-vacuum confocal magnetron sputtering system. The deposition is executed under a base pressure of approximately 10^{-7} Torr, with an Ar working pressure of 3×10^{-3} Torr, onto Si/SiO_2 substrates. Avci et. al.'s pioneering research [65] has pointed out Pt as an ideal mediating spacer in contrast to other heavy metals (HM). This suitability aligns well with the extensively reported HM/FM interfacial DMI scenarios [22,51,66,67]. Of the two ferromagnetic (FM) layers, the CoFeB layer exhibits IMA due to its considerable thickness surpassing the spin reorientation transition thickness [68,69], while Co demonstrates PMA due to robust interfacial anisotropy at the two Co/Pt interfaces [70,71]. During deposition, substrate rotation was disabled, and the direction of the CoFeB atom flux was set to strike the substrate normal at an angle of $\alpha = 25°$, facilitating the formation of a wedged multilayer structure and inducing the required in-plane symmetry breaking (refer to Fig. 2-3(a)). For a comprehensive view on how oblique (wedge) deposition is controlled within our sputtering system, refer to the appendix at section 6.1. Conversely, Pt was deposited in a configuration with normal incidence at $\alpha = 0°$. For measurements of anomalous Hall resistance (R_H) and unidirectional magnetoresistance (UMR), Hall bar devices with a lateral geometry of 5 × 60 μm and various orientations with respect to the substrate were prepared using standard lift-off lithography techniques (see the appendix for the photolithography techniques in section 6.2).

Next, we turn our attention to examining IL-DMI's effect on a magnetic bilayer system featuring orthogonal magnetizations. Mathematically, the interaction can be represented by the overall Hamiltonian [16,61]:

$$\widehat{\mathrm{H}} = \boldsymbol{J_H} \boldsymbol{M}_1 \cdot \boldsymbol{M}_2 - \boldsymbol{D} \cdot (\boldsymbol{M}_1 \times \boldsymbol{M}_2) \tag{2.1}$$

Eqn. (2.1) comprises two parts, the conventional symmetric (Heisenberg) exchange term and the antisymmetric (DMI) term [25,55], respectively. Here, $\boldsymbol{J_H}$ represents the Heisenberg exchange integral, $\boldsymbol{M}_{1,2}$ denote the magnetizations of the two magnetic layers, and $\boldsymbol{D}$ is the characteristic DMI vector dictating the strength and orientation of the IL-DMI. As the two magnetizations naturally adopt an orthogonal configuration, contribution from the Heisenberg exchange term to the Hamiltonian is conveniently

doi:10.6342/NTU202404434

discarded, while the DMI term is maximized. Considering that the degree and orientation of symmetry breaking are determined by the sputtering process, $\boldsymbol{D}$ is expected to be fixed and lie within the xy plane due to symmetry constraints [15,64,65]. The system's Hamiltonian is therefore governed by a cross product term:

$$\widehat{\mathrm{H}}_{\mathrm{DMI}} = -\boldsymbol{D} \cdot (\boldsymbol{M}_1 \times \boldsymbol{M}_2). \tag{2.2}$$

Drawing analogy from the well-known Zeeman Hamiltonian $\widehat{\mathrm{H}}_{\mathrm{Zeeman}} = -\boldsymbol{m} \cdot \boldsymbol{H}$ where $\boldsymbol{m}$ is the magnetic moment and $\boldsymbol{H}$ represents the external field, we can infer that macroscopically, the IMA layer exerts an effective field on the PMA layer, and vice versa. Specifically, if $\boldsymbol{M}_1$ and $\boldsymbol{M}_2$ in eqn. (2.2) are selected as $\boldsymbol{M}_{\mathrm{PMA}}$ and $\boldsymbol{M}_{\mathrm{IMA}}$, respectively, then the PMA (Co) layer experiences the DMI effective field:

$$\boldsymbol{H}_{\mathrm{DMI}} = -\boldsymbol{D} \times \boldsymbol{M}_{\mathrm{IMA}} \tag{2.3}$$

while the IMA (CoFeB) layer encounters an effective field:

$$\boldsymbol{H}_{\mathrm{DMI}} = \boldsymbol{D} \times \boldsymbol{M}_{\mathrm{PMA}} \tag{2.4}$$

For instance, if the direction of $\boldsymbol{D}$ points toward $\varphi_D = 150^{\circ}$ (where φ_D represents $\boldsymbol{D}$'s angle relative to x axis) then when $\boldsymbol{M}_{\mathrm{IMA}}$ is pinned at $\varphi_H = 60^{\circ}$ (with φ_H representing the applied in-plane field's angle $\boldsymbol{H}_{\varphi}$), the $\boldsymbol{H}_{\mathrm{DMI}}$ exerted on $\boldsymbol{M}_{\mathrm{PMA}}$ is maximized and points toward $+z$ direction. Conversely, when $\boldsymbol{M}_{\mathrm{PMA}}$ points toward $+z$, $\boldsymbol{H}_{\mathrm{DMI}}$ exerted on $\boldsymbol{M}_{\mathrm{IMA}}$ points toward $\varphi_H = 60^{\circ}$ (Fig. 2-3(a) left).

doi:10.6342/NTU202404434

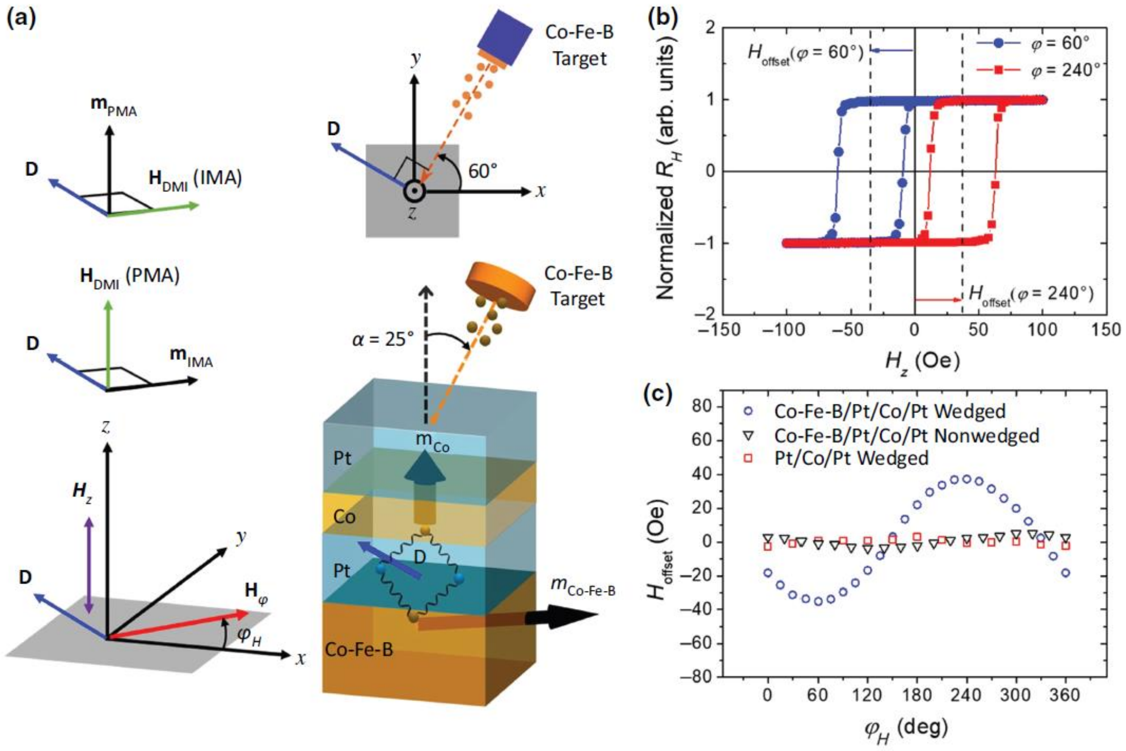

Fig. 2-3 Overview of the magnetic multilayers' geometry, external fields, coordinate system, and the manifestation of IL-DMI on PMA's hysteresis loops. (a) The multilayer structure is depicted, with the CoFeB atom flow tilted away from the substrate normal at an angle of α=25°. The coordinate system and the geometries of the external fields are illustrated in the lower left diagram. The cross-product relationships between $\boldsymbol{M}_{\text{IMA}}$, $\boldsymbol{M}_{\text{PMA}}$, $\boldsymbol{D}$ and H_{DMI} (PMA and IMA) are showcased in the upper left diagram, while the upper right diagram indicates the correlation between CoFeB atom flow direction and the direction of $\boldsymbol{D}$. (b) Representative Hall resistance hysteresis loops were measured by sweeping $\boldsymbol{H}_{\text{z}}$ field while simultaneously applying a constant field $\boldsymbol{H}_{\varphi}$ in the xy plane (see (a)). The blue and red datasets correspond to $\varphi_H = 60°$ and 240°, respectively, with a magnitude of $|\boldsymbol{H}_{\varphi}| = 300$ Oe. (c) H_{offset} as a function of φ_H. Three samples are demonstrated: the fully wedged CoFeB(2)/Pt(2.5)/Co(0.6)/Pt(2.5) sample along with two control samples, namely fully wedged Pt(2.5)/Co(0.6)/Pt(2.5) and non-wedged

CoFeB(2)/Pt(2.5)/Co(0.6)/Pt(2.5). Reprinted from [53].

Next, a field sweep protocol is developed to evaluate the behavior of the CoFeB(2)/Pt(2.5)/Co(0.6)/Pt(2.5) wedged-deposited structure which was patterned into a Hall bar device. The in-plane field $\boldsymbol{H}_{\varphi}$ is applied to fully align $\boldsymbol{M}_{\mathrm{IMA}}$ along φ_H. It's important that $|\boldsymbol{H}_{\varphi}|$ must be sizable to prevent the reciprocal $\boldsymbol{H}_{\mathrm{DMI}}$ (from $\boldsymbol{M}_{\mathrm{PMA}}$) and possible in-plane anisotropy from causing unwanted misalignment of $\boldsymbol{M}_{\mathrm{IMA}}$. Simultaneously, a field sweep is executed in the ±z direction to capture the hysteresis behavior of $\boldsymbol{M}_{\mathrm{PMA}}$ by R_H measurement. These procedures are graphically represented in Fig. 2-3(a) lower left panel. Fig. 2-3(b) illustrates two hysteresis loops of the Co layer subject to two different in-plane field angles, namely $\varphi_H = 60^{\circ}$ and 240° with $|\boldsymbol{H}_{\varphi}| = 300$ Oe. Square hysteresis loops indicate robust PMA character of the Co layer, with a coercive field $H_c = 25$ Oe. These two hysteresis loops exhibit significantly shifted switching boundaries, and we define the horizontal shift of the loop centers, H_{offset}, as the average of the two switching fields of magnetization's down-to-up and up-to-down transitions. This substantial H_{offset} contrasts sharply with the two control samples, namely the wedged Pt(2.5)/Co(0.6)/Pt(2.5) and non-wedged CoFeB(2)/Pt(2.5)/Co(0.6)/Pt(2.5), wherein PMA hysteresis loops are consistently symmetrical with respect to the origin, where negligible H_{offset} (< 2 Oe) are observed regardless of φ_H (Fig. 2-3(c)). Note that data from the two control samples also serve to demonstrate the precision of our meticulously calibrated vector magnet (Model 5204, GMW associates) [72], thereby eliminating possible innate asymmetries that can stem from the vector magnet.

Following the identical field sweep protocol with a constant magnitude of $|\boldsymbol{H}_{\varphi}| =$ 300 Oe as φ_{H} was gradually rotated from 0 to 360°, H_{offset} as a function of φ_H is shown in Fig. 2-3(c). The clear sinusoidal dependence of H_{offset} on φ_{H} confirms the predicted IL-

doi:10.6342/NTU202404434

DMI effective field to be in the cross product form of $-\boldsymbol{D} \times \boldsymbol{M}_{\mathrm{IMA}}$. Sine fit to the data $H_{\mathrm{offset}} = H_{\mathrm{DMI}} \sin(\varphi_{\mathrm{H}} - \varphi_{\mathrm{D}})$ yields an amplitude of $H_{\mathrm{DMI}} = 37$ Oe and φ_{D} of 150° for this particular sample. This H_{DMI} amplitude of 37 Oe is comparable to findings reported by Han et al.[58] albeit much smaller than in Ref. [65]. This variance is attributed to the significantly thicker Pt spacer, which may weaken the long-range indirect exchange interaction. Importantly, the $\boldsymbol{D}$ direction with respect to the x axis (φ_{D}) is observed to be perpendicular to the CoFeB's atom flow direction (Fig. 2-3(a) upper right), in agreement with the 3rd Moriya rule [16] where the $\boldsymbol{D}$ vector must be perpendicular to the mirror plane. One can also perceive as follows: with the only remaining symmetry operation being a mirror along the wedge direction, a perpendicular $\boldsymbol{D}$ alignment with the direction of the wedge enables the H_{DMI} landscape to be symmetrical across this mirror.

These observations unequivocally illustrate that $\boldsymbol{M}_{\mathrm{PMA}}$ is influenced by a sizable IL-DMI coupling. Other commonly encountered coupling effects, such as RKKY coupling, dipolar coupling [73] or symmetric interlayer exchange coupling, all belong to the realm of symmetric exchange interactions and thus cannot account for the chiral nature of our findings. The identical thickness of 2.5 nm of the two Pt layers (self-countering spin current) alongside low probing current density of less than 1.32×10^{10} A/m^2 also excludes symmetry breaking contribution from SOT induced hysteresis loop-shift [66,74,75], ruling out the possibility of intralayer DMI serving as the origin of the observed phenomenon.

In addition, H_{offset} as a function of φ_H while varying the strength $|\boldsymbol{H}_{\varphi}|$ from 10 Oe to 300 Oe is depicted in Fig. 2-4(a). As $|\boldsymbol{H}_{\varphi}|$ increases from 100 Oe to 300 Oe, the behavior of H_{offset} with respect to φ_H nicely follows a sinusoidal trend with consistent magnitude of H_{DMI} and $\boldsymbol{D}$ vector direction. Fig. 2-4(b) presents H_{offset} as a function of H along $\varphi_H = 90°$

doi:10.6342/NTU202404434

with dashed lines serving as guide to the eyes. This clear saturation behavior shows that once the IMA magnetization is properly aligned by a high enough $\boldsymbol{H}_\varphi$, H_{offset} is maximized to the magnitude of $\boldsymbol{H}_{\mathrm{DMI}} = -\boldsymbol{D} \times \boldsymbol{M}_{\mathrm{IMA}}$. On the contrary, when $|\boldsymbol{H}_\varphi|$ decreases to below 100 Oe, the $H_{\mathrm{offset}}-\varphi_H$ behavior deviates from a sinusoid, possibly due to the reciprocal H_{DMI} exerted on $\boldsymbol{M}_{\mathrm{IMA}}$ alongside the existence of an in-plane uniaxial magnetic anisotropy (see section 3.2). This clear saturation behavior with external field is a trademark of IL-DMI, differentiating itself from the tilted magnetic easy axis scenario, where the H_{offset} possesses a linear trend with regard to the magnitude of $|\boldsymbol{H}_\varphi|$ [76,77].

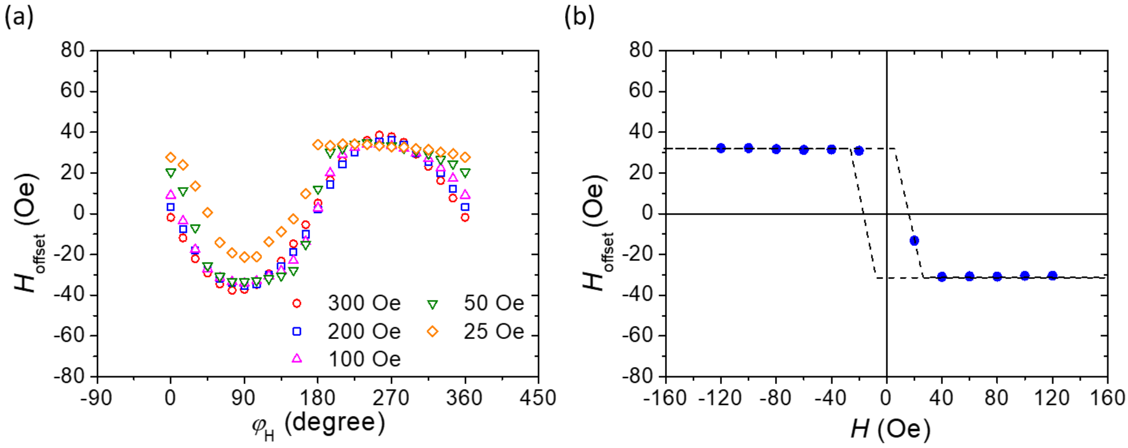

Fig. 2-4 (a) H_{offset} as a function of φ_H, where in-plane field $\boldsymbol{H}_\varphi$'s strength varies from 25 to 300 Oe. (b) H_{offset} under varying in plane field H. the direction of here H is along φ_H = 90°. Note the clear saturation of H_{offset} toward H_{DMI} at large enough H. Figure adapted from [53].

Following the established protocol, we manufactured a second batch of samples featuring an identical layer structure but with Hall bar devices arranged in sequential 30° rotations in the xy plane. This was done to assess the universality of the wedge-induced in-plane symmetry breaking. The devices with varying orientations are grown on a 1 cm × 1 cm substrate labeled A to F (Fig. 2-5(a)). H_{offset} was measured for each device, with the six samples having independent x_iy_i and $\varphi_{H,\,i}$ coordinates. The data sets for the six devices are presented in Fig. 2-5(b) with solid lines representing sine fits to the data. It's notable that the six sinusoidal fits not only exhibit a similar magnitude of $H_{\text{DMI}} = 30 \pm 2$ Oe, but also show a consistent shift in $\varphi_{H,\,I}$ dependence at constant intervals of approximately 30° from device A to F. After recalculating to convert $\varphi_{H,\,i}$ back into the substrate's xy coordinates (refer to Fig. 2-5(a)) and compiled the value of H_{DMI} and φ_D in Fig. 2-5(c), both H_{DMI} and φ_D were found to be universal across all six rotary devices. This result highlights the effectiveness of the wedge deposition due to the agreement between the symmetry constraints and the relative angle between the wedge direction and the $\boldsymbol{D}$ direction. This is in contrast from the other works [63,65] which reported random D directions from device-to-device, and this consistently makes it much more reliable in any potential practical applications.

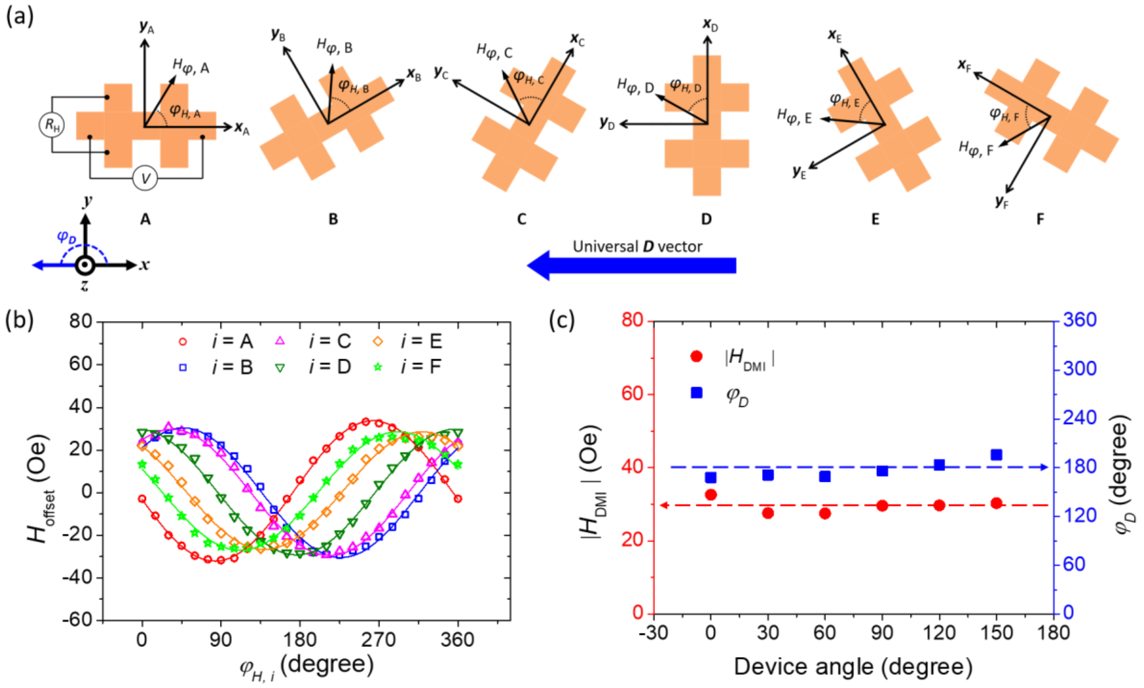

Fig. 2-5 Demonstration of universal IL-DMI. (a) Illustration of six rotating Hall cross devices, labeled device A to F. These devices feature current channel directions rotated at 30° intervals, each characterized by its independent x_iy_i and $\varphi_{H,\ i}$ coordinates, distinguishing their respective field sweeping procedures. (b) Results obtained from hysteresis loop-shift measurements induced by IL-DMI, with different coordinate systems utilized for each individual device. Solid lines represent sine fits to the data, with $|\boldsymbol{H}_\varphi|$ = 300 Oe maintained throughout. (c) Compiled φ_D and H_{DMI} extracted from sine fit in (b). φ_D is recalculated back to the xy coordinate system of the substrate. Figure adapted from [53].

2.2 Reciprocal Effect and Energy Density

As seen in section 2.1.2, the IL-DMI is a reciprocal effect. While we previously focused on the response of the PMA layer, an effective field in the form of $\boldsymbol{H}_{\mathrm{DMI}} = \boldsymbol{D} \times \boldsymbol{M}_{\mathrm{PMA}}$ is also exerted on the IMA layer. This effective field should manifest itself as a hysteresis loop shift of $\boldsymbol{M}_{\mathrm{IMA}}$, where our homemade MOKE system is employed to accurately capture the hysteresis shift of $\boldsymbol{M}_{\mathrm{IMA}}$ relying on its high accuracy thanks to the Helmholtz coil. Here, the results captured by the MOKE are separated into two scenarios in the following. Note that due to the IL-DMI effective fields exist for both $\boldsymbol{M}_{\mathrm{PMA}}$ and $\boldsymbol{M}_{\mathrm{IMA}}$, the H_{DMI} will be specifically labeled in this section.

In the first case, we focus on a sample (same as the one in Fig. 2-5) with its PMA layer experiencing an H_{DMI} (PMA) higher than its coercive field. Since $\boldsymbol{D}$ points in the -x direction as seen in Fig. 2-5(a), the external in-plane field provided by the Helmholtz coil is set along ± y directions to maximize the magnitude of H_{DMI} (IMA), and the MOKE system set to the perpendicular configuration to detect the Co magnetization. The results are shown in Fig. 2-6, where the PMA magnetization is switched by an in-plane field. This is a coherent switching process, in which the external in-plane field switches $\boldsymbol{M}_{\text{IMA}}$ (from + y to -y, for example) and then due to high H_{DMI} (PMA) of 30 Oe directly overpowering the $H_c \approx 25$ Oe, $\boldsymbol{M}_{\text{PMA}}$ experiences magnetization switching as well. This is a fascinating result in the sense that manipulation of one magnetization is transposed to an orthogonal axis by IL-DMI, and the switching polarity can be controlled by the external field's orientation with regard to $\boldsymbol{D}$. We'll see in the next section how this special trait enables potential utilization in practical memory devices.

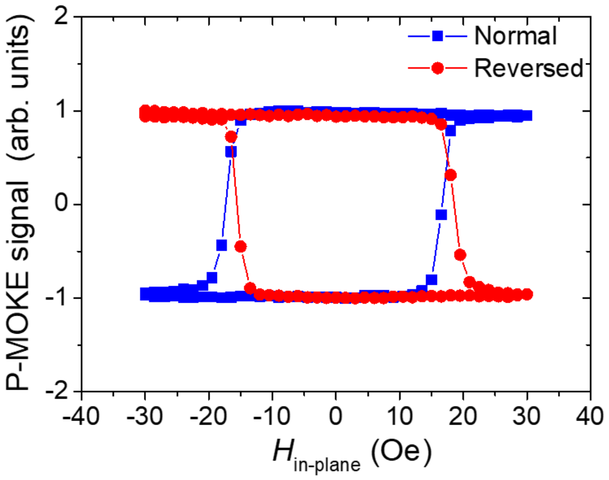

Fig. 2-6 PMA Co switching induced by in-plane field, measured by P-MOKE. Normal (red data set) hysteresis loop have the $H_{\text{in-plane}}$'s positive direction in the + y direction while the reversed (blue data set) have the $H_{\text{in-plane}}$'s positive direction in the – y direction. Note that the L-MOKE signal is flooded by P-MOKE due to the naturally much higher Kerr rotation in P-MOKE measurement [78], the coherent switching also renders $\boldsymbol{M}_{\text{IMA}}$ hysteresis loop invisible. Figure reprinted from [53].

In the second case, due to IL-DMI entangling $\boldsymbol{M}_{\text{IMA}}$ and $\boldsymbol{M}_{\text{PMA}}$'s switching processes (as shown in Fig. 2-6), a CoFeB(2)/Pt(2.5)/Co(0.8)/Pt(2.5) sample with a slightly thicker Co layer is thus separately fabricated to increase the Co ($\boldsymbol{M}_{\mathrm{PMA}}$) layer's coercive field, thereby avoiding such coherent switching. Fig. 2-7(a) shows the out-of-plane H_{offset} of the Co PMA layer ($\boldsymbol{M}_{\mathrm{PMA}}$) as a function of the applied in-plane field direction φ_H, indicating a H_{DMI} of 25.8 Oe and $\boldsymbol{D}$ vector direction of 67°. We then employ the L-MOKE system to capture the hysteresis shift of $\boldsymbol{M}_{\mathrm{IMA}}$. The sample is first subject to an initialization field to fix $\boldsymbol{M}_{\mathrm{PMA}}$ toward $\pm z$ prior to measurement. L-MOKE results showing hysteresis behaviors of $\boldsymbol{M}_{\mathrm{IMA}}$ are reported in Fig. 2-7(b), with the external field's direction parallel to -23°, the direction where H_{DMI} (IMA) is maximized. We can compare this H_{DMI} (IMA) of about 13.8 Oe to the H_{DMI} (PMA) of 25.8 Oe by utilizing the DMI energy term [62,65]:

$$E_{\mathrm{DMI}} = \mu_0 M_{\mathrm{s}} H_{\mathrm{DMI}} t_{\mathrm{FM}} \tag{2.5}$$

where μ_0 is the vacuum permittivity, M_{s} the saturation magnetization and t_{FM} the magnetic layer thickness. Using previously measured values from our lab of $M_{\mathrm{s}}^{\mathrm{CoFeB}} = 0.86 \times 10^6$ A/m and $M_{\mathrm{s}}^{\mathrm{Co}} = 1.18 \times 10^6$ A/m [79], we calculated $E_{\mathrm{DMI}}^{\mathrm{Pt/Co}} = 2.41$ μJ/m^2 and $E_{\mathrm{DMI}}^{\mathrm{CoFeB/Pt}} = 2.34$ μJ/m^2 from eqn. (2.5). Note that this value is much smaller than the conventional interfacial DMI's typical strength of 0.05 ~ 0.5 mJ/m^2 [47,66,80] due to the longer exchange length. Importantly, since the two magnetic layers are mediated by the exact same IL-DMI, this decent mutual agreement of the estimated DMI energy confirms the reciprocity of the IL-DMI.

Overall, both the coherent switching and hysteresis shift of $\boldsymbol{M}_{\mathrm{IMA}}$ solidly confirms the reciprocity of the interlayer DMI.

doi:10.6342/NTU202404434

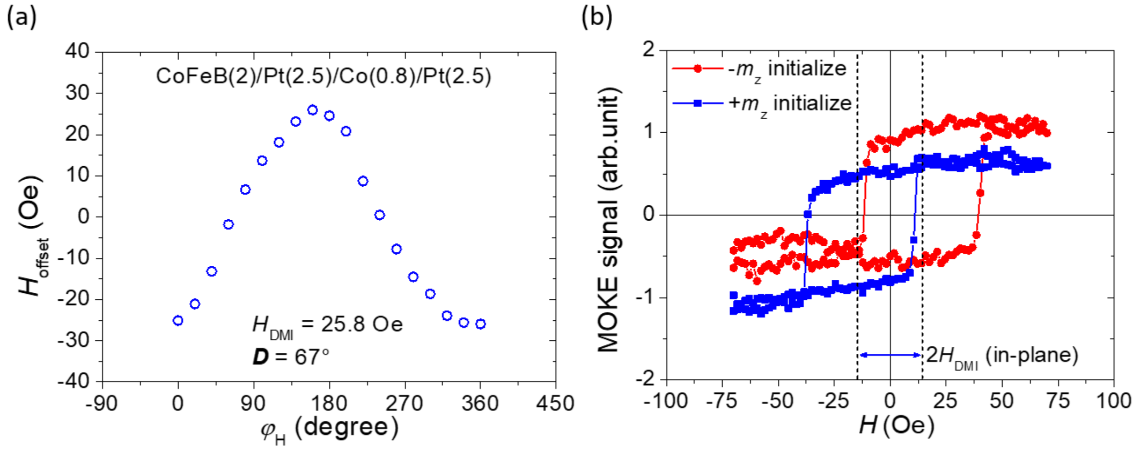

Fig. 2-7 (a) H_{offset} of the perpendicularly-magnetized Co layer as a function of in-plane applied filed direction φ_H. Sine fitting reveals the H_{DMI} (PMA) strength and the $\boldsymbol{D}$ vector direction. (b) L-MOKE results showing $\boldsymbol{M}_{\text{IMA}}$ hysteresis loop-shift which is dependent on $\boldsymbol{M}_{\text{z}}$'s direction. Figure reprinted from [53].

2.3 IL-DMI's role in Current-Induced Field-Free Switching

The coherent switching of both magnetizations under in-plane field reported in Fig. 2-6 and the universal behavior induced by wedge deposition in Fig. 2-5 inspired us to explore the possibility of harnessing IL-DMI as a symmetry-breaking element in achieving field-free current-driven magnetization switching. Conventional SOT mechanisms, constrained by in-plane spin polarization [81-83], cannot enable deterministic magnetization switching of a PMA magnetization without applying an external field along the current direction (H // x axis) to break the mirror symmetry (the mirror being the xy plane). Prior to our investigations, Numerous means have been proposed to bypass this external field requirement and achieve a purely current-driven switching. These methods include employing an intralayer DMI [84], introducing tilted magnetic anisotropy into $\boldsymbol{M}_{\text{PMA}}$ [77,85,86], exploiting exchange bias [87-89] and utilizing epitaxial materials with low symmetry [81,90].

Here, it is hypothesized that during magnetization of the IMA layer, the polarity of the IL-DMI effective field exerted on the PMA layer may also reverse, potentially creating preference in the energy landscape between the up/down magnetization states, or facilitating outright switching of $\boldsymbol{M}_{\mathrm{PMA}}$ (analogous to the Zeeman energy from an external z-directional field). Moreover, as the cross product of the two vectors "$\boldsymbol{M}_{\mathrm{IMA}}$" and "$\boldsymbol{D}$" determines the orientation and strength of the DMI effective field, the switching polarity of $\boldsymbol{M}_{\mathrm{PMA}}$ could be well controlled. With the $\boldsymbol{D}$ vector engineered to point toward the $-x$ direction (identical to the growth condition of Fig. 2-5), the landscape of H_{DMI} acting on $\boldsymbol{M}_{\mathrm{PMA}}$ is illustrated in Fig. 2-8(a). $\boldsymbol{D}$ separates the xy plane into two parts, when $\boldsymbol{M}_{\mathrm{IMA}}$ lies within the first and second quadrants ($0° < \varphi_M < 180°$), H_{DMI} points towards the $+z$ direction and reaches maximum at $\varphi_M = 90^{\circ}$. Conversely, H_{DMI} points towards the $-z$ direction and reaches its minimum at $\varphi_M = 270°$ when φ_M lies within the third and fourth quadrants ($180^{\circ} < \varphi_M < 360^{\circ}$).

From these observations, a model containing two geometries featuring current channels striking at angles of 45° (left) and 135° (right) with respect to the x-axis are showcased with rotary devices in Fig. 2-8(b). For the 45° device, the applied pulse current (I_{pulse}) induces magnetization switching of $\boldsymbol{M}_{\mathrm{IMA}}$ under a standard type-y scheme [91], leading to two possible states of $\varphi_M = 135°$ ($-45°$) when I_{pulse} is positive (negative) and surpasses the critical switching threshold. In the scenario where $\varphi_M = 135°$, $\boldsymbol{M}_{\mathrm{PMA}}$ orients toward the $+z$ direction owing to the corresponding positive H_{DMI} while an alignment along $-z$ is expected due to a negative H_{DMI} when $\varphi_M = -45°$. A similar scenario is depicted in the 135° device, albeit with the orientational dependence of the current polarity for $\boldsymbol{M}_{\mathrm{PMA}}$ being opposite to that of the 45° device. Overall, this model

doi:10.6342/NTU202404434

could be viewed as a coherent switching behavior where the external in-plane field is replaced by current-induced spin torque.

The validity of the aforementioned model was confirmed through current-induced magnetization switching measurements conducted on a magnet-free probe station. Current pulses of various amplitudes and a pulse width of 50 ms were utilized. In Fig. 2-8 (c) and (d), one can see that deterministic switching of the PMA layer is successfully achieved for both the 45° and 135° devices (blue data set). Remarkably, not only are the switching polarities of the two devices opposite, but they also precisely adhere to the IL-DMI effective field's landscape, which describes the response of $H_{\rm DMI}$ with regard to φ_M. Moreover, our model also implicitly suggests that the two magnetizations involved should switch coherently wherein $\boldsymbol{M}_{\rm IMA}$ and $\boldsymbol{M}_{\rm PMA}$ should share an identical switching current.

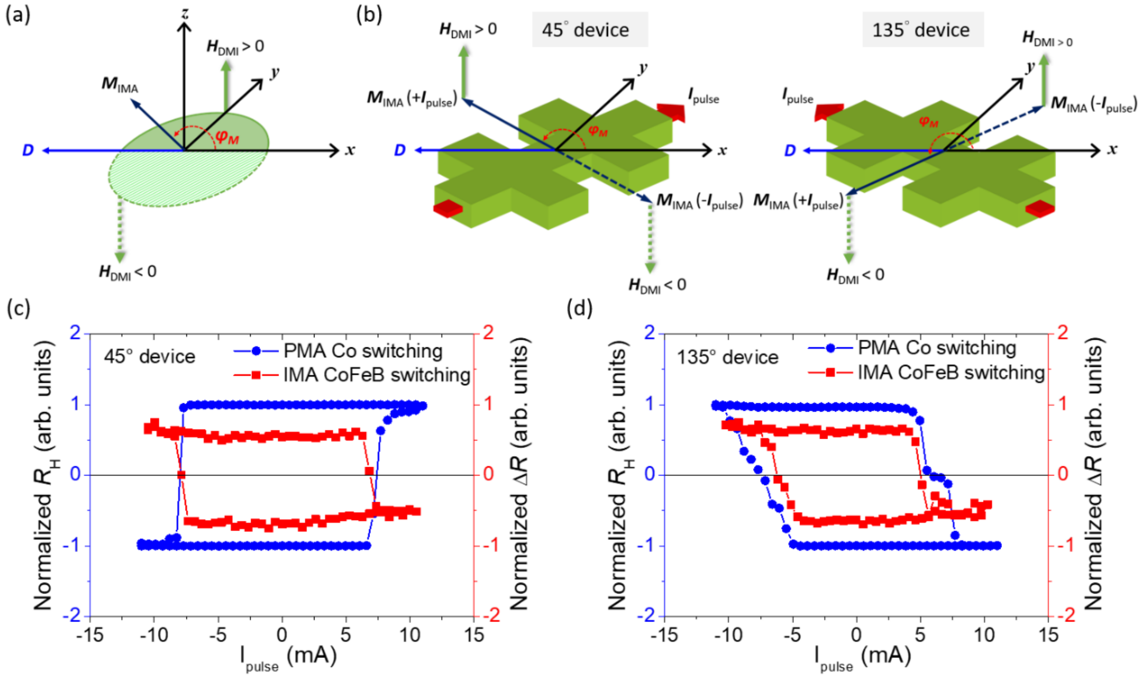

Fig. 2-8 Modelling and experimental demonstration of current-driven field-free switching induced by IL-DMI. (a) Schematics of the orientational relationships between $\boldsymbol{D}$ vector, $\boldsymbol{M}_{\rm IMA}$ and the corresponding $\boldsymbol{H}_{\rm DMI}$. (b) Illustration of two devices positioned on the same

substrate, with their respective current channel directions striking angles of 45° and 135° with respect to the x-axis, respectively. Employing the Oersted field and/or type-y SOT switching scheme enables $\boldsymbol{M}_{\mathrm{IMA}}$ switching between two states, eliciting H_{DMI} response with opposite polarity. (c) and (d) showcase current-induced magnetization switching loops of both $\boldsymbol{M}_{\mathrm{PMA}}$ and $\boldsymbol{M}_{\mathrm{IMA}}$ under field-free condition. Figure adopted from [53].

Consequently, we conducted consecutive current scans immediately following PMA switching, during which the UMR detection technique was utilized to probe the switching behavior of $\boldsymbol{M}_{\mathrm{IMA}}$ (Fig. 2-8(c) and (d), red data set). Clearly, $\boldsymbol{M}_{\mathrm{IMA}}$ indeed experiences magnetization switching, and its critical switching current in both 45° and 135° devices aligns relatively well with that of the $\boldsymbol{M}_{\mathrm{PMA}}$ switching data, thus confirming coherent switching. It's observed that the switching currents of the IMA layer are consistently slightly lower than those of the PMA layer. During the PMA (Co layer) switching experiments, the Hall cross (intersection) region predominantly contributes to the Hall signal. For the IMA (CoFeB layer) switching, in contrast, the UMR detects signals primarily originating from the Hall-bar (longitudinal) region. Due to the naturally higher current density in the longitudinal region [92], this discrepancy explains the slightly lower switching current observed by the UMR.

In contrast to the PMA switching scheme, the switching polarity of the IMA layer remain unchanged across both devices, as seen in Fig. 2-8(c) and (d). This consistency arises from the fact that in-plane magnetization switching occurs through the current-induced Oersted field and/or Spin-Orbit Torque (SOT) originating from the adjacent Pt layer. Consequently, the switching curve is solely dictated by the polarity of I_{pulse}, independent of the direction of $\boldsymbol{D}$. Another important evidence lies in the fact that due to the symmetrical thicknesses of the Pt layers sandwiching the Co layer, SOT induced effect exerted on $\boldsymbol{M}_{\mathrm{PMA}}$ is in fact negligible. As seen in Fig. 2-9, the near-zero DL-SOT effective field is a testament to that the current-induced magnetic switching of $\boldsymbol{M}_{\mathrm{PMA}}$ is propelled entirely by H_{DMI}.

Overall, the clear coherent switching behavior of both the PMA and IMA magnetizations we've observed is the first field-free switching via IL-DMI in a orthogonally magnetized system, as well as the first direct experimental evidence of IL-DMI's involvement in mediating current-induced field-free switching, where contemporary research resorted to micromagnetic simulations [60,62] to validate their findings. We assert that the switching process is unaffected by magnetic history, as both magnetizations are simultaneously reinitialized under applied current, ensuring consistent polarity retention. This stands in contrast to other field-free approaches reliant on mechanisms such as exchange bias, the orange peel effect [83,93] or exotic spin currents [81]. Furthermore, the minimal SOT acting on $\boldsymbol{M}_{\mathrm{PMA}}$ distinguishes this IL-DMI mechanism from the previously reported type-T scenario [] where the magnetic coupling is symmetric, and PMA switching necessitates substantial SOT.

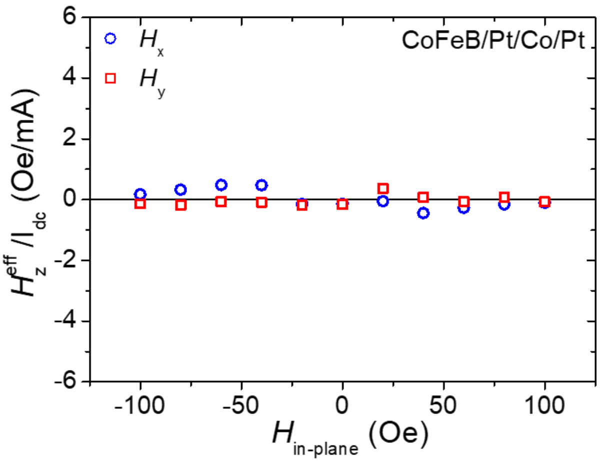

Fig. 2-9 SOT induced effective field captured by current-induced loop-shift measurement [66]. The extremely low DL-SOT effective field of less than 0.5 Oe/mA, regardless of the

in-plane field’s strength or direction, is evident.

Lastly, we demonstrate the feasibility to replace the in-plane magnetized amorphous CoFeB layer by the (presumably polycrystalline) permalloy (Py) layer. The sample used in this set of measurements is a wedge deposited Py(5)/Pt(2.5)/Co(0.6)/Pt(2.5) multilayer. Following procedures identical to the main text, a sizable H_{DMI} and the universality of the IL-DMI effect over a considerably sized substrate is again confirmed, as shown in Fig. 2-10 (a)-(c). Current-induced field-free switching measurements are also performed using two devices, Fig. 2-10 (d) shows the switching behavior of the 30° and 120° devices which are on the opposite sides of the IL-DMI landscape (see Fig. 2-8(a)). As expected, their respective switching polarities are opposite to each other.

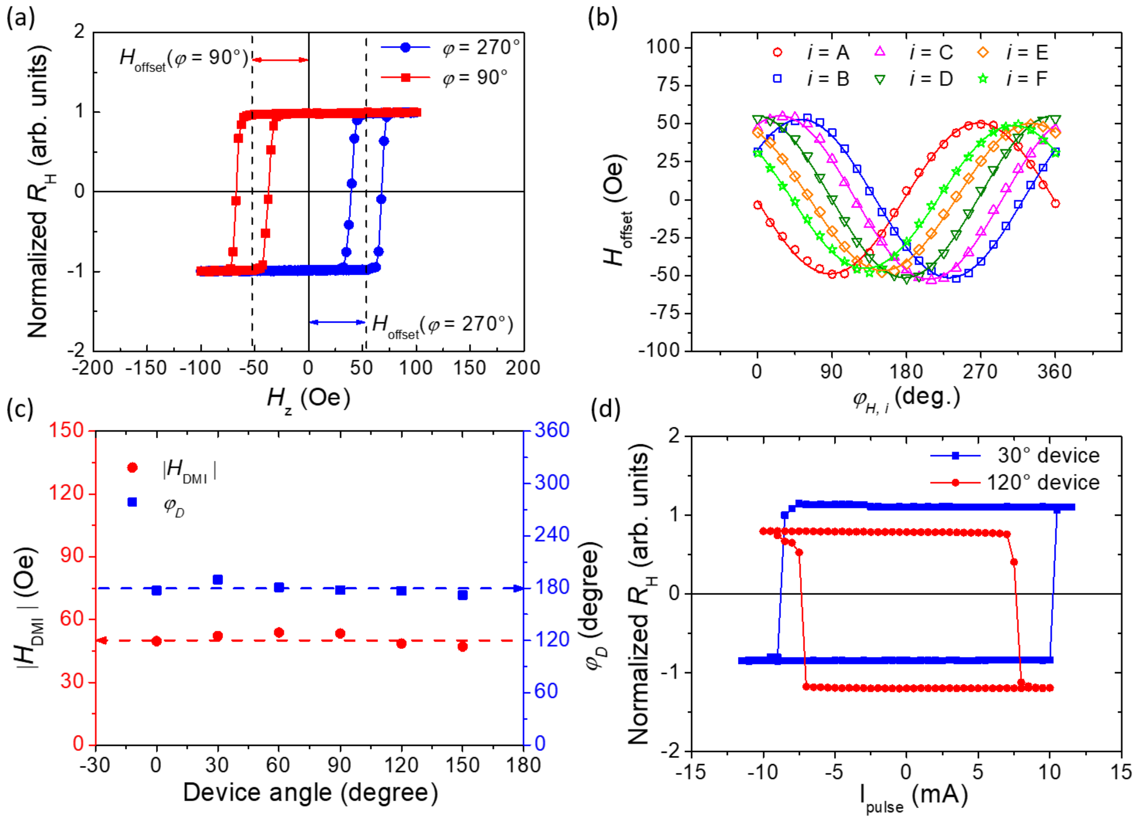

Fig. 2-10 (a) Representative Hall resistance loops of Py(5)/Pt(2)/Co(0.6)/Pt(2) with identical field scan protocol to that described in the main text, with $|\boldsymbol{H}_{\varphi}| = 300$ Oe. (b) IL-DMI coupling induced hysteresis loop-shift measurements on rotary devices. Geometry of the devices are identical to the ones showed in Fig. 2-5. The recalculated compilation of φ_D and H_{DMI} are plotted in (c). (d) Field free switching of two devices, 30° and 120° denotes the angle between the current channel and the x axis. Similar to the CoFeB case described previously, the field free switching's polarity is dictated by the IL-DMI effective field landscape. Reprinted from [53].

2.4 Brief Conclusions

In this chapter, we have successfully demonstrated the existence of a substantial IL-DMI within a magnetic multilayer system with orthogonal magnetizations. Experimental verification of this IL-DMI was achieved through a meticulously calibrated field sweep procedure, revealing its chiral nature with an effective field, H_{DMI} of 37 Oe. Comparison with control samples pinpoint IL-DMI's origin to the wedge deposition induced in-plane symmetry breaking, which is also supported by symmetry. Characterizations of devices featuring multiple orientations on the same substrate have highlighted the universal strength and direction of such interactions, proving advantageous for wafer-scale integration. Moreover, through deterministic field-free magnetization switching experiments, we have demonstrated all-electric (current-driven) manipulation of 3D magnetic textures, well explained by a model based on IL-DMI.

There remain several unresolved mysteries and challenges in the field. For instance, while the generation of IL-DMI using oblique angle deposition is supported by symmetry analysis, a detailed study into the physical origin of IL-DMI has yet to be reported.

doi:10.6342/NTU202404434

Another issue, as highlighted by Vedmedenko et al. [94], is the notably low exchange strength E_{DMI} (reported at ≈ 2.4 μJ/m^2 here). Enhancements are necessary to make IL-DMI more appealing for advanced applications such as three-dimensional arrays of chiral magnetic objects or chiral logic circuits [95,96]. In addition, research into novel spacer materials beyond Pt is imperative to enable more efficient control over IL-DMI. In the subsequent sections, significant advancements will be showcased, aimed to at least partially address these mysteries and challenges.

doi:10.6342/NTU202404434

Chapter 3 IL-DMI's Comparison with other Symmetry Breaking effects

Our focus now shifts towards exploring various symmetry-breaking effects. In Chapter 2, we delved into our initial findings regarding the emergence of IL-DMI, its quantitative assessment, and its demonstrated potential for practical applications in enabling current-induced field-free switching in a PMA magnetization. Here, we conduct a comparative analysis between IL-DMI and another significant symmetry-breaking effect: the tilting of magnetic anisotropy in the PMA layer, to elucidate their respective roles in achieving field-free switching. Additionally, current-induced loop shift measurements are performed to rule our other potential mechanisms. On the other hand, while it has been established that both tilted magnetic anisotropy and IL-DMI can originate from the wedge deposition process, we investigate a suggested alternative means of achieving in-plane symmetry breaking: sample growth with an external in-plane field H_{ext} (as shown in Fig. 2-2(b)). We aim to determine this method's efficacy at generating substantial IL-DMI with the predicted characteristic $\boldsymbol{D}$ directions. This chapter contains content refined from my published article "Field-Free Switching in Symmetry-Breaking Multilayers: The Critical Role of Interlayer Chiral Exchange" [97] along with unpublished research focused on relations (or the lack of) between in-plane magnetic anisotropy and IL-DMI.

doi:10.6342/NTU202404434

3.1 Comparative study of IL-DMI versus Tilted Anisotropy

3.1.1 Magnitudes of IL-DMI and Tilted Anisotropy

The significance of this comparative analysis lies in the fact that similar to the IL-DMI, generation of tilted PMA magnetic anisotropy in a Pt/Co based structure is also often attributed to the oblique deposition process. Certain works using oblique deposition concluded the thickness difference to be the source of the tilted magnetic anisotropy [76,98], as schematically shown in Fig. 3-1(a) (though as we shall see in section 4.3 as well in [99], this thickness gradient is miniscule across a single device), while a more recent publication connected its origin with tilted Pt(111) texture, deviating away from the *z* axis [86]. In addition, while IL-DMI and tilted PMA anisotropy have significantly different origins, due to them originating from an identical in-plane symmetry breaking factor, their individual contributions can be difficult to separate. For example, Kim et. al. [77] demonstrates that in a system with tilted magnetic anisotropy, the hysteresis shift of the PMA layer is linear with regard to the external in-plane field parallel to the tilting axis, as shown in Fig. 3-1(b). This linear behavior is almost identical with the response from a double-PMA system mediated by IL-DMI (discussed later in sec. 4.1.2 and ref. [62]). Most importantly, field-free switching of a PMA magnetization can be achieved utilizing tilted magnetic anisotropy as well. Under conventional *y* spin generated from the spin Hall effect, the magnetization, when activated by a sufficiently large current and aligns parallel to the *y* axis, has a clear energy preference and deterministically relaxes to ± easy axis direction, as demonstrated in Fig. 3-1(c). This energy preference is equivalent to a *x* directional effective field, as captured by current-induced hysteresis loop-shift measurement (Fig. 3-1(d)) [86].

doi:10.6342/NTU202404434

To quantitatively separate the contributions from IL-DMI and tilted PMA anisotropy, and especially to identify the dominating factor in assisting field-free switching, we selected type-T structures with repeating $[Pt/Co]_n$ stacks serving as the PMA layers to generate different DMI exchange length, while simultaneously inducing variations in the tilting angle due to the different amount of wedged layers. By looking at the field scan and current switching behaviors of these multilayer stacks, a comparative study of IL-DMI and tilted PMA anisotropy is obtained.

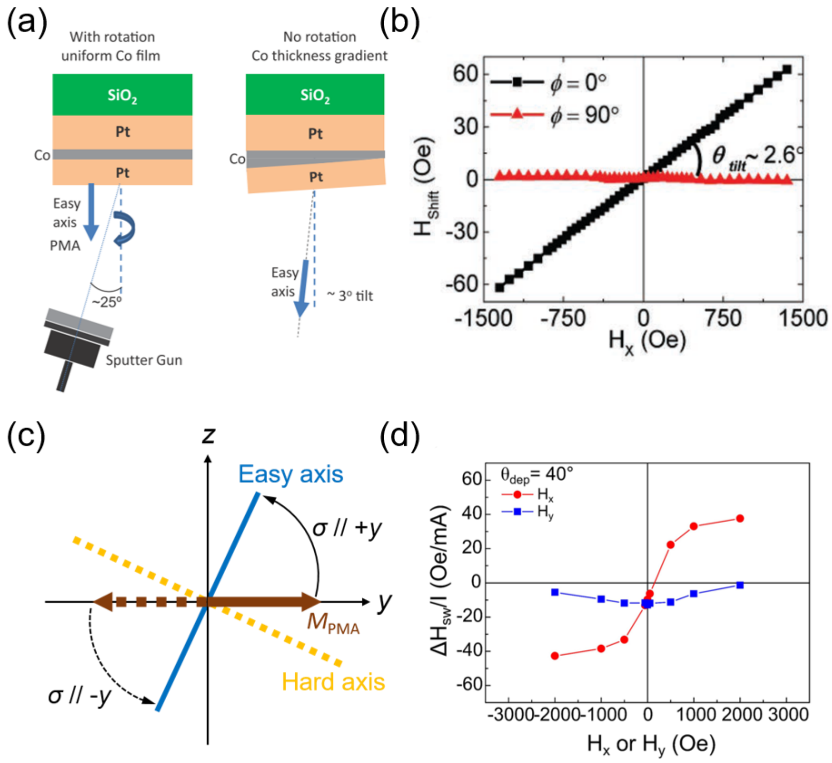

Fig. 3-1 Tilted anisotropy generation and its effect on PMA magnetization switching. (a) The previously proposed mechanism where tilting is generated via a thickness gradient. Adopted from [76]. (b) Hysteresis shift of the PMA magnetization with slight tilting toward azimuthal angle of 0°. Reprinted from [77]. (c) Demonstration of how the tilted easy axis away from the *z* axis accomplishes deterministic switching. (d) The effect of tilted anisotropy is equivalent to a longitudinal (*x*) effective field. Reprinted from [86].

To this end, samples with structures of Ta(0.5)/[Pt(1)/Co(0.8)]$_n$/Pt(2.2)/Co(1.7)/Ta(3) are prepared on thermally oxidized silicon wafers (stacking number n = 1, 2, 3, 4). The Ta layers served to provide adhesion and capping to the structure. As demonstrated in Fig. 3-2(a), the thick Co(1.7) layer possesses IMA, while PMA exists in [Pt/Co]$_n$ multilayers. The symmetry breaking generated by oblique deposition of the Ta layer is aligned toward the y direction, transverse to the current direction (x) following the symmetry analysis to achieve symmetry-breaking [82]. Subsequently, following the established measurement protocol, the IL-DMI strength between [Pt/Co]$_n$ and Co can be quantified.

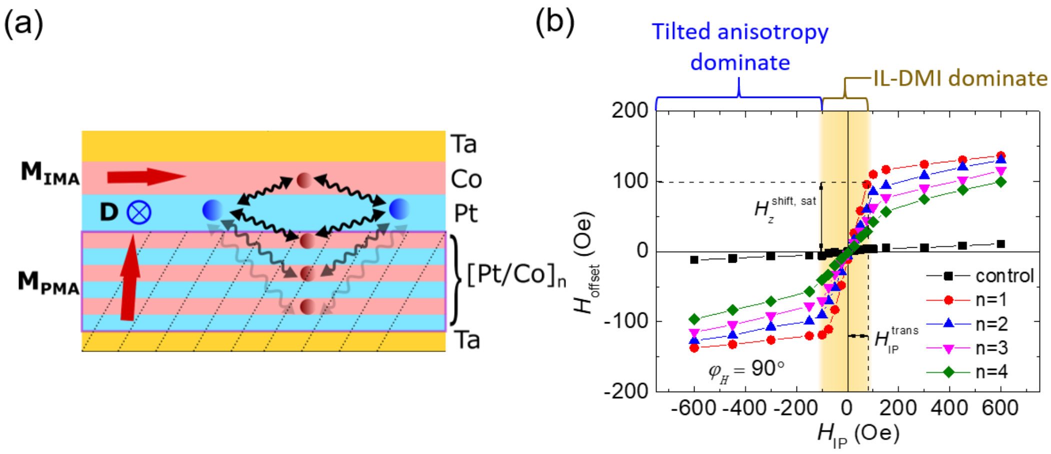

Fig. 3-2 Coexistence of IL-DMI and tilted magnetic anisotropy. (a) Schematic illustration of the broken symmetry due to the obliquely grown Ta buffer and disabled rotation of the Pt layer. The relative orientations of $\boldsymbol{M}_{\mathrm{IMA}}$ (Co with IMA) $\boldsymbol{M}_{\mathrm{PMA}}$ ([Pt/Co]$_n$ with PMA) and $\boldsymbol{D}$ are also shown. (b) The H_z^{shift} under different values of H_{IP}, where $\varphi_{\mathrm{H}} = 90°$, for all samples. H_z^{shift} can be separated into two parts by the clear change in the slope of H_z^{shift} vs. H_{IP}. In the shaded region where $H_{\mathrm{IP}} < H_{\mathrm{IP}}^{\mathrm{trans}}$, IL-DMI dominates while at higher in-plane fields ($H_{\mathrm{IP}} > H_{\mathrm{IP}}^{\mathrm{trans}}$), the contribution from tilting anisotropy is predominant. H_z^{shift} and $H_{\mathrm{IP}}^{\mathrm{trans}}$ for the n = 1 sample are indicated by the arrows. Reprinted from [97].

We focus on the response of H_{offset} under in-plane field H_{IP} scans with direction fixed at $\varphi_H = 90°$ (the direction where the PMA hysteresis z-directional shift H_z^{shift} is maximized). A distinct dichotomy in the relationship between H_z^{shift} and H_{IP} is discerned in Fig. 3-2(b), where two regions with disparate slopes are separated into shaded and unshaded parts. The points of the slope transition $H_{\mathrm{IP}}^{\mathrm{trans}}$ are situated approximately at $H_{\mathrm{IP}} = 75\ \mathrm{Oe}$ for the $n = 1$ sample, and $100\ \mathrm{Oe}$ for $n = 2$, 3, and 4, signifying the saturation of IL-DMI's contribution to H_z^{shift}. This saturation behavior marks the alignment of M_{IMA} toward $\varphi_H = 90°$ (identical to the behavior captured in Fig. 1-13). Beyond $H_{\mathrm{IP}}^{\mathrm{trans}}$, H_z^{shift} continues to exhibit a linear increase with ramping H_{IP}. This additional component in H_z^{shift} is ascribed to the tilted PMA anisotropy induced by the wedged structure, a phenomenon further examined in the next section. Note that the control sample depicted in Fig. 3-2(b) shows minimal H_z^{shift} with no discernable slope change, thereby confirming the absence of both IL-DMI and tilted anisotropy when the symmetry breaking element is absent.

doi:10.6342/NTU202404434

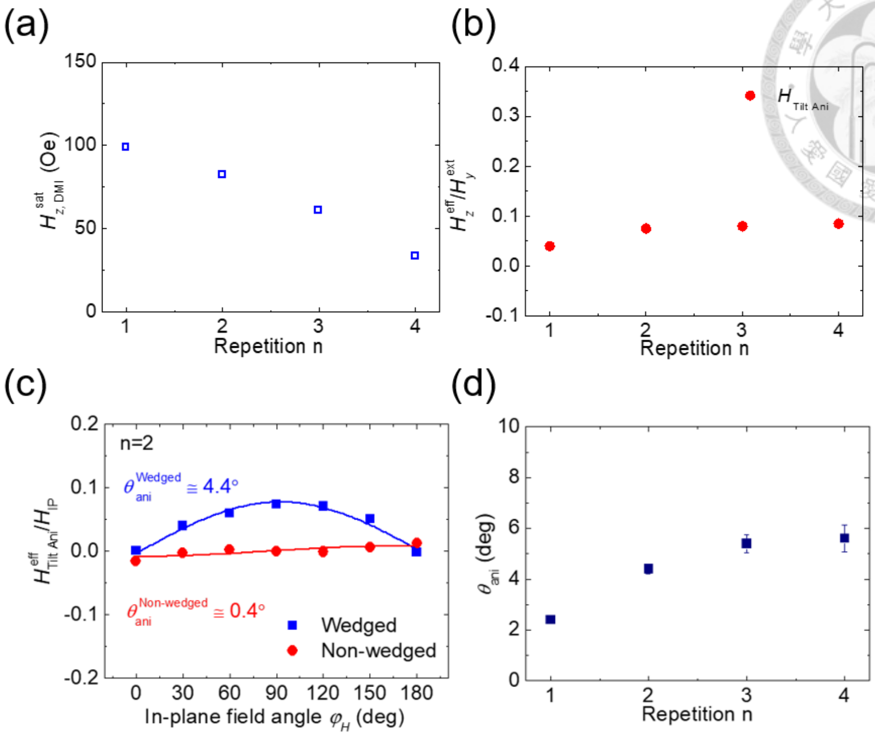

Fig. 3-3 Tilting angle & H_{DMI} vs. the repetition of $[Pt/Co]_n$. Extracted value of (a) IL-DMI effective field ($H^{sat}_{z,\,DMI}$) and (b) ratio between the z directional effective field and the in-plane field ($H^{eff}_z/\ H^{ext}_y$). (c) Estimation of the intensity of tilting, quantified by H^{eff}_{TA}/H_{IP} in the tilting-anisotropy-dominated regime (white region), for the n = 2 device. (d) From the ratio extracted by cosinusoidal fitting as demonstrated in (c), θ_{ani} can be obtained. Figure adapted from [97].

As introduced previously, by treating the measured H^{shift}_z as the superposition of both IL-DMI and contributions from tilted PMA anisotropy, and considering the linear relationship between the tilted anisotropy's contribution and H_{IP} [77], we can deduce the maximum value of IL-DMI's effective field here (termed $H^{sat}_{z,\,DMI}$). This value is obtained by subtracting H^{shift}_z at H^{trans}_{IP} ($H^{shift,\,sat}_z$) by the products of corresponding H^{trans}_{IP} and H^{shift}_z/H_y at the unshaded regions. Compiled in Fig. 3-3(a), $H^{sat}_{z,\,DMI}$ attenuates from 101 Oe to 34 Oe as the stack number n increases from 1 to 4. This is due to the lower part of the $[\mathrm{Pt/Co}]_n$ stack experiences increased exchange length as n increases. Conversely, the ratios of H_z^{shift}/H_y governed by the tilted anisotropy (slopes from the unshaded region in Fig. 3-2(b)) exhibits a less pronounced yet contrasting trend, increasing from 0.04 to 0.085 as n increases from 1 to 4, as depicted in Fig. 3-3(b). Compared to a previous study that attributed its origin to strain-induced magnetic anisotropy, these values of H_z^{shift}/H_y are very comparable [77].

Although the magnitude of tilted magnetic anisotropy is comparatively low in comparison to IL-DMI, its contribution to the shift in hysteresis loops cannot be disregarded. This contribution holds significance when quantifying the energy density of respective effects, and might potentially play a role in current-induced field-free switching mechanisms. To quantify the tilted anisotropy, the ratio of $H_z^{\mathrm{shift}}/H_{\mathrm{IP}}$ in the large field regime was measured under varying static H_{IP} and different φ_H angles. For example, when n = 2, a variation in $H_z^{\mathrm{offset}}/H_{\mathrm{IP}}$ with φ_H is evident compared to the control sample, as summarized in Fig. 3-3(c). These $H_z^{\mathrm{offset}}/H_{\mathrm{IP}}$ vs. φ_H data points are subjected to fitting to extract the easy axis tilted angle θ_{ani} (tilt away from z-axis) according to [76,85]

$$H_z^{\mathrm{offset}}\cos\theta_{\mathrm{ani}}=H_{\mathrm{IP}}\cos(\varphi_{\mathrm{ani}}-\varphi)\sin\theta_{\mathrm{ani}} \tag{3.1}$$

Where θ_{ani} = 4.4° is extracted when n = 2 while a negligible 0.4° is extracted from the control sample (Fig. 3-3(c)). Furthermore, a monotonic increase is observed as n increases, where a maximal of 5.6° is reported when n = 4 (Fig. 3-3(d)). This increasing trend is tentatively ascribed to the template effect facilitated by the wedged Ta buffer (seed) layer [100] which is strengthened when the number of stacks of $[\mathrm{Pt/Co}]_n$ grown without rotation is increased. In addition, the maximum of $H_z^{\mathrm{offset}}/H_{\mathrm{IP}}$ is situated at φ_H = 90°, corresponding to a φ_{ani} close to 90°, in line with the wedge symmetry. Overall, the tilting is sizable, comparable to previous reports (2.6° in [77] and 3.3° in [76]).

In this section, it's revealed that due to the oblique angle deposition process to create wedge structures, IL-DMI and tilted magnetic anisotropy exists simultaneously in our samples. Their contribution to the hysteresis offset can be separated by their different response under varied H_{IP} strength, and they possess opposite trends with increased wedged layer thickness.

3.1.2 Role of Tilted Magnetic Anisotropy and IL-DMI in Current-Induced Field-Free switching

The coexistence of tilted magnetic anisotropy and IL-DMI raises a crucial question regarding the identification of the dominant mechanism driving current-induced field-free switching. Identical to the protocol employed in section 2.3, I_{write} with pulse width of 50 ms are applied along the longitudinal direction of the Hall bar devices. The switching of $\boldsymbol{M}_{\mathrm{PMA}}$ is probed by R_{H} and UMR is employed to detect $\boldsymbol{M}_{\mathrm{IMA}}$'s dynamics. As illustrated in Fig. 3-4(a), current-induced field-free switching is attainable for both $\boldsymbol{M}_{\mathrm{PMA}}$ and $\boldsymbol{M}_{\mathrm{IMA}}$. Moreover, in Fig. 3-4(b), the critical switching currents, I_{c}, exhibit a consistent increasing trend with higher stacking order, and are almost the same for both PMA and IMA magnetizations, regardless of n. This strongly suggests that the moment in both layers are electrically switched simultaneously, still following the IL-DMI coupling scenario. However, as outlined in Fig. 3-4(c), the switching percentage of $\boldsymbol{M}_{\mathrm{PMA}}$ decreases significantly from 70% to 2% as n increased from 1 to 4, whereas that of $\boldsymbol{M}_{\mathrm{IMA}}$ remains

doi:10.6342/NTU202404434

relatively constant at nearly 100% throughout. This nearly constant switching ratio in $\boldsymbol{M}_{\mathrm{IMA}}$ can be attributed to the nature of type-y SOT switching, which is inherently field-free [91]. Conversely, the fraction of domains that are successfully switched in the $[\mathrm{Pt/Co}]_n$ multilayers diminishes as the magnitude of H_{DMI} attenuates with increasing n. This is also in coherence with the observation that $H_{z,\mathrm{DMI}}^{\mathrm{sat}}$ fails to overcome the H_{c} of $\boldsymbol{M}_{\mathrm{PMA}}$ as n increases (Fig. 3-3(a)), and only some domains with inherently weaker H_{c} can be switched. Note that the increased I_{c} required for samples with higher n is attributed to additional current shunting from the greater overall thicknesses. A crucial conclusion therefore can be made where the scenario involving tilted anisotropy in concert with SOT is unlikely to be the mechanism driving the observed field-free switching, since the decrease in switching percentage contradicts the measured increase in tilting intensity, which should've assisted in field-free switching.

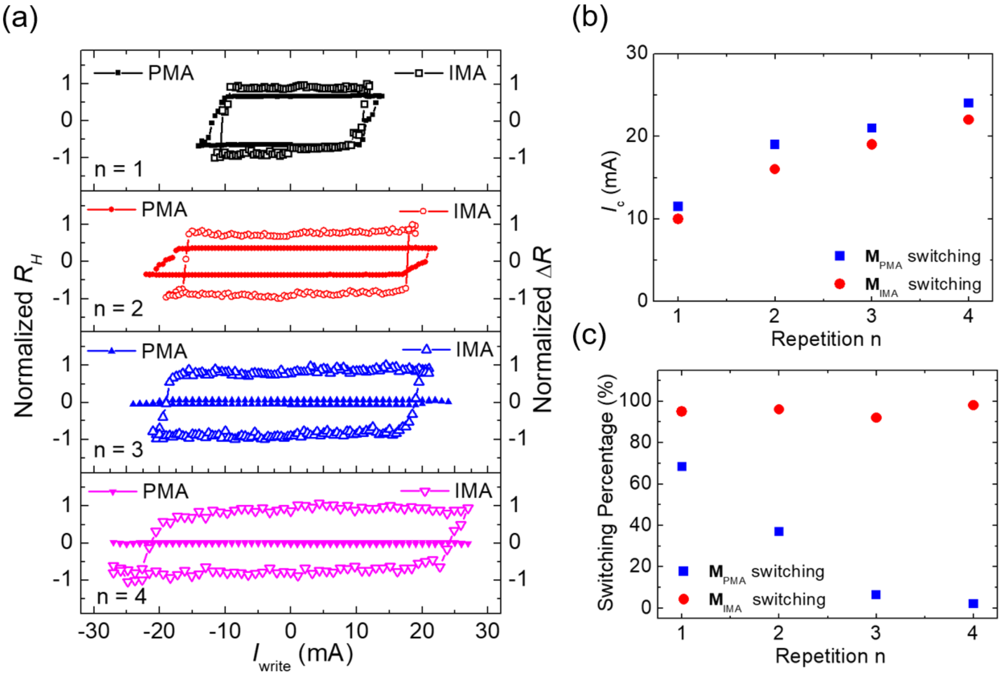

Fig. 3-4 Field-free switching of both $\boldsymbol{M}_{\mathrm{IMA}}$ and $\boldsymbol{M}_{\mathrm{PMA}}$. (a) Magnetization switching loops for Hall bar devices with different n values. R_{H} and ΔR (generated from UMR) are utilized

to probe $\boldsymbol{M}_{\text{IMA}}$ and $\boldsymbol{M}_{\text{PMA}}$ as shown by the solid and open data points, respectively. (b) The stacking number dependence of (b) I_c (critical switching current) and (c) devices' switching percentage are also reported. Figure adapted from [97].

In addition, we performed current-induced hysteresis loop-shift measurement to capture the field-dependent switching behavior. The representative shifted hysteresis loops are shown in Fig. 3-5(a), and the linear DL-SOT effective field of the corresponding H_z^{eff} vs. I_{DC} are depicted in Fig. 3-5(b). Importantly, the H_x and H_y dependence of $H_z^{\text{eff}}/I_{\text{DC}}$, as summarized in Fig. 3-5(c) which exhibit traits akin to a standard HM/FM bilayer structure [66], while the distinct finite $H_z^{\text{eff}}/I_{\text{DC}}$ at low external fields due to a x directional effective field originating from tilted magnetic anisotropy are absent (refer to Fig. 3-1(d)). This further confirms the limited role played by tilted magnetic anisotropy in the field-free switching mechanism.

Lastly, a comprehensive summary of IL-DMI, tilting magnitude, H_c and DL-SOT behaviors as a function of different n are compiled in Table 1.

doi:10.6342/NTU202404434

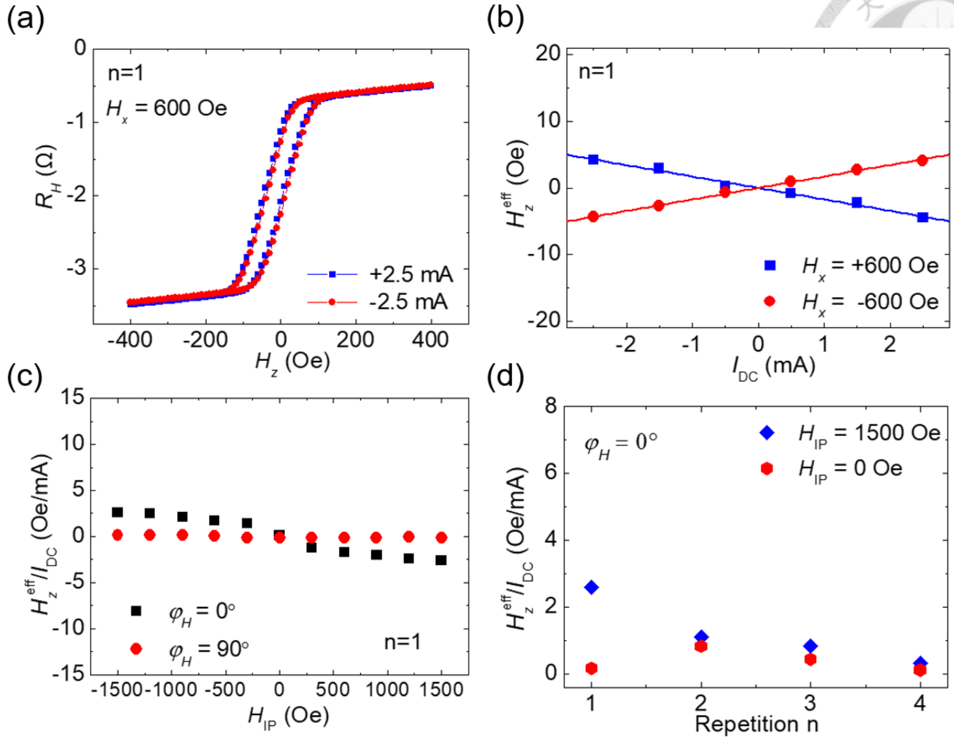

Fig. 3-5 Characterization of DL-SOT effective fields by the hysteresis loop shift method. (a) Representative loop shift behavior from the n = 1 sample under I_{DC} = ± 2.5 mA and H_{x} of 600 Oe. (b) The linear SOT-induced H_z^{eff} under H_{x} = ± 600 Oe. (c) $H_z^{\mathrm{eff}}/I_{\mathrm{DC}}$ as functions of H_{IP} for either x or y directional external fields ($\varphi_H = 0°$ and 90°). Note the distinct lack of asymmetry when compared to Fig. 3-1(d). (d) Compilation of current induced SOT-induced H_z^{eff} versus various stacking repetition (n) under $\varphi_H = 0°$ with H_{IP} = 0 and 1500 Oe. Figure adopted from [97].

n	H_c (Oe)	$H_{z,\,\mathrm{DMI}}^{\mathrm{sat}}$ (Oe)	θ_{ani} (deg)	zero-field switching percentage (%)	zero-field $H_z^{\mathrm{eff}}/J_{\mathrm{DC}}$ ($\mathrm{Oe}/10^{11}\,\mathrm{A}\cdot\mathrm{m}^{-2}$)
1	88	101	2.4 ± 0.13	70	0.7 ± 1.30
2	115	82	4.4 ± 0.20	40	4.3 ± 0.52
3	143	61	5.5 ± 0.36	6	2.6 ± 0.67
4	151	34	5.6 ± 0.50	2	0.8 ± 1.01

Table 1 Summary of the stacking number *n* dependence of both the measured and calculated quantities for $\boldsymbol{M}_{\mathbf{PMA}}$ ($[\mathrm{Pt/Co}]_n$). The uncertainties stemmed from the standard errors in fittings. Table reprinted from [97].

3.2 Lack of Evidence Correlating Field-Induced Magnetic Anisotropy to IL-DMI Generation

We now turn our attention to the origin of IL-DMI. As mentioned in Fig. 2-2, the two primary symmetry-breaking methods for inducing IL-DMI are wedge deposition and the application of an in-situ in-plane external field (H_{ext}) during sample growth. Despite both methods adhering to the symmetry constraint (i.e., symmetry-breaking must occur in-plane), it is intriguing that, according to the literature, both approaches yield desirable outcomes. Specifically, the former method induces structural asymmetry, while the latter method is expected to generate purely magnetic effects. Industrially speaking, applying H_{ext} is more advantageous than the wedge approach by avoiding unwanted thickness gradient that naturally occur in wedged structures. Therefore, it's instrumental to confirm the efficacy of the in-situ H_{ext} approach.

In a Type-T system, Pacheco et al. [64] connected the generation of IL-DMI with a significant uniaxial magnetic anisotropy (UMA) in the CoFeB layer with IMA, where UMA is confirmed by angle-dependent L-MOKE measurement (see Fig. 3-6(a)). In the case of a double-PMA system, however, little connection can be drawn between H_{ext} and UMA, since no IMA magnetization exists within the structure. Still, He et al. [62] demonstrated sizable IL-DMI strength (Fig. 3-6(b)). These are peculiar results indeed, since judging from the latter result, the existence of UMA might not be necessary. In other words, implicit discrepancies seem to exist between reports. In this section, I try to shed light onto the process of applying in-situ H_{ext} to generate IL-DMI in Type-T structures, and discuss its efficacy compared to the wedge deposition method (A thorough investigation into the wedge deposition itself is elaborated in Chapter 4).

doi:10.6342/NTU202404434

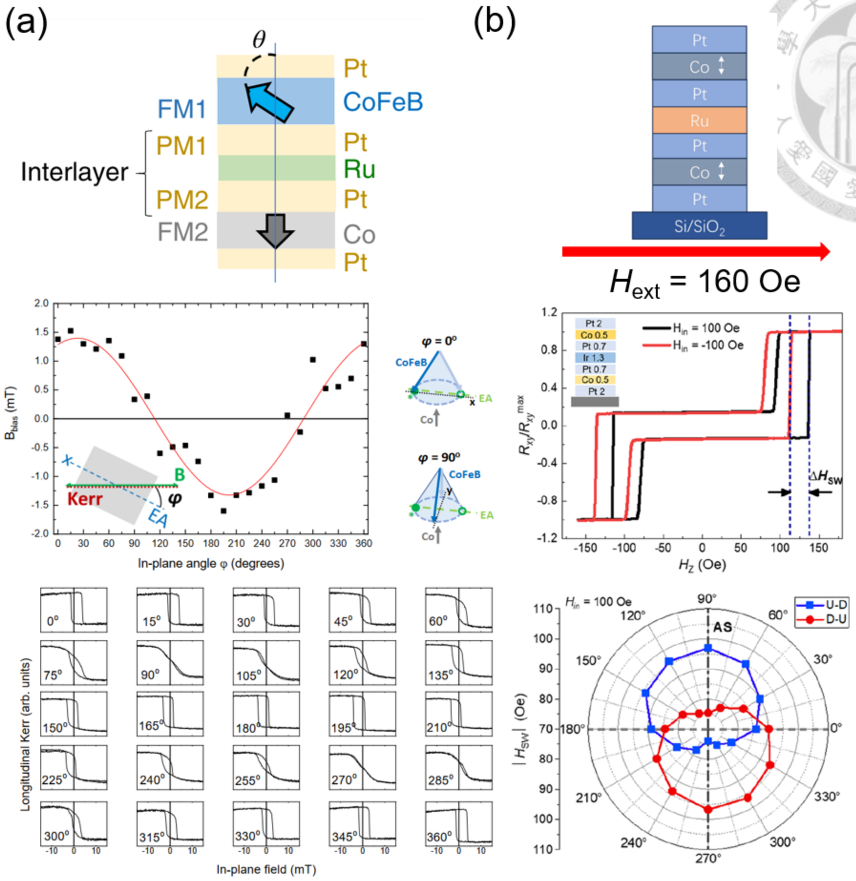

Fig. 3-6 Previous reports utilizing external in-plane field during growth as a source of symmetry breaking, in (a) type-T and (b) double PMA systems. (a) Coexistence of uniaxial magnetic anisotropy (UMA) and IL-DMI induced loop shift in the IMA CoFeB layer, reprinted from [64]. Direct causation relationship between UMA and generation of IL-DMI is claimed by the authors. (b) In double PMA systems, no UMA can be generated due to the natural magnetic anisotropy, though, He. et al. considers H_{ext} an eligible source of symmetry breaking, and sizable IL-DMI is generated. Reprinted from [63] and [62].

To start, we investigate samples prepared by the wedge method. Structures of Ta(0.5)/Pt(t)/Co(0.8)/Pt(t)/CoFeB(1.5)/Ta(2) with an intermediate H_{DMI} magnitude is chosen so that no coherent switching will occur that prohibits L-MOKE detection of the IMA layer's hysteresis behavior. The Ta buffer wedge scheme is employed, where the sputter configuration is plotted in Fig. 3-7(a). The resultant $H_{\mathrm{DMI}}-\varphi_H$ relationship confirms ***D*** to be perpendicular to the Ta atom flow (Fig. 3-7(b)) as expected. When we look at the M_{IMA}'s response as shown in Fig. 3-7(c), not only are the hysteresis loops shifted according to the ***D*** direction, easy (hard) axis behavior is observed along the x (y) axis, where the H_c along easy axis is about 9 Oe, and the in-plane anisotropy field H_{an} is roughly 30 Oe. Using the rotary L-MOKE, the ratio between the remnant magnetization and the saturation magnetization (M_R/M_S) is measured along different in-plane directions, and compiled into the polar plot as shown in Fig. 3-7(d). The clear dumbbell-like shape evidenced the existence of UMA, and the easy axis aligns toward Tantalum's atom flow direction.

This is a peculiar result in the sense that when compared to the work done by Pacheco et al., wedge deposition and an in-situ H_{ext} both induces UMA in M_{IMA}. One might be inclined to consider this convincing evidence relating UMA with IL-DMI, however, caution must be exercised because outside of the topic of IL-DMI, both techniques are well known to generate UMA [101] , i.e. it's possible that at least in the case for wedge deposition, UMA and IL-DMI share their origin in the wedge method, but might not have any causation relationship between themselves. Therefore, it's prudent to perform additional analysis by preparing samples with in-situ H_{ext}.

doi:10.6342/NTU202404434

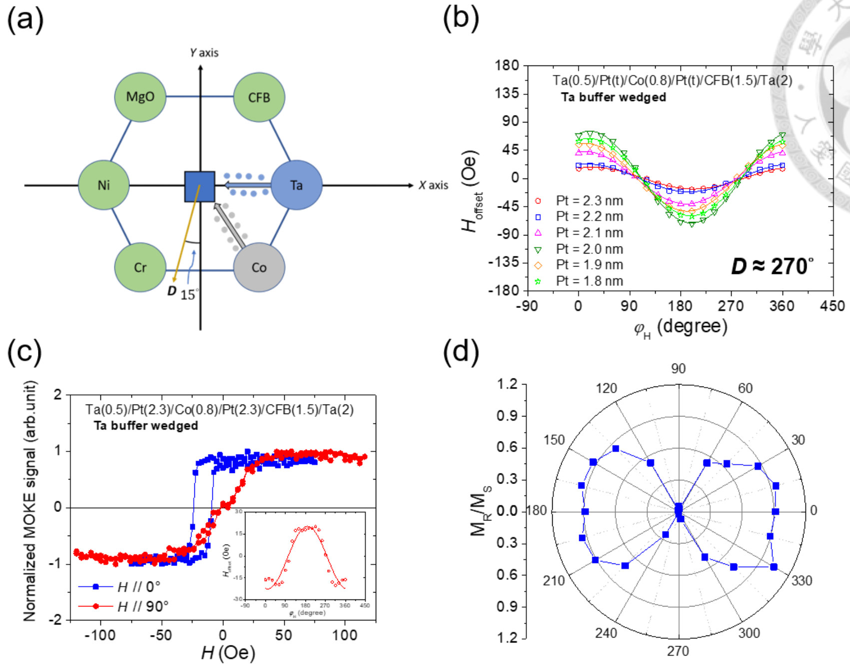

Fig. 3-7 Relationship between the relative orientation of the oblique angle deposition process and the resultant IL-DMI in M_{PMA} and M_{IMA}, and the UMA captured in M_{IMA}. (a) schematics of the relative orientation between the sputter targets and the sample (located at the center). (b) H_{DMI} captured by the previously established angle-dependent loop shift protocol, for various Pt spacer thickness. (c) focusing on the M_{IMA} response in the sample with Pt thickness of 2.3 nm where the clear easy (hard) axis behavior is observed around x (y) axis, respectively. The inset shows the angle-dependent IL-DMI effective field experienced by M_{IMA}. (d) A clear UMA exists in M_{IMA}, as demonstrated by the $\mathrm{M_R/M_S}$ ratio forming a dumbbell-like graph.

Subsequently, a set of NdFeB magnets are attached to the sample holder and provides H_{ext} along the x direction of the samples. The H_{ext}'s magnitude under this setup is roughly 500 Oe, higher than the 180 Oe employed by He et al. [62] and Gao et al. [63]. The real-life snapshot and visualization of this setup is provided in Fig. 3-8(a). The corresponding magnetic response of M_{IMA} is demonstrated in Fig. 3-8(b), where a clear easy axis is aligned parallel to H_{ext}, as evident in the square (oblique) hysteresis loops when the $H_{\mathrm{in\text{-}plane}}$ is applied parallel (perpendicular) to x axis. The in-plane anisotropy field H_{an} is about 24 Oe. Clearly, both wedge deposition and in-situ H_{ext} have successfully induced UMA. However, the angle-dependent loop shift measurement reveals minimal IL-DMI effective field, as reported in Fig. 3-8(c). For the Pt spacer thickness between 2.4 nm and 1.8 nm, the H_{DMI} magnitudes are universally less than 10 Oe in the type-T series. Identical results play out in the double-PMA set of samples, as shown in Fig. 3-8(d). Notably, their angle dependences appear random, in contradiction with the symmetry breaking constraints embodied in the 3rd Moriya rule. On the other hand, the 3rd Moriya rule is always followed in the wedge deposition scenario with no exceptions. We suspect that the random but nonzero H_{offset} reported in Fig. 3-8(c) and (d) are due to the combination effects of slight instrumental errors from the vector magnet, and possibly a low but unavoidable contribution from an “instantaneous wedge” due to the initial incident atoms (occurs when the sputtering process starts).

doi:10.6342/NTU202404434

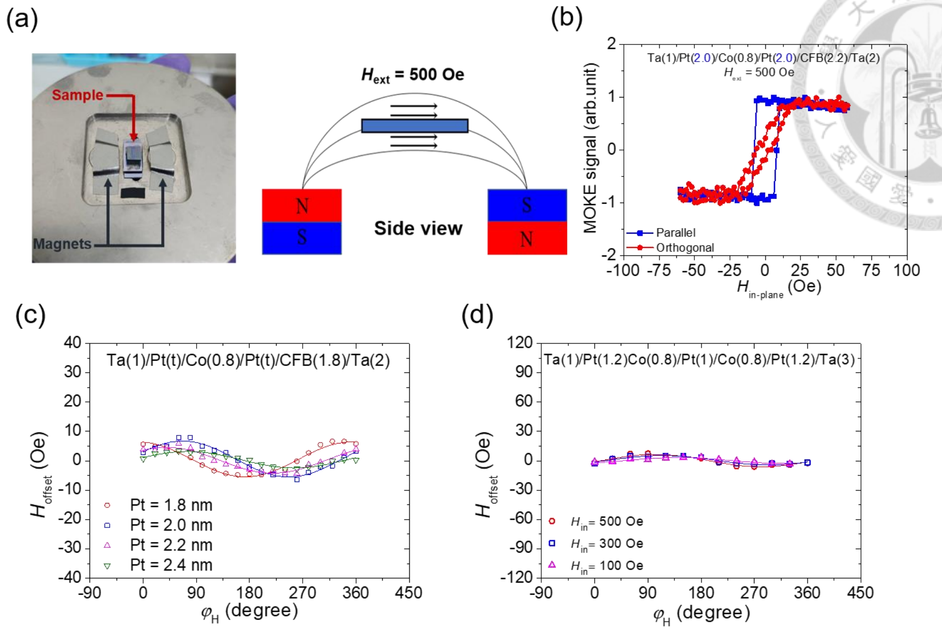

Fig. 3-8 Setup of the in-situ H_{ext} during growth, resultant L-MOKE analysis and the absence of sizable IL-DMI. (a) Left: snapshot of the valley-shaped folder to contain a pair of NdFeB permanent magnets. Right: Side view of the substrate within the magnetic field lines generated by the magnets. H_{ext}'s direction is parallel to the x axis of the sample, its strength of ≈ 500 Oe is measured by a gaussmeter prior to sample placement (at the midpoint between magnets). (b) L-MOKE analysis revealed easy axis along the H_{ext} direction, while the hard axis is correspondingly orthogonal to H_{ext}. (c) H_{offset} plotted as a function of φ_H for different Pt spacer thickness, in Type-T structures. Note the universally low H_{offset} and the random φ_H dependence. (d) H_{offset} response from a double-PMA system. Similar to the case in (c), diminishingly low H_{offset} is observed.

Explanations are clearly required since these experimental results contradict the previous reports compiled in Fig. 3-6. I'd first like to note that investigations into IL-DMI, especially focusing on its origin, are extremely rare, thus I attempt to provide several possibilities in the following. The first possibility is that in the cases of ref. [62-64], the

H_{ext} utilized within these works somehow generates a structural symmetry breaking alongside the originally highlighted UMA. This effect should be similar to wedge deposition due to a currently unknown mechanism. The second possibility is that the UMA from either in-situ H_{ext} or post growth annealing could be effective, but is much weaker in my prepared samples compared to prior results. This is however rather unlikely since judging from the UMA profile as seen in Fig. 3-8(b), the H_{an} of 24 Oe is very comparable to the case of wedge deposition ($H_{\text{an}} \approx 30$ Oe) where the IL-DMI is profound (Fig. 3-7). The final possibility is that the H_{ext} is inconsequential for IL-DMI generation, and the reported H_{DMI} values are the results of the "instantaneous wedge" effect that may naturally occur at the beginning of the sputtering process. This possibility is also supported by the random $\boldsymbol{D}$ vector directions implicitly indicated in ref. [63], and the fact that UMA simply cannot exist in the double-PMA system.

It must be admitted that the efficacy of applying an external H_{ext} during growth (or post growth field annealing) is still shrouded in some uncertainties. However, by cross comparing existing literature with my current experimental results, I tentatively propose that it's likely the UMA is a byproduct of the sample growth process, but is not the origin of IL-DMI. Nevertheless, I look forward to follow-up researches, be it calculations or experimental works that can provide deeper insights on the effects (or the lack) of the in-situ H_{ext} at IL-DMI generation. Finally, note that it's easier to relate the physical picture of wedge deposition to IL-DMI generation, as elaborated in the next chapter.

doi:10.6342/NTU202404434

Chapter 4 Azimuthal Engineering and Modelling of Interlayer Chiral Exchange

In the previous sections, experimental verifications have expanded our understanding of IL-DMI. However, little attention has been given to controlling the strength of IL-DMI, and a comprehensive model bridging the gap between symmetry analysis and the physical origin of IL-DMI remains incomplete.

Within this context, we unveil advancements in controlling the strength of IL-DMI and elucidate how the detailed conditions of the wedge deposition serve as crucial tuning parameters for IL-DMI. Building on these important observations, we developed a comprehensive viewpoint on the physical origin of IL-DMI through our devised toy model based on the Fert-Lévy three-site scenario. This model allows us to better explain the effect of wedge deposition, and furthermore, we address the unfavorable device-to-device characteristic deviations often associated with the wedge deposition process by implementing specific azimuthal engineering designs, desirable for real-life implementation.

Additionally, we present solid experimental evidence supporting the oscillatory nature of IL-DMI and determined its characteristic length, thereby confirming IL-DMI's origin as an additional term of the RKKY interaction stemming from the spin-orbit scattering of conduction electrons, as predicted by Smith, Fert and Lévy [17,46]. Content in this chapter is primarily rewritten from my published work “Tailoring Interlayer Chiral Exchange by Azimuthal Symmetry Engineering” [102], with additional refined content.

doi:10.6342/NTU202404434

4.1 Tunable IL-DMI Strength by Oblique Angle Deposition Control

Thus far, several studies have employed oblique angle deposition (OAD) to induce IL-DMI. Apart from our previous works [53,97], all these seminal reports have opted to employ wedge deposition on the “spacer layer” which separates the two magnetizations coupled by IL-DMI. For example, Han et al. obliquely deposited the Ir layer in the stack of Pt/Co/Pt/Ir/Pt/Co/Pt multilayers [58], while Wang et al. employed wedged Pt/Ru/Pt spacer layers in a Pt/CoB/Pt/Ru/Pt/CoB/Pt structure [60]. While this appears to adhere to the in-plane symmetry breaking picture showcased in Fig. 2-1, it implicitly confines the element that participate in the symmetry breaking process to a single wedged layer. On the other hand, it’s evident that IL-DMI can be induced by obliquely depositing the buffer layer, as shown in the results in chapter 2 and 3, where the wedged layers were chosen to be CoFeB under layer and the seeding Ta buffer layer, respectively. This is an important point of interest, therefore, through the utilization of OAD to generate multiple wedged layers, a detailed profiling of IL-DMI can be made in both orthogonally magnetized (type-T) and perpendicularly-magnetized synthetic antiferromagnet (SAF) systems.

Two series of magnetic multilayers, denoted as S1 and S2, are fabricated on thermally-oxidized Si/SiO2 substrates using high-vacuum magnetron sputtering. The deposition conditions employed are identical to those described in previous procedures outlined in Chapters 2 and 3. The layer composition for each series are as follows:

1. S1: Ta(0.5)/Pt(2)/Co(0.75)/Pt(2)/CoFeB(1.35)/Ta(2)
2. S2: Ta(0.5)/[Pt(1)/Co(0.4)]$_3$/Ru(0.5)/[Co(0.4)/Pt(1)]$_2$/Ta(2)

Where Pt/Co based structures are again chosen for robust PMA characteristics and high

SOC at the interface to satisfy the requirements for DMI generation (though, it's worth noting that a recent publication successfully incorporated a Ag spacer with strong Rashba coupling [103]). In S1, the type-T magnetic configuration is adopted, with Co demonstrating PMA attributed to the strong SOC at the Pt/Co and Co/Pt interfaces, while the relatively thick CoFeB layer possesses IMA. In S2, an optimized Ru thickness of 0.5 nm antiferromagnetically couples the [Pt(1)/Co(0.4)]$_3$ and [Co(0.4)/Pt(1)]$_2$ layers therefore forming a SAF structure in S2. In both series, individual Pt layers are selectively wedge deposited to induce in-plane symmetry breaking. Based on the insights gained from S1 and S2, several other stack designs are formulated afterwards.

4.1.1 Type-T structures

We start our investigation by exploring the contribution of different wedge layers to the overall strength of IL-DMI in S1. Specifically, the wedge growth is achieved through Oblique angle deposition (OAD), with the Pt atom flow inclined at an incident angle of 20° relative to the substrate normal and an azimuthal angle of 0° (parallel to the x-axis as indicated in Fig. 4-1(a)). Subsequently, our wedge scenarios are designed as follows:

6. Pt buffer layer (designated Pt$_1$) and spacer layer (designated Pt$_2$) both grown with identical OAD conditions.
7. Pt$_1$ grown with OAD.
8. Pt$_2$ grown with OAD.
9. Pt$_1$ deposited with standard OAD, while during the sputtering of Pt$_2$, the sample holder is rotated by 180° relative to Pt$_1$'s wedge direction (azimuthal angle being 180°), we labeled this the "counter-wedge" scenario.

A graphical representation of the counter-wedged structure is provided in Fig. 4-1(a), with the inset in Fig. 4-1(d) outlining the critical layers for all scenarios.

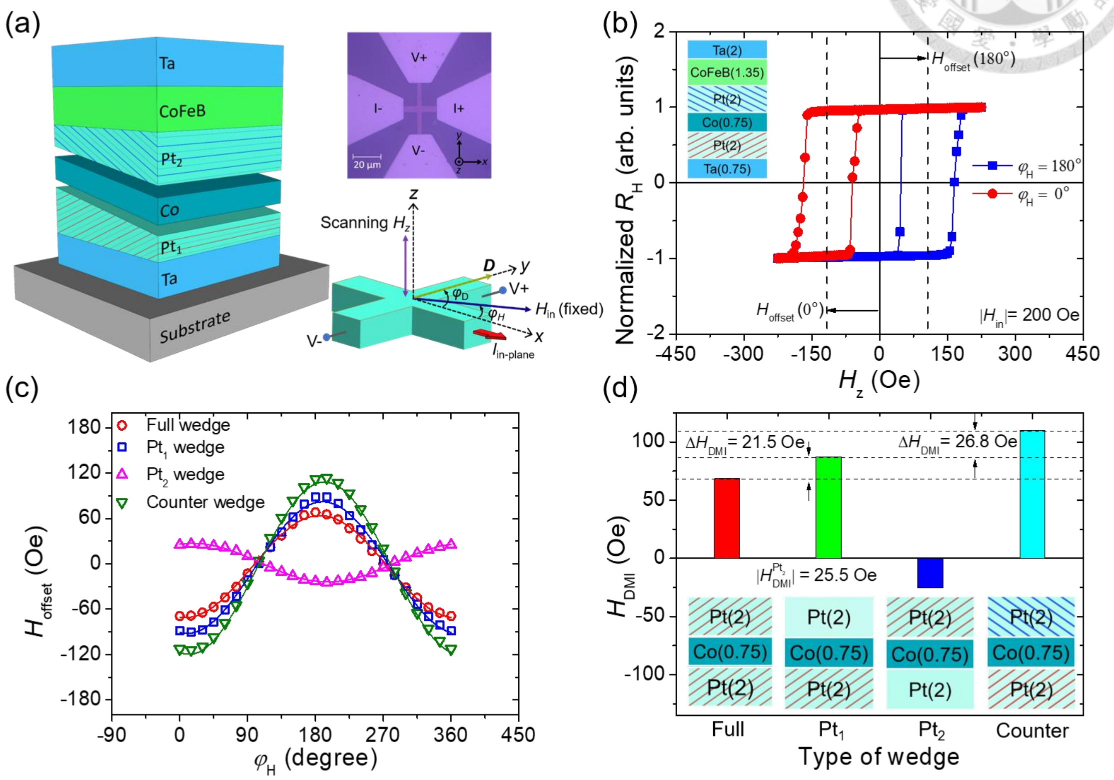

Fig. 4-1 Characterization of the effective fields induced by IL-DMI in type-T samples (Series S1) with different wedge conditions depicted. (a) Left: Illustration of the representative counter-wedge grown condition, where Pt$_1$ and Pt$_2$ denotes the buffer and spacer Pt layers, respectively. The counter-wedge is graphically highlighted by red/blue stripes (for visual clarity), emphasizing its origin from the antiparallel atom flux directions. The atom flow points toward the plane normal of the stripes. Upper right: Optical microscope image of a representative Hall bar device. Lower right: Setup for angle-dependent loop-shift measurements. (b) Representative R_H vs. H_z loops of a counter-wedge sample measured with φ_H = 0° and φ_H = 180°. (c) H_{offset} plotted as a function of φ_H for various types of OAD conditions. Solid lines depict sine fits to the data, facilitating extraction of H_{DMI} as previously discussed in Chapter 2. (d) H_{DMI} values

for different OAD conditions compiled from (c). The inset illustrates their respective 2D representations of critical layers (Full, Pt_1, Pt_2, and counter wedge, respectively). Note that to form a basis of comparison, H_{DMI} is designated negative for Pt_2 wedge. Reprinted from [102].

Following an identical energy analysis strategy as elaborated in Chapter 2, angle dependent loop-shift measurement is employed to characterize the strength of IL-DMI, where the effective fields felt by the two magnetic layers are described by eqn. (2.3) and (2.4). Here, $\boldsymbol{H}_{in}$ (with $|H_{in}|$ = 200 Oe) is applied to preset the magnetization of $\boldsymbol{M}_{IMA}$ while the H_z is swept to record the hysteresis behavior of the PMA (Co) layer through R_H measurement on the Hall bar devices as schematically illustrated in the lower right panel of Fig. 4-1(a). Sizable H_{offset} can clearly be observed from the representative R_H-H_z loop from the counter wedged sample as shown in Fig. 4-1(b). By systematically rotating φ_H from 0° to 360°, the variations of H_{offset} with φ_H are shown in Fig. 4-1(c). The existence of sizable IL-DMI is clearly showcased by the iconic antisymmetric behavior of H_{offset}, where the magnitude of H_{DMI} can be extracted by $H_{offset} = H_{DMI}\sin(\varphi_H - \varphi_D)$.

For the wedged spacer Pt_2, sine fit indicates $\varphi_D \approx 286°$ and yields an H_{DMI} of 25.5 Oe. Conversely, when the Pt_1 buffer layer is wedged, $\varphi_D \approx 99°$ while simultaneously exhibiting a sizably higher H_{DMI} of 87.1 Oe (the slight deviation of φ_D from either 90° or 270° is due to unavoidable misalignments in the sputter chamber or when devices are transported onto the vector magnet). It's clear that whilst these two scenarios both follow the third Moriya rule in which $\boldsymbol{D}$ is perpendicular to the symmetry breaking factor, $\boldsymbol{D}$ is surprisingly rotated approximately 180° when comparing Pt_1-wedged to its Pt_2-wedged counterpart.

Based on the findings in Pt_1 and Pt_2-wedged samples, it's evident that employing an

doi:10.6342/NTU202404434

identical OAD condition on different wedged layers results in the generation of opposite symmetry breaking polarities, suggesting the potential for azimuthal-symmetry engineering. Subsequently, in the full wedge sample, where both Pt_1 and Pt_2 are prepared by OAD with an azimuthal angle of 0°, H_{DMI} is weakened to 68.6 Oe while maintaining an identical φ_{D} as the Pt_1 wedge scenario. Conversely, in the counter-wedge sample (Pt_1-0° and Pt_2-180°), an enhancement of H_{DMI} to 113.8 Oe is observed. These results are summarized in Fig. 4-1(d). It's worth noting that reminiscent to that the full wedge structure can be conceptualized as a combination of Pt_1 and Pt_2 wedge, full wedge structure's corresponding H_{DMI} value indeed accurately matches with the mutual cancellation from Pt_1 and Pt_2 due to their antiparallel φ_{D} (a clear linear dependence). On the other hand, in the counter-wedge case, by reverting Pt_2 wedge's corresponding φ_{D} via reversed OAD, subtraction of H_{DMI} transforms into addition. Overall, these linear values of H_{DMI} originating from corresponding combinatory wedge conditions are highlighted in Fig. 4-1(d).

4.1.2 IL-DMI behavior in a double-PMA system

Before continuing to investigate SAF structures, it's essential to first introduce IL-DMI's manifestation in structures where both magnetizations possessing PMA. Starting from eqn. (2.2), since both magnetizations aligns in the z direction, we alternatively label $\boldsymbol{M}_{\mathrm{T}}$ and $\boldsymbol{M}_{\mathrm{B}}$ as the top and bottom magnetizations, respectively. Let's first focus on $\boldsymbol{M}_{\mathrm{T}}$. The IL-DMI effective field $\boldsymbol{M}_{\mathrm{T}}$ experiences is similar to eqn. (2.3) and takes the form of $\boldsymbol{H}_{\mathrm{DMI}} = \boldsymbol{M}_{\mathrm{B}} \times \boldsymbol{D}$. If no external $\boldsymbol{H}_{\mathrm{in}}$ is applied, then $\boldsymbol{H}_{\mathrm{DMI}}$ has a null out-of plane component and cannot be captured via angle dependent loop-shift. However, when $\boldsymbol{H}_{\mathrm{in}}$ is applied, $\boldsymbol{M}_{\mathrm{B}}$ deviates a small angle from z direction, and can be approximated by $\boldsymbol{M}_{\mathrm{B}} \approx$

doi:10.6342/NTU202404434

$\pm \boldsymbol{j} + \boldsymbol{H}_{\text{in}}/H_{\text{K}}$ [72,104] where $\boldsymbol{j}$ is the unit vector in the z-direction and H_{K} the effective PMA anisotropy field (this first order approximation holds when $|\boldsymbol{H}_{\text{in}}| \ll H_{\text{K}}$). The overall IL-DMI effective field is therefore represented as follows:

$$\boldsymbol{H}_{\text{DMI}} = \boldsymbol{j} \times \boldsymbol{D} + \boldsymbol{H}_{\text{in}} \times \boldsymbol{D}/H_{\text{K}} \tag{4.1}$$

An identical argument holds for $\boldsymbol{M}_{\text{B}}$. Note that due to the inability to capture the in-plane component $\boldsymbol{j} \times \boldsymbol{D}$ in eqn. (4.1), it's much more practical to omit the first term in eqn. (4.1) and focus on capturing the out-of plane term $\boldsymbol{H}_{\text{in}} \times \boldsymbol{D}/H_{\text{K}}$ as a basis of comparison, which we designated the effective H_{DMI} in subsequent investigations into double PMA systems. A graphical depiction of the relationship between these vectors are illustrated in Fig. 4-2(a). As a result, we separately prepared a Ta(0.5)/Pt(2)/Co(0.6)/Pt(0.7)/Co(0.6)/Pt(2) sample where the buffer Pt layer is deposited with OAD (critical layers illustrated in Fig. 4-2(a)). We then characterized this multilayer structure's PMA anisotropy field (H_{k}, as shown in Fig. 4-2(b)) via detecting the magnetization's R_{H} response under x-directional field scan, and obtained an overall $H_{\text{k}} \approx$ 3300 Oe via quadratic fitting (although, due to the entanglement between the hysteresis behavior of $\boldsymbol{M}_{\text{T}}$ and $\boldsymbol{M}_{\text{B}}$, the multilayer's overall response is used to approximate individual layer's PMA anisotropy field, which should be close enough as He et al. verified with micromagnetic simulation [62]). The angle scan results are portrayed in Fig. 4-2(c), where the $\boldsymbol{D}$ vector is clearly parallel to the x axis (consistent with the atom flux's azimuthal angle of 90°, and the H_{offset} is dependent on the magnitude of H_{in}). The linear trend of $\boldsymbol{H}_{\text{DMI}}$'s z component as a function of H_{in} is compiled in Fig. 4-2(d), in good accordance with eqn. (4.1), and demonstrates the difference in IL-DMI's response when compared to the saturating H_{offset} in type-T structures as previously showcased in Fig.

doi:10.6342/NTU202404434

2-4(b). Modifying eqn. (2.5) by applying eqn. (4.1), the IL-DMI energy density in this device can be estimated to be $E_{\mathrm{DMI}} = \mu_0 M_s t_{\mathrm{FM}} H_{\mathrm{offset}}(H_{\mathrm{in}}/H_{\mathrm{k}}) \approx 46.4\ \mu\mathrm{J/m}^2$.

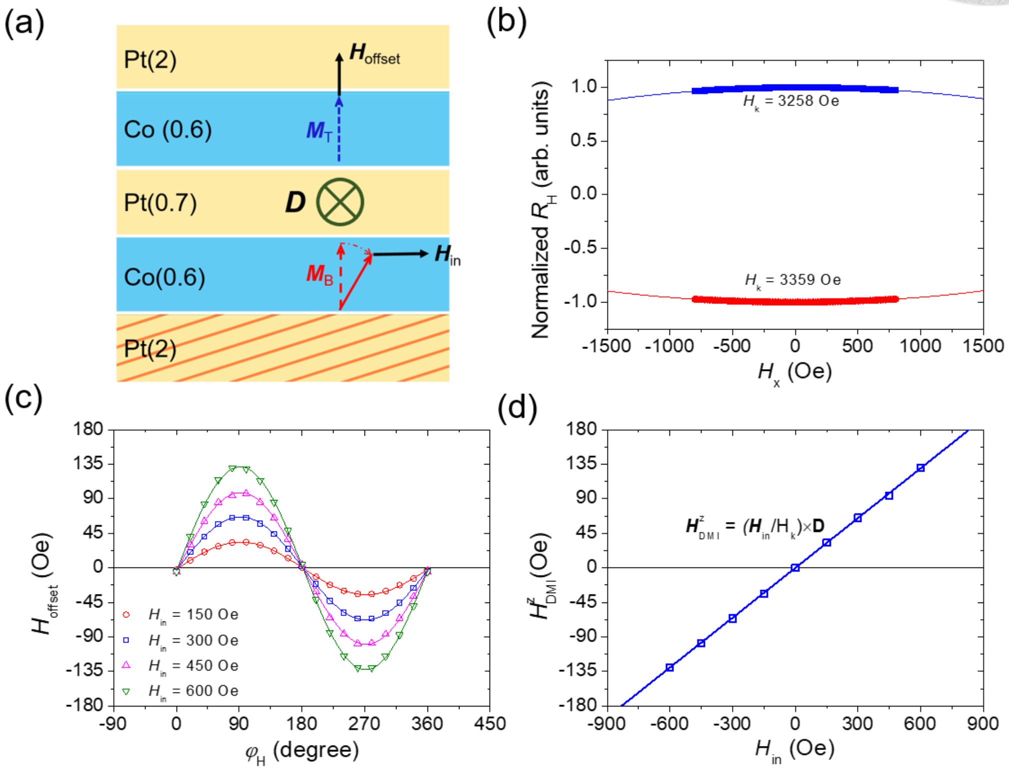

Fig. 4-2 IL-DMI in a double PMA magnetization system. (a) Representative diagram of the H_{offset} in $\boldsymbol{M}_{\mathrm{T}}$ generated by tilting of $\boldsymbol{M}_{\mathrm{B}}$ via the application of H_{in}. Buffer Pt layer deposited under OAD to generate in-plane symmetry breaking. (b) Measurement of H_{K} by capturing the response of R_{H} under x directional field scan, from which H_{K} is extracted via quadratic fitting. (c) H_{offset} as a function of φ_{H} under different H_{in} magnitudes. (d) Linear response of $\boldsymbol{H}_{\mathrm{DMI}}$'s z component with regard to the in-plane field strength.

4.1.3 SAF System

Now we proceed to investigate how manipulating the OAD conditions can influence

IL-DMI in SAF structures of the S2 samples. Fig. 4-3(a) depicts the SAF structure with an enlarged illustration providing an example of the wedge conditions of various Pt layers (in this instance, counter-wedge). The full R_H versus H_z loop is shown in the inset of Fig. 4-3(b), which exhibits a square hysteresis near its origin. It's evident that the bottom $[Pt/Co]_3$ (referred to as $\boldsymbol{M}_B$) and the top $[Co/Pt]_2$ (referred to as $\boldsymbol{M}_T$) are antiferromagnetically coupled via the Ru(0.5) spacer layer, and are aligned parallel under high H_z. In S2, considering the z-oriented $\boldsymbol{M}_T$ and $\boldsymbol{M}_B$, the application of H_{in} results in an in-plane tilt of the PMA magnetizations (as discussed in section 4.1.2), generating nonzero H_{offset} via $\boldsymbol{H}_{DMI(B)} = \boldsymbol{D} \times \boldsymbol{M}_T$ ($\boldsymbol{H}_{DMI(T)} = -\boldsymbol{D} \times \boldsymbol{M}_B$) with regard to $\boldsymbol{M}_B$ ($\boldsymbol{M}_T$) [62,105]. Fig. 4-3(b) illustrates how a constant H_{in} of 200 Oe disrupts the symmetry of the magnetic hysteresis, with clearly observed antisymmetric H_{offset} providing a robust metric for comparing the strength and direction of IL-DMI.

The three Pt layers within $\boldsymbol{M}_B$, denoted as Pt_1, Pt_2, and Pt_3 (as shown in Fig. 4-3(a)) are subjected to individual analysis to discern their respective impacts on the strength and direction of IL-DMI. Deposited under identical OAD conditions (atom flow azimuthal angle = 0°), angle dependent loop-shift results for Pt_1, Pt_2, and Pt_3-wedged samples are presented in Fig. 4-3(c). Their angular dependencies share the same symmetric/asymmetric axis observed in S1, with the respective H_{DMI} and φ_D extracted by sine fit. Specifically, when Pt_1 is grown via OAD, $\varphi_D \approx 271°$ with $H_{DMI} = 77.9$ Oe. In the case for wedged Pt_2 (Pt_3), an antiparallel $\varphi_D \approx 91°$ is observed, with H_{DMI} of 71.0 Oe (38.9 Oe). Importantly, by combining OAD in Pt_2 and Pt_3 alongside a reversed OAD direction in Pt_1 (referred to as counter-wedge), an enhanced H_{DMI} of 104.0 Oe is observed. Although this value does not precisely coincide with the summation of all H_{DMI} contributions from individual layers, the profound qualitative enhancement compared to the reduction (to 60 Oe) under the destructive full-wedge scenario shows consistency between S1 and S2

doi:10.6342/NTU202404434

samples, reaffirming the feasibility of tuning IL-DMI strength and direction by azimuthal engineering, as summarized in Fig. 4-3(d).

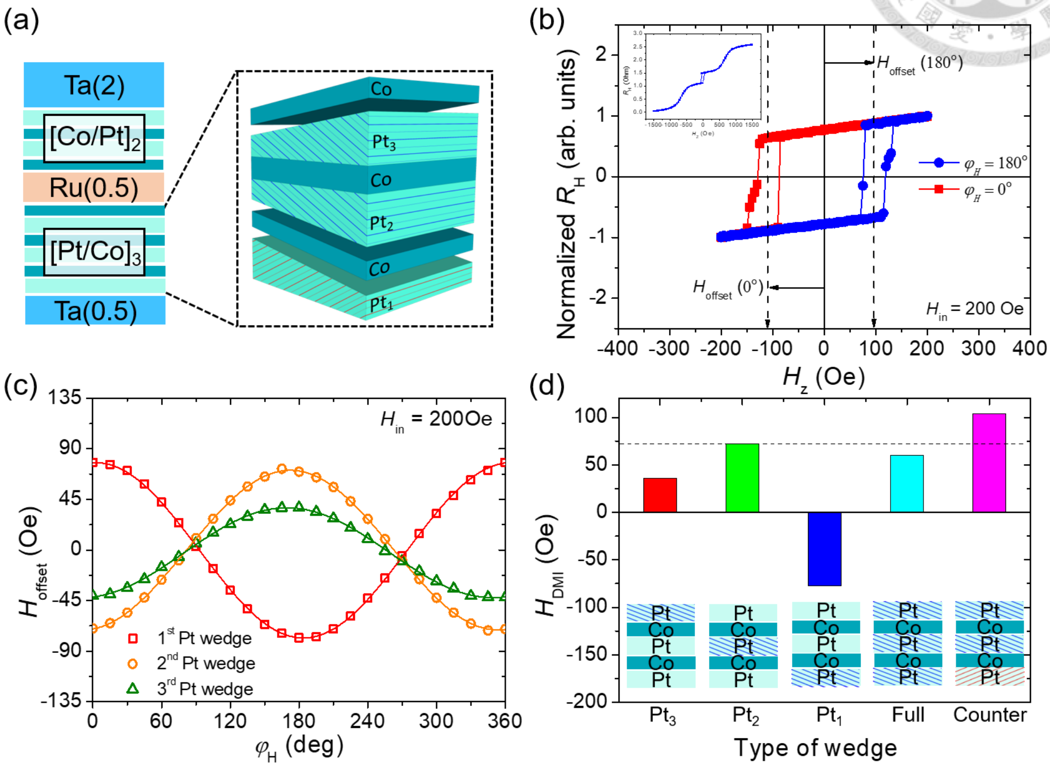

Fig. 4-3 IL-DMI characterization in SAF structures (S2), with various OAD conditions (a) SAF stack's structural overview, the enlarged image highlights the detailed wedge conditions in the bottom $[Pt/Co]_3$ and showcases the "counter-wedge" configuration. (b) asymmetric hysteresis observed in the central loop under $|H_{in}|$ = 200 Oe and φ_H of 0° and 180°. (c) H_{offset} captured by angle scan for Pt_1, Pt_2 and Pt_3-wedged samples. (d) Compilation of measurements for samples with different wedge combinations. Similar to the case in type-T structures, the magnitude of H_{DMI} in Pt_1-wedged sample is designated as negative. The inset provides details on the wedge conditions employed. Figure adopted from [102].

4.2 IL-DMI Toy model developed from the Fert-Lévy three site triangle

Judging from the results in both type-T and SAF samples, a clear linear combinatory contribution from individual wedge deposited layers is observed. Moreover, when we compare their respective H_{DMI} magnitudes, S1 and S2 samples unequivocally point out that the earlier a wedged layer is deposited onto the substrate, the greater influence it exerts on the overall strength of IL-DMI. These results are indeed beneficial for practical implementations, but how can we relate these results to a comprehensive physical picture?

From a microstructural perspective, OAD is frequently responsible for the formation of slanted nanocolumnar structures, primarily driven by the shadow effect [106,107]. For example, Garcia et. al. [108] demonstrated that zig-zag like structures can form by periodically changing the deposition orientation in TiO_2 thin films prepared by sputtering (Fig. 4-4(a)). Moreover, Klemmer and Pelhos [100] as well as Li et al. [101] has proved the existence of slanted nanoscale structures originating from OAD, influencing magnetic properties. Fig. 4-4(b) graphically demonstrates how the atomic self-shadow effect creates a shadowed region due to the initial sputtered atoms serving as a template and blocking the follow-up incident atoms. The resultant slanted nanostructures roughly points toward the atom flux direction (the deposition angle $\alpha \neq \beta$ the resultant structure angle [106], but a positive correlation holds). In spintronics, previous experimental studies have also associated microstructures or tilted textures induced field-free SOT switching to OAD, via analyses such as scanning electron microscopy (SEM) [109] and X-ray diffraction pole figure measurements [86]. Interestingly, the pioneering calculation

doi:10.6342/NTU202404434

work by Vedmedenko et al. [52] assumed atomic shifts in the spacer layer that separates the two magnetizations to arrive at a nonzero IL-DMI magnitude. Due to these associated microstructures or tilted textures, OAD has the potential to generate horizontal shifts of atoms within the Co and CoFeB layers, influenced by templating effects from the wedged Pt nanostructures. Consequently, we establish a simplified toy model by integrating these horizontal shifts into the Fert-Lévy three-site model, a methodology partially explored as well in related studies [59], though, our model addresses the impacts of both the Pt buffer and spacer layers on the two magnetic layers, relating them with the overall direction and strength of IL-DMI.

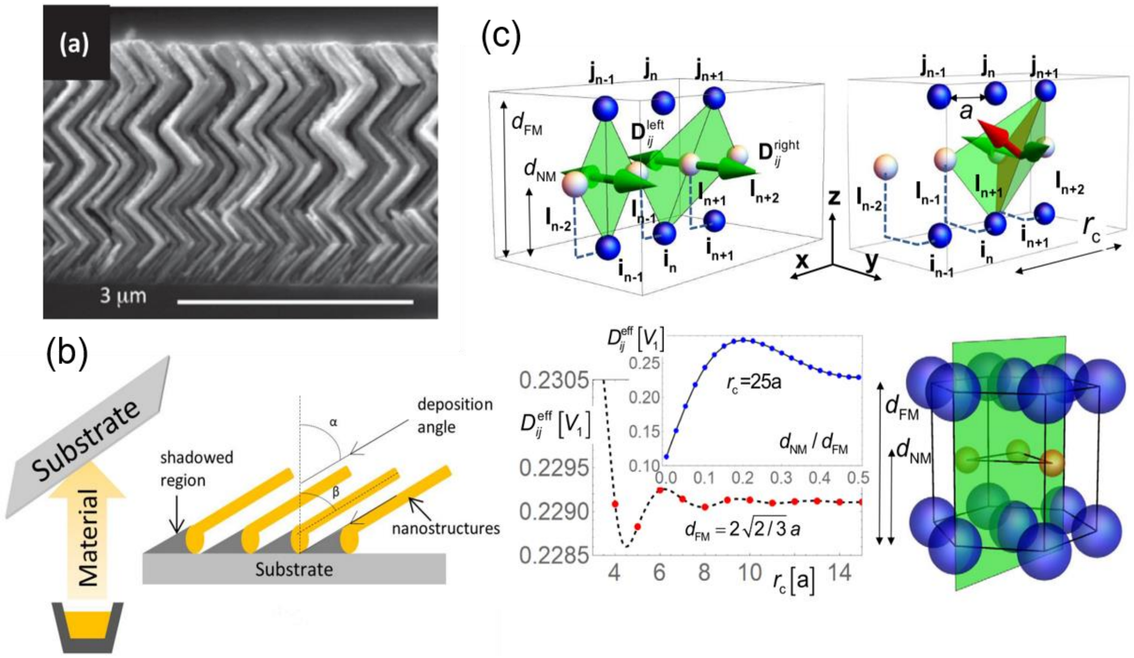

Fig. 4-4 Connecting the microstructures originated from OAD with IL-DMI modelling. (a) SEM micrograph of TiO_2 with Zig-zag like microstructure, obtained by periodically staggering the OAD orientation [108]. (b) Illustration of how the formation of slanted columnar nanostructures is achieved due to the shadow effect [110]. (c) Pioneering atomistic Monte Carlo calculations of IL-DMI [52]. By assuming impurities that shifted

the normal metal atoms in the -y direction, nonzero $\boldsymbol{D}$ magnitude is reached for a hcp structure.

A toy model consisting of two connected Fert-Lévy three-site triangles as illustrated in Fig. 4-5(a) is examined. Similar to the procedures explored in [52,59], DMI vectors from these two triangles are expressed as:

$$\boldsymbol{D}_1(\boldsymbol{R}_{li}, \boldsymbol{R}_{lj}, \boldsymbol{R}_{ij}) = -V_1 \frac{(\boldsymbol{R}_{li} \cdot \boldsymbol{R}_{lj})(\boldsymbol{R}_{li} \times \boldsymbol{R}_{lj})}{|\boldsymbol{R}_{li}|^3 |\boldsymbol{R}_{lj}|^3 |\boldsymbol{R}_{ij}|} \tag{4.2}$$

and

$$\boldsymbol{D}_2(\boldsymbol{R}_{l'i}, \boldsymbol{R}_{l'j}, \boldsymbol{R}_{ij}) = -V_1 \frac{(\boldsymbol{R}_{l'i} \cdot \boldsymbol{R}_{l'j})(\boldsymbol{R}_{l'i} \times \boldsymbol{R}_{l'j})}{|\boldsymbol{R}_{l'i}|^3 |\boldsymbol{R}_{l'j}|^3 |\boldsymbol{R}_{ij}|} \tag{4.3}$$

where various $\boldsymbol{R}$ vectors represent interatomic vectors for the left and right Fert-triangles, respectively, and V_1 is a material-dependent quantity. In the absence of symmetry breaking, the total magnitude of $\boldsymbol{D}$ (sum of $\boldsymbol{D}_1$ & $\boldsymbol{D}_2$) is naturally cancelled out (dashed lines connected triangles in Fig. 4-5(a)). However, when atomic displacements (labeled δ_1 and δ_2) occur in the lower Co or the upper CoFeB layers (due to OAD as elaborated, along x axis), the magnitude of $\boldsymbol{D} = \boldsymbol{D}_1 + \boldsymbol{D}_2$ becomes nonvanishing.

$\boldsymbol{D}$'s total magnitude is calculated by the summation of eqn. (4.2) and eqn. (4.3). To demonstrate a more semi-quantitative agreement with the experimental results, displacements (represented by shifts δ_1 and δ_2) are tentatively set as 8% and 2.4% of the interatomic distance, respectively. Consequently, individually taking δ_1 or δ_2 into consideration results in nonvanishing $\boldsymbol{D}$ with the same polarity (toward + y), and their corresponding magnitudes have a numeric ratio close to the measured H_{DMI} ratio from Pt_1

and Pt$_2$ wedged samples in series S1. Importantly, when simultaneously taking δ_1 & δ_2 into calculation, the resultant relative magnitude of $\boldsymbol{D}$ closely resembles $\boldsymbol{D}(\delta_1) + \boldsymbol{D}(\delta_2)$ (Fig. 4-5(b)), thereby clearly demonstrating additivity which corresponds to the counter-wedge scenario where both displacements are effectively utilized. As depicted in Fig. 4-5(b) all combinations resembling the complete four scenarios discussed in Fig. 4-1 can be qualitatively observed. This additive rule also accurately predicts the relative strengths and overall directions of $\boldsymbol{D}$ for the SAF samples in S2, where it's implied that the wedged Pt$_1$ primarily serves to displace the magnetic atoms in $\boldsymbol{M}_\mathrm{B}$, while wedged Pt$_2$ and Pt$_3$ influence the displacements in the $\boldsymbol{M}_\mathrm{T}$ more profoundly. This analogy, while less straightforward, is drawn from the contrasting contributions of the Pt buffer and spacer layers observed in S1.

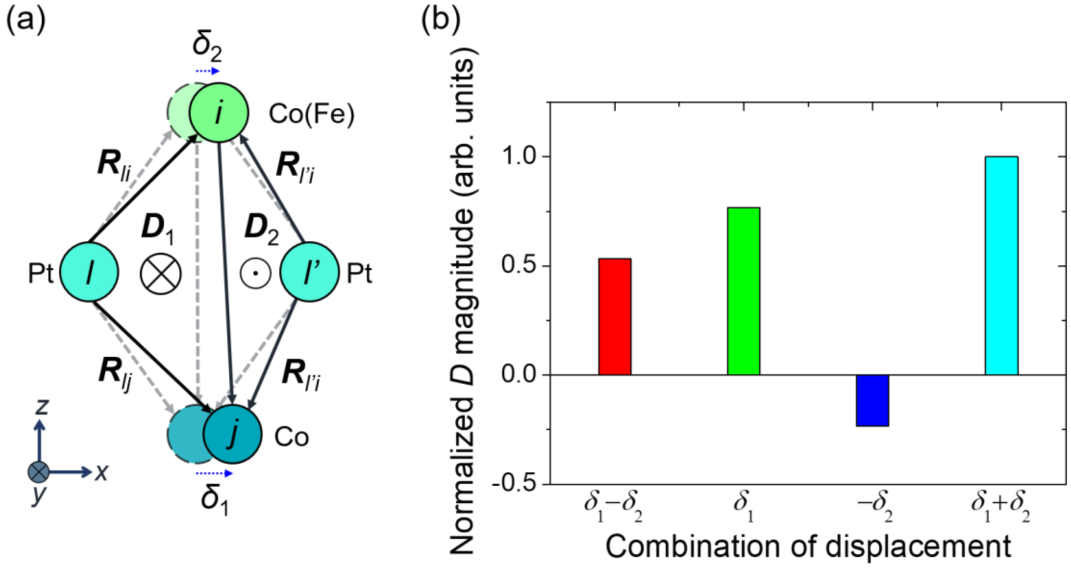

Fig. 4-5 Toy model based on the Fert-Lévy three-site model. (a) Schematic diagram of the toy model, with two connected three-site triangles. The length between the nearest atoms is set to 2.78 Å (lattice constant of Pt(111)). The two displacements δ_1 and δ_2 are set to 8% and 2.4% of the interatomic distance, respectively. (b) Normalized $\boldsymbol{D}$ magnitude

under different displacement combinations. The relative magnitudes coincide nicely with the experimental values reported in Fig. 4-1. In addition, the ***D***'s direction (± y) accurately presents the symmetry breaking rule where δ lies along the x direction. Adopted from [102].

After the investigation proving that our proposed toy model accurately captures the linear combinatory nature of IL-DMI as found in experiments, another instrumental facet of our model pertains to the IL-DMI's response under varying atomic shifts. Schematics in Fig. 4-6(a) shows the configuration between Pt target, $\theta_{\mathrm{incident}}$ and the substrate. The $\theta_{\mathrm{incident}}$ can be controlled by a lift motor, as seen in the appendix (section 6.1). Given the positive correlation between the nanocolumnar structure's angle β and $\theta_{\mathrm{incident}}$ [106], a correspondingly higher δ_1 can be generated as subsequently modelled in Fig. 4-6(b). The calculated normalized ***D*** magnitude (by again employing eqn. (4.2) and (4.3)) is presented in Fig. 4-6(c), which shows a distinctive semi linear increasing trend.

In practice, the structures here are akin to S1 albeit with varying Pt spacer thicknesses ranging from 1.8 nm to 3.3 nm, and $\theta_{\mathrm{incident}}$ altered from 20° to 70°. As shown in Fig. 4-6(d), a mostly monotonically increasing H_{DMI} is observed with elevated $\theta_{\mathrm{incident}}$, with H_{DMI} reaching as high as 285 Oe (corresponding to $E_{\mathrm{DMI}} \approx 28.4\ \mu\mathrm{J/m^2}$ by eqn. (2.5)) under low Pt spacer thickness of 1.8 nm and high $\theta_{\mathrm{incident}} = 70°$, a four-fold increase from $\theta_{\mathrm{incident}} = 20°$ and is one of the higher values reported in IL-DMI systems. This result is consistent with the increased aforementioned increased structure angle as the deposition angle is increased. Samples with SAF structures similar to S2 are also tested, where the spacer thickness is unchanged to preserve the SAF characteristic, and focus is placed on the H_{DMI}-$\theta_{\mathrm{incident}}$ behavior. Fig. 4-6(e) shows SAF structure has a large enhancement in H_{DMI} of over four times by changing $\theta_{\mathrm{incident}}$ from 20° to 70°, very

doi:10.6342/NTU202404434

similar to its type-T counterpart.

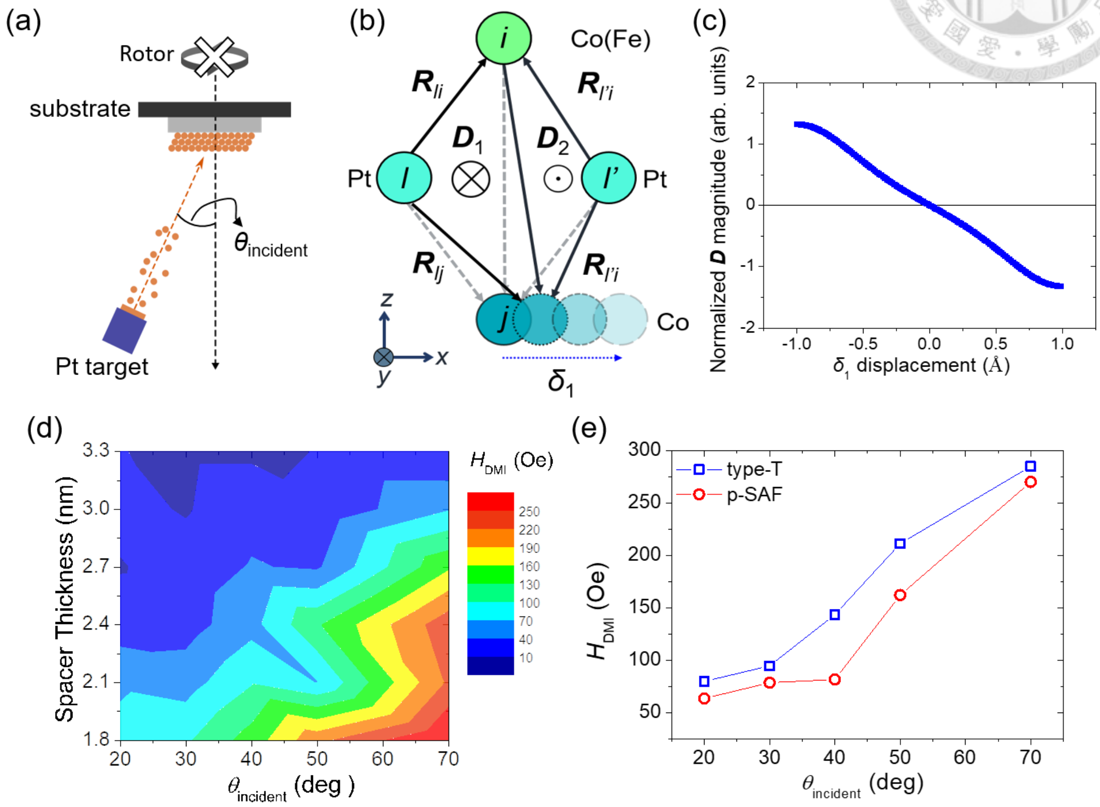

Fig. 4-6 Relations between the incident angle and H_{DMI}. (a) Schematics of the incident angle $\theta_{\mathrm{incident}}$ with regard to the sample substrate. $\theta_{\mathrm{incident}}$ ranges from 20° to 70° (b) Since the structure angle β of the nanocolumnar structures rises with increased $\theta_{\mathrm{incident}}$ [106], we modelled the resultant IL-DMI by increasing the atomic shift in the Co layer as shown by the displacement of atom "j", δ_1, in the x direction. (c) Corresponding calculated $\boldsymbol{D}$ magnitude as a function of δ_1. (d) Contour plot of type-T sample's H_{DMI} as a function of Pt spacer thickness and $\theta_{\mathrm{incident}}$. (e) H_{DMI} vs. $\theta_{\mathrm{incident}}$ for both type-T and SAF structures, the spacer Pt thickness of the type-T structure is 1.8 nm. Following the established protocol, $|H_{\mathrm{in}}|$ during angle dependent loop-shift measurement is fixed at 200 Oe. All samples are grown with the counter-wedge technique. Figures modified from [102].

It’s also noteworthy that, although cannot be directly inferred from our toy model, the findings from S1 and S2 samples unequivocally point out that the earlier a wedged layer is grown onto the substrate, the greater an influence it has on the interlayer DMI strength (can be implicitly seen by tentatively assigning $\delta_1 = 0.3\ \delta_2$ in Fig. 4-5), consistent with the concept of template and shadow effect as the columnar structure formation is dictated by the atoms initially sputtered.

In summary, the proposed toy model nicely supports the experimental results and provides insight not only into the physical origin of IL-DMI but also offers valuable guidance to effectively fine-tune the strength of interlayer chiral exchange, as the fabrication processes see fit.

doi:10.6342/NTU202404434

4.3 Device-to-device properties homogeneity improved by counter-wedge deposition.

4.3.1 Field-Free Switching Characteristics

Having unveiled the controllability of IL-DMI through azimuthal engineering, we proceed to test its practical usage by demonstrating field-free current-induced switching utilizing the two counter-wedge deposited samples from S1 and S2. Hall bar devices with different orientations are employed for this purpose. This setup results in a rotating φ_{D} relative to the *x*-axis of individual devices (see Fig. 4-1(a)) facilitating the investigation of the angle dependence of switching. The switching experiments are conducted at a magnet-free probe station. Robust and deterministic field-free current-driven switching is achievable in both type-T and SAF configurations as shown in Fig. 4-7 (a) and (b), and a strong correlation is found between the switching percentage, and the interplay between $\boldsymbol{D}$ and spin (charge) current. When subject to a substantial charge current I_{pulse} along the current channel (*x*-axis), magnetization dynamics are triggered by the conventional *y*-polarized spin (σ), leading to the eventual collinear alignment of $\boldsymbol{M}_{\mathrm{T}}$ and $\boldsymbol{M}_{\mathrm{B}}$ toward the *y*-axis due to current-induced damping like SOT ($\tau_{\mathrm{DL}} \propto m \times (m \times \sigma)$) [91,111]. Put differently, σ induces an in-plane component in both magnetizations. Consequently, $\boldsymbol{M}_{\mathrm{T}}$ and $\boldsymbol{M}_{\mathrm{B}}$ experience $\boldsymbol{H}_{\mathrm{DMI}}$ which is proportional to $\sigma \times \boldsymbol{D}$ and $\boldsymbol{D} \times \sigma$, (recall $\boldsymbol{H}_{\mathrm{DMI(T)}} = -\boldsymbol{D} \times \boldsymbol{M}_{\mathrm{B}}$ and $\boldsymbol{H}_{\mathrm{DMI(B)}} = \boldsymbol{D} \times \boldsymbol{M}_{\mathrm{T}}$) respectively. Fig. 4-7(c) shows that when $\varphi_{\mathrm{D}} = 0°$ (180°), $\sigma \times \boldsymbol{D}$ is minimized (maximized), causing $\boldsymbol{M}_{\mathrm{T}}$ to deterministically stabilize in the $\pm z$ directions, while in contrast $\boldsymbol{M}_{\mathrm{B}}$ relaxes to an opposite direction relative to $\boldsymbol{M}_{\mathrm{T}}$, completing a deterministic switching cycle. On the contrary, when $\varphi_D = 90°$ and $270°$, $\sigma \times \boldsymbol{D}$ reduces to null, resulting in experimentally confirmed failed switching (Fig. 4-7(a) and (b)). Note that this above model is a more general case which explains the field-free switching behavior in both type-T and SAF devices, while a limited case exclusively for type-T has already been modelled and experimentally confirmed in Sec. 2.3.

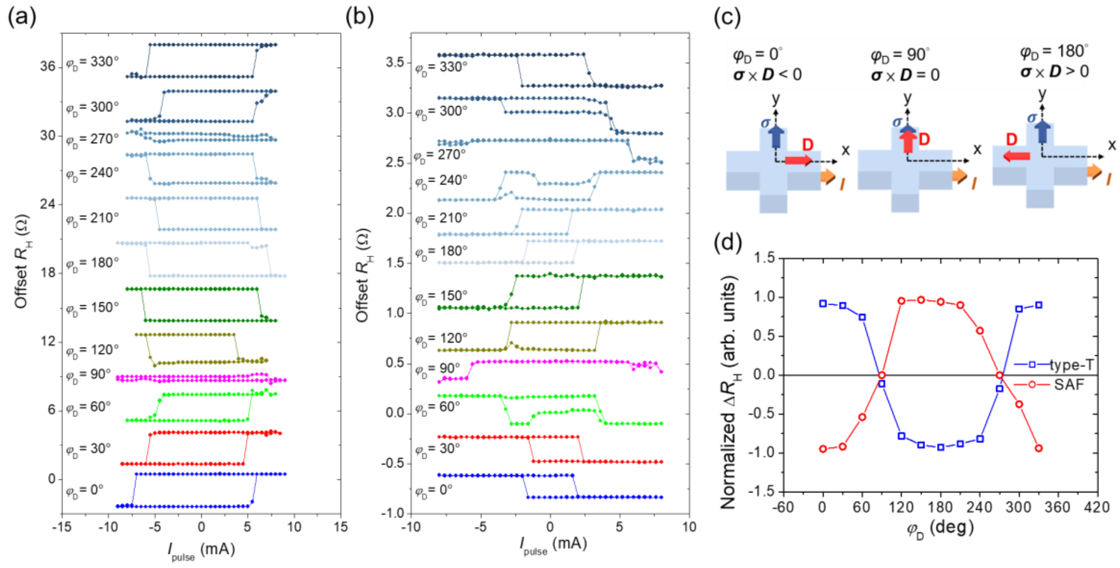

Fig. 4-7 Angle dependent field-free current-induced SOT switching facilitated by counter wedge induced IL-DMI. (a) and (b) showcase field-free SOT switching behaviors at various φ_D angles in type-T and SAF counter-wedged devices, respectively. Notably, there's a change in polarity relative to the evolution of φ_D with failed switching occurring at $\varphi_D = 90°$ and $\varphi_D = 270°$. (c) Illustration of the field-free switching mechanism. (d) The switching percentage, normalized to the R_H obtained from field-scan, is depicted for both types of samples as a function of φ_D. Figures reprinted from[102].

The switching percentages as a function of φ_D is compiled in Fig. 4-7(d). The maximum switching ratio (92% and 94% for type-T and SAF cases, respectively) occur at $\varphi_D = 0°$ and $180°$, consistent with $\varphi_D || I_{pulse}$ maximizes the z-oriented assist fields. This relatively high switching percentage improves over previous works [60,62], possibly due to the enhanced H_{DMI}, which negates the depinning fields or the Oersted fringing fields.

For realistic applications of IL-DMI and the counter-wedge technique, it's essential to consider various device characteristics. To assess the viability of devices' operation, factors such as SOT performance, device reliability, including repeatability and thermal stability can serve as crucial figures of merit.

The effective fields produced by the current-induced damping-like SOT (DL-SOT) are characterized by the hysteresis loop shift method [66]. The two representative samples (type-T and SAF) presented here are identical to those used for measuring field-free switching in Fig. 4-7. As shown in Fig. 4-8(a), the extracted $H_z^{\mathrm{eff}}/I_{\mathrm{DC}}$ of the type-T sample indicates that the PMA magnetization experiences a negligible DL-SOT response of $H_z^{\mathrm{eff}}/I_{\mathrm{DC}} \leq 1.0$ Oe/mA, in line with the fact that the two Pt layers with identical thicknesses would effectively cancel out the overall spin current. However, a much larger $H_z^{\mathrm{eff}}/I_{\mathrm{DC}} \approx 13.1$ Oe/mA is observed for the SAF sample under sufficiently high x-direction field H_x. Note that in the case of type-T devices, field-free switching can be switched entirely relying on H_{DMI} due to the in-plane magnetization reversal of the CoFeB layer, without the Co layer experiencing substantial SOT [53], of which the contribution cannot be captured by the current-induced hysteresis-loop shift method. On the other hand, H_{DMI} only serves as an assist field in SAF devices, requiring the PMA magnetizations to experience sizable SOT to activate magnetization dynamics.

Thermal stability factor (Δ) is then measured by field-free switching to evaluate the robustness of the device. Under the thermally-activated switching scenario (due to the long duration of applied current pulse width (t_{pulse})), equation $I_c = I_{c0}\left[1-\frac{1}{\Delta}\ln\left(\frac{t_{\mathrm{pulse}}}{\tau_0}\right)\right]$ is employed [112] from which the zero thermal critical switching current, I_{c0}, and the thermal stability Δ can be extracted, with $\tau_0 \approx$ 1 ns describing the intrinsic attempt rate. In practice, by varying t_{pulse} from 200 μs to 2 ms, I_{c0} and Δ are extracted by linearly fitting I_c to $\ln(\frac{t_{\text{pulse}}}{\tau_0})$, as shown in Fig. 4-8(b). Δ = 24.9 is insufficient for long-term data storage functionalities ($\Delta \geq 45$ required for 10-year information retention [113]), but still comparable to other contemporary reports [77,114]. This may be improved by further stack engineering.

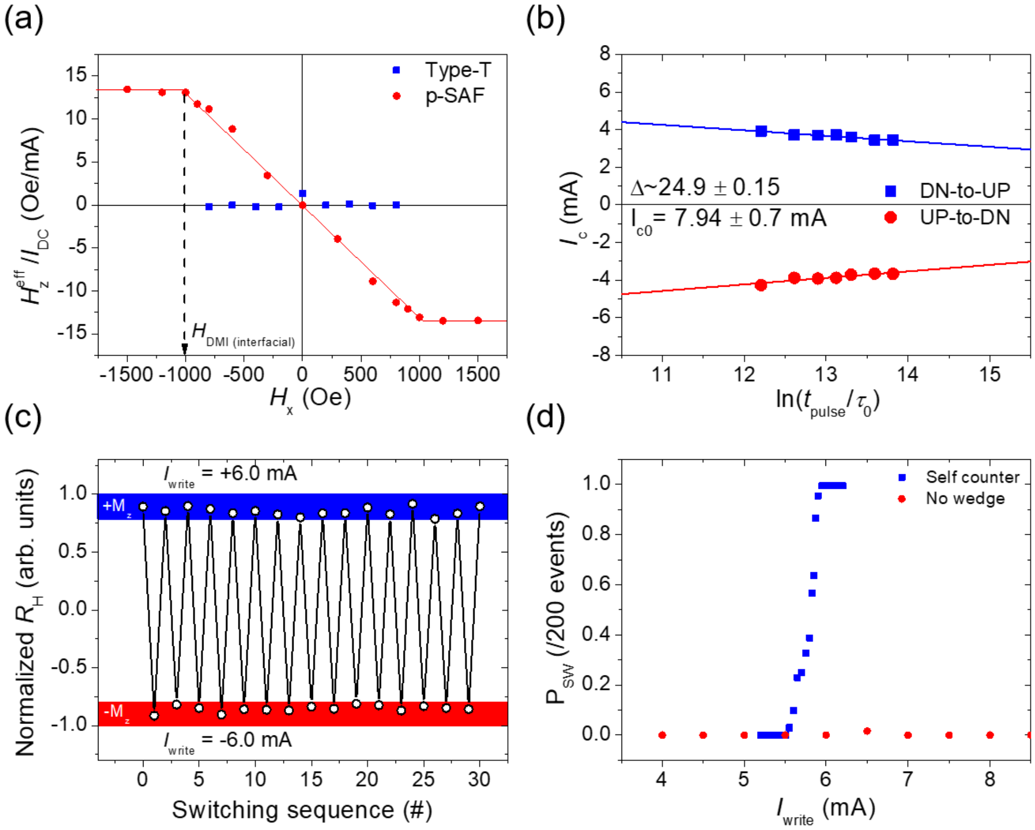

Fig. 4-8 (a) Strength of DL-SOT effective fields experienced by the PMA magnetization characterized by $H_z^{\text{eff}}/I_{\text{DC}}$. Saturation field (interfacial H_{DMI}) of the SAF sample labeled with black arrow. (b) Pulse width dependent measurement of critical switching current I_c. (c) Repeated switching events of the self-counter-wedged SAF device under I_{write} with alternating polarity. The initial 30 sequences are shown from the complete 300 sequences.

doi:10.6342/NTU202404434

(d) Comparison of switching probability (P_{sw}) as a function of I_{write} between the self-counter-wedged SAF sample, and a control device prepared without wedge. Adopted from [102].

Current pulses with opposite polarities are injected into the SAF sample (φ_{D} = 90° device) with 50 ms pulse width and a current magnitude of $I_{\mathrm{write}} = \pm 6$ mA to test the field-free operation's repeatability. Robust reversible switching behavior is successfully demonstrated, shown in Fig. 4-8(c), by treating a single switching's corresponding normalized $\Delta R_{\mathrm{H}} \geq \pm\ 0.8$ as a successful event. Following an identical procedure, the switching percentage under different I_{write} is plotted in Fig. 4-8(d), with a control sample showcasing failed field-free switching in a non-wedged device, regardless of the applied current.

4.3.2 Self Counter-Wedge Design for Structural Homogeneity

In the preceding section, we demonstrated favorable switching characteristics with robust switching and behaviors following the IL-DMI framework. However, the conventional OAD faces challenges in industrial fabrication due to said method forming a thickness gradient that accompanies OAD which is detrimental to the consistency of device behavior. Here, in Fig. 4-9, the thickness gradient is definitively showcased. Calculated from this demonstrative CoFeB atom flow, the thickness difference across a typical device is merely ~ 5×10^{-4} nm (far thinner than a monolayer), rendering the thickness difference itself impossible to be the origin of IL-DMI. However, this thickness difference is exacerbated to > 1 nm across a 3-inch wafer, sufficient to induce significant disparities in spatially separated devices, such as magnetic properties [115,116] or

doi:10.6342/NTU202404434

difference in spin current generation capabilities [117-119].

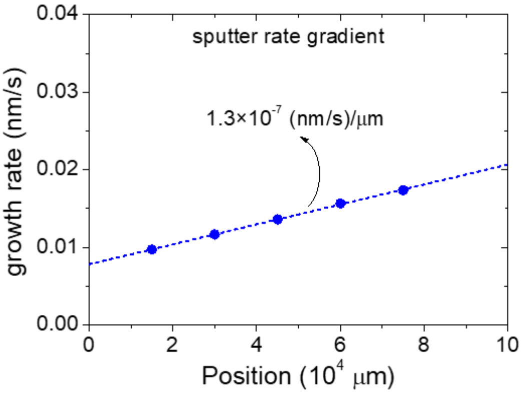

Fig. 4-9 The sputter rate's spacial variation from a representative CoFeB atom flow via OAD. Five devices under test formed a straight line with 1.5 cm interval on the sample holder, placed collinear to the CoFeB atom flow. The sputter rate gradient is calculated from 5000 s of growth with a power of 30 Watts.

Azimuthal engineering strategy already offers opportunities for attaining high H_{DMI} and facilitating field-free switching. Moreover, the counter-wedge technique already represents an advancement over conventional OAD methods since, in principle, the antiparallel thickness gradients in discrete Pt layers cancel each other out. However, counter-wedge faces a limitation where the thickness mitigation is achieved only after the deposition of multiple layers, potentially leading to the formation of inclined layer stacks (as depicted in Fig. 4-1(a) and Fig. 4-3(a)). Here, we introduce an enhancement method termed "self counter-wedge" where Pt layers are grown sequentially via an OAD followed by a reversed OAD process. Through this approach, the thickness gradient is preliminarily smoothened within individual Pt layers. This is based on two previous observations:

doi:10.6342/NTU202404434

1. Contributions from different layers. As stated before, the contributions from multiple wedged layers can be linearly combined.
2. Template effect, where earlier a wedged layer is deposited, higher its contributing IL-DMI strength.

In Fig. 4-10(a), the SAF structure featuring Pt_1, Pt_2 and Pt_3 grown using the self counter-wedge protocol is depicted. The enlarged image emphasizes that the sequences of OAD and reversed OAD utilized for Pt_2 and Pt_3 are reversed compared to Pt_1 to exploit the overall cumulative contributions.

For a comparative analysis of the uniformity between structures grown using self-counter and standard counter wedge techniques, SAF devices are deposited on a 3-inch (7.6 cm) wafer, as illustrated in Fig. 4-10(b). Here, five zones with 1-cm spacings are selected to evaluate their spatial-dependent device characteristics. First, a straightforward measurement of their respective resistivity, as displayed in Fig. 4-10(b), indicate the spatial homogeneity of electrical property. The spatial variation in resistivity is suppressed to below ± 5 % in the case of self-counter wedge, where a significant ± 20 % is recorded for the counter case, possibly attributed to the decreased interface roughness [120]. This result is rather straightforward at demonstrating the higher consistency of film thickness across a sizable distance. Aside from purely electrical behavior, magnetic switching characteristics are also examined. As depicted in Fig. 4-10(c), consistent field-free switching is achieved for self counter-wedged devices across all five zones. The normalized ΔR_H and critical switching current I_c of the tested devices are summarized in Fig. 4-10(d) and (e), respectively. Without the immediate thickness compensation, as in the case of counter-wedge structures, the switching percentage exhibits considerable variation, even resulting in failed switching or reversed switching polarity in some cases. This is likely attributed to the phenomenon of slanted layers, which can be exacerbated

doi:10.6342/NTU202404434

by the spatial deviation of the devices from the nominal sputtering position. The self-counter case, on the other hand, demonstrates greater consistency across these five zones. Likewise, a relatively stable I_c is reported whereas for the counter-wedge case, the variation in I_c exceeds 5 mA among different regions.

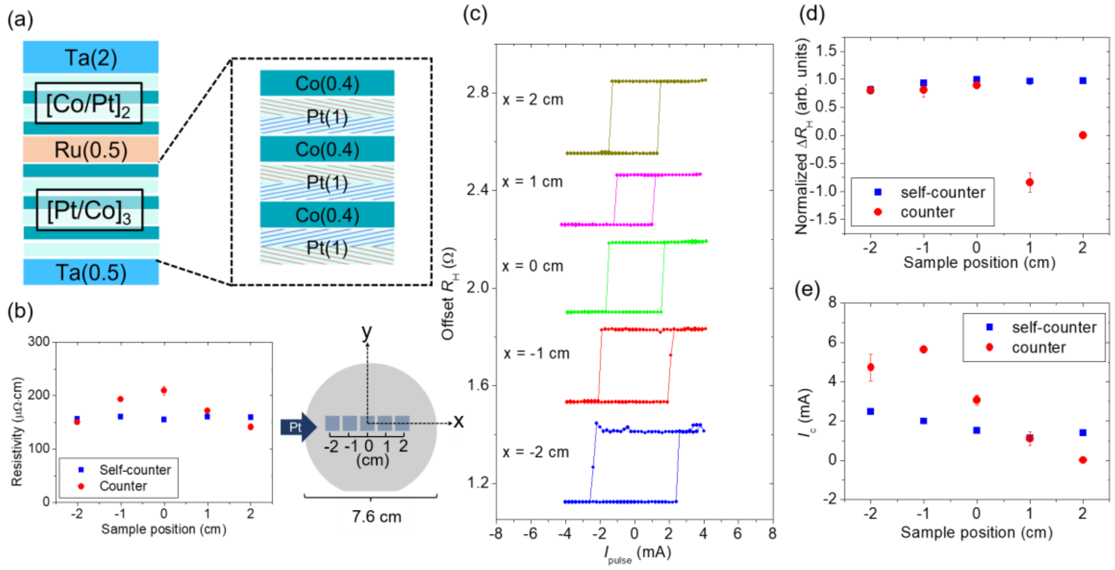

Fig. 4-10 By employing a self-counter wedge technique, improved field-free switching homogeneity is achieved. (a) The structure of the self-counter wedged SAF stack is depicted, where the non-uniformity induced by OAD is mitigated in individual layers. An enlarged section highlights the opposite order of OAD and reversed OAD for the three Pt layers involved. (b) Devices deposited on a 3-inch (7.6 cm) wafer are shown, with five zones chosen along the Pt atom flow direction (*x*-axis) at spacings of 1 cm to test their field-free switching characteristics. Also presented is the spacial variation in resistivity along the deposition direction. (c) Switching loops of devices with $\varphi_D = 180°$, obtained from the five devices. (d) and (e) Comparison of the normalized switching percentage and critical switching current, respectively, of devices with $\varphi_D = 180°$ from different zones between the two wedge-grown scenarios. Figure reprinted from [102].

In addition, we hereby prove that proper OAD design utilized in self counter-wedge maintains a sizable H_{DMI}, in both type-T and SAF structures. For a type-T structure, schematics of the "self-counter wedge" deposition scheme is illustrated in Fig. 4-11(a). Following the exhibition convention established, blue/red stripes indicate the antiparallel deposition directions due to OAD and reversed OAD employed on the lower/upper half of the bottom Pt layer. This approach leads to a weakened but nevertheless still sizable H_{DMI} of 51.8 Oe (Fig. 4-11(b)). The angle dependence of $\varphi_{\mathrm{D}} \approx 270°$ highlights the dominant influence of the lower half of the Pt layer, which overcompensates for the upper half which neighbors the Co layer (contributing to $\varphi_{\mathrm{D}} \approx 90°$).

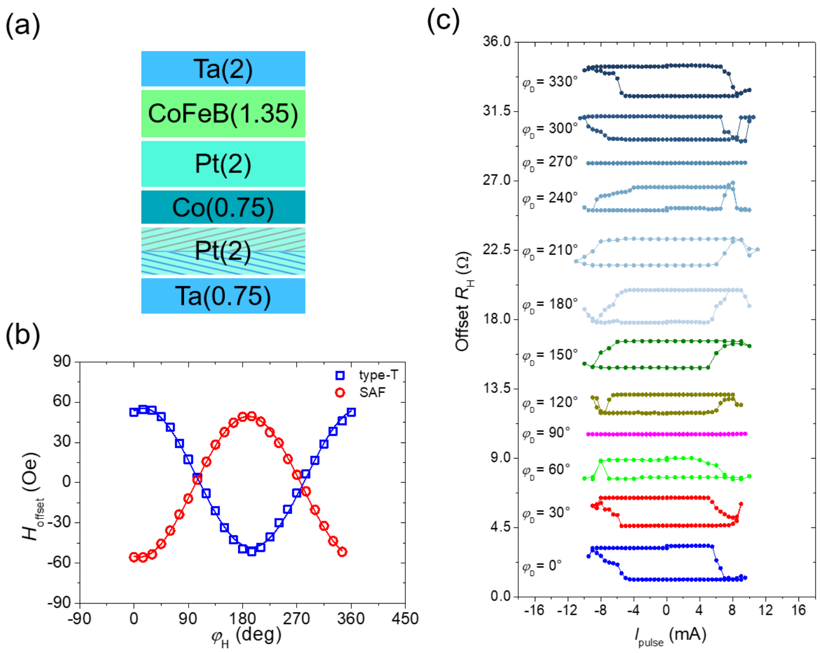

Fig. 4-11 (a) Illustration of the structure and the self-counter-wedge condition in a device with type-T configuration. (b) Angle dependent loop shift of type-T and SAF devices, both grown with self counter-wedge. (c) Switching curves of the type-T self-counter-wedged sample, with different φ_{D}. While field-free switching remains achievable, there's obvious “switch-back” behaviors, likely due to the reduced H_{DMI}.

The tested field-free switching loops of the type-T self-counter wedged sample are compiled in Fig. 4-11(c). It’s obvious that a high switching percentage of ≈ 80% can be achieved in 0°/180° devices. However, the switching loops can show a “switch back” behavior, where the deterministic state of R_{H} cannot be maintained under high current. This phenomenon has been observed in other works [121], and we attribute this phenomenon to the lowered H_{DMI} causing a degraded symmetry breaking effect. For the self counter-wedged devices with SAF structure, the individual contributions from Pt_1, Pt_2 and Pt_3 layers are detailed in Fig. 4-12(a), where the consistent directional alignment of their resulting $\boldsymbol{D}$ is evident. Notably, the combinatory nature of IL-DMI is evident here, with the contributions from Pt_1, Pt_2 and Pt_3 adding up to 62.5 Oe, fairly close to the reported $H_{\mathrm{DMI}} = 52.5$ Oe (Fig. 4-11(b)) in the combined structure. Wedged Pt layers in the top FM layer, on the other hand, contributes little to the overall interlayer DMI strength, with their corresponding H_{DMI} negligibly small at around 5.6 Oe (Fig. 4-12(b)). This result echoes our observation that higher-level (later-grown) layers contribute much less to the interlayer DMI while compared to the bottom-level (earlier-grown) layers.

doi:10.6342/NTU202404434

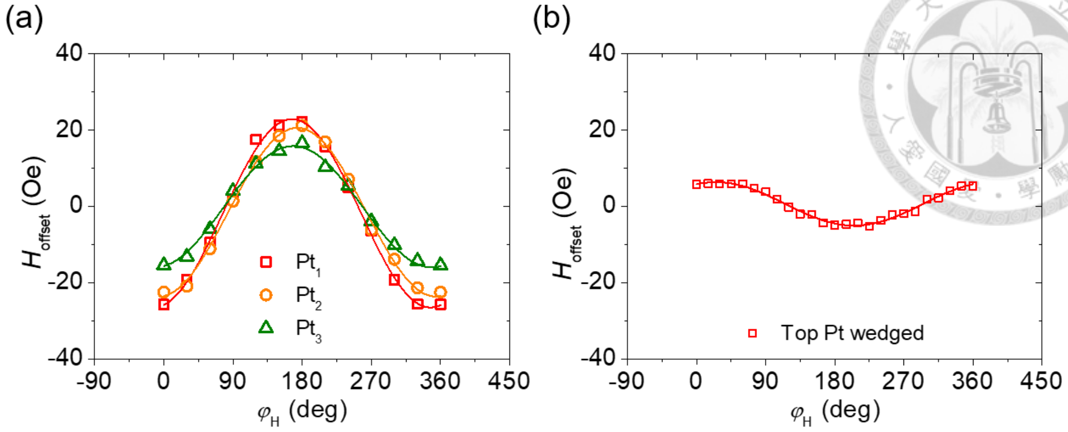

Fig. 4-12 Investigation of individual layer's contribution in the self-counter wedge scenario. (a) Contributions of self-counter wedge employed on Pt_1, Pt_2 and Pt_3 layers with H_{DMI} magnitudes being 24.6 Oe, 22.0 Oe and 15.9 Oe, respectively. Note their constructive relationship and parallel alignment of $\boldsymbol{D}$ with regard to the overall case reported in Fig. 4-11(b). (b) Angle scan for H_{offset} when the top Pt layers are wedge deposited instead. Note the weak H_{DMI} of 5.7 Oe. Reprinted from [102].

4.3.3 Ruderman-Kittel-Kasuya-Yoshida (RKKY) type IL-DMI

In section 4.2, the IL-DMI's dependence on the spacer thickness has been slightly explored. Judging from the contour plot in Fig. 4-6, a simple monotonic increase in H_{DMI} is observed with reduced Pt thickness, regardless of the incident angle, or the magnetic system (either type-T or double PMA). However, this is not the end of the story. In 1976, Smith [17] predicted that for a ferromagnetic layer, spin-orbit scattering of conduction electrons by high SOC impurities gives rise to DMI due to the RKKY mechanism (Fert and Lévy capitalized on this to develop their famous three-site model [16]). So far, rock solid correlation between DMI and RKKY has yet to be experimentally verified.

IL-DMI provides a unique opportunity in the sense that compared to other versions of DMI (such as bulk DMI and interfacial DMI), its spin system is much simpler (can be considered merely comprising of two spins in a macroscopic picture, as described by eqn. (1.13)) and the $\boldsymbol{D}$ direction can be subsequently determined. In this section, we experimentally report the profound correlations between IL-DMI (possibly DMI in general) and the conventional RKKY interaction.

Analytical calculations based on the RKKY formalism are recently performed by Schoenmaker [10] by using the second-order perturbation theory while additionally introducing an x-oriented symmetry breaking factor. The derived $\boldsymbol{D}$ as a function of exchange length, along the conventional behavior of RKKY is reprinted in Fig. 4-13(a). Coherent with the experimental results reported so far in this dissertation, $\boldsymbol{D}$ is always perpendicular to the symmetry breaking (thus the $\widetilde{D}_{\mathrm{y}}$ annotation).

doi:10.6342/NTU202404434

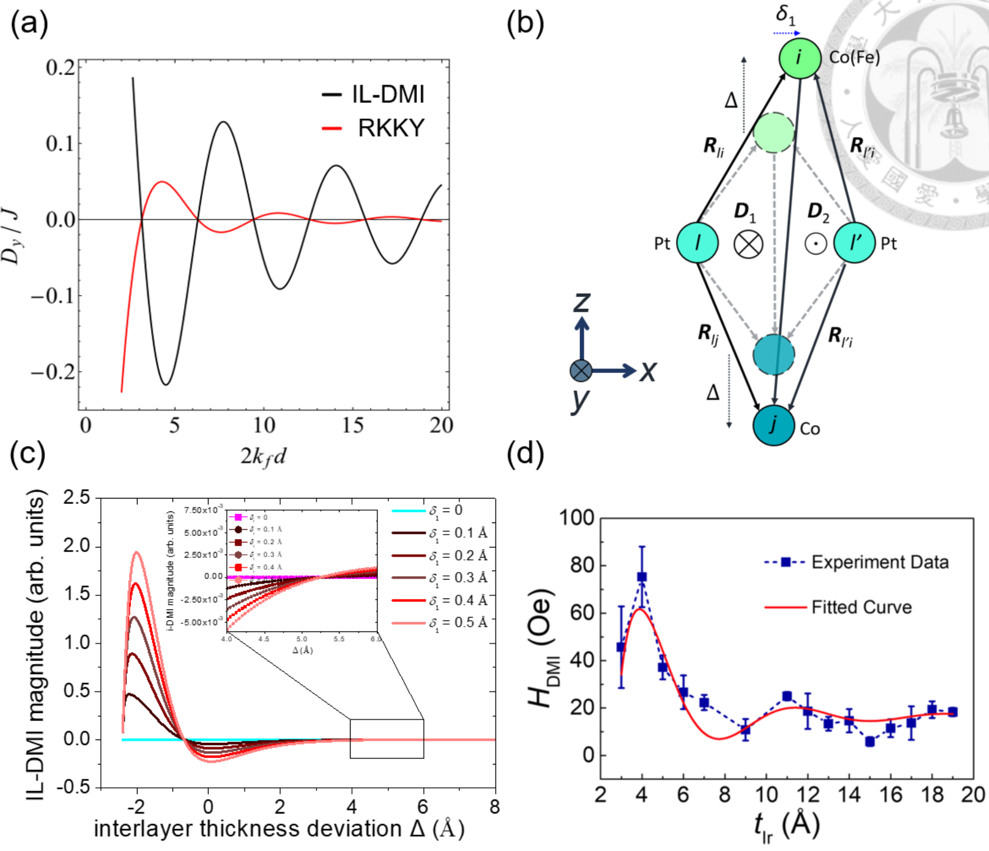

Fig. 4-13 Theoretical and model predictions on RKKY type IL-DMI, as well as previous attempts. (a) By additionally introducing an *x*-oriented symmetry breaking factor, IL-DMI can be calculated following the RKKY formalism. Note the damped oscillation for both IL-DMI and RKKY, and the exactly identical oscillation period. Reprinted from [10]. (b) Utilizing our proposed shifted Fert-Lévy model, we attempted to see if the oscillatory behavior with interlayer thickness can be captured. (c) Corresponding IL-DMI strength calculated based on the model described in (b). Depending on the interlayer thickness deviation, oscillatory behavior is observed, where the inset shows the second intersection with 0. Note that this model is entirely material-independent, a deficiency discussed in the main text. (d) Previous results by Liang et al.. While oscillating H_{DMI} is observed, definitive sign change in $\boldsymbol{D}$ cannot be observed due to the randomness in $\boldsymbol{D}$ directions and low H_{DMI} strength. Reprinted from [59].

Importantly, the calculated $\widetilde{D}_{\mathrm{y}}$ shows damped oscillation with regard to the exchange length where its polarity oscillates between ± y directions, with the oscillation period exactly identical to the RKKY interaction (represented by $\tilde{J}$). Though, the calculated attenuation rate for the two interactions are different, in which $\widetilde{D}_{\mathrm{y}} \propto \sin(2k_f d + \phi)/d$ and $\tilde{J} \propto \sin(2k_f d + \phi)/d^2$ [10].On the other hand, we investigated if our previously proposed shifted Fert-Lévy model can provide insight on the thickness dependence of the IL-DMI strength. As schematically shown in Fig. 4-13(b), by assigning an atomic shift δ_1 and changing the y coordinate of the FM atoms from the initial condition described in Fig. 4-5(a) (thus the interlayer thickness Δ), the normalized ***D*** magnitude is reported in Fig. 4-13(c). It's clear that as δ_1 increases, the ***D*** magnitude also rises. In addition, oscillatory behavior also appears, suggesting that the shifted Fert-Lévy model also provides some insight into the thickness dependence of IL-DMI. Though, due to the rather simplified picture of our model (such as only considering atomically thin thickness for individual layers, and neglecting the difference between different elements), no realistic predictions can be made on the periodicity or the rate of attenuation of IL-DMI.

Very recent works have attempted to clarify this issue. Liang et al. [59] demonstrated oscillating H_{DMI} magnitude as shown in Fig. 4-13(d) with an Iridium spacer. However, due to the randomness in the ***D*** direction (which violates the 3rd Moriya rule) and the low H_{DMI}, clear parallel/antiparallel direction change of ***D*** wasn't demonstrated.

We first start from two simple scenarios as a control experiment. In the first case, a type-T structure with a pure Pt spacer is prepared. type-T is selected to avoid the conventional RKKY interaction in a double PMA system vastly complicating ***D*** magnitude comparison (see eqn. (4.1)). As shown in Fig. 4-14(a), and also implicitly stated in section 4.2, a monotonic decrease of H_{DMI} is observed with a unitary ***D*** direction of 270° (due to the x-oriented OAD) regardless of the spacer thickness, which spans from fairly long range (t_{Pt} = 4 nm) to right before PMA disappears (t_{Pt} = 2 nm). This result implicitly indicates that similar to the RKKY interaction, for a significant oscillatory behavior (in the case of RKKY, from ferromagnetic to antiferromagnetic) to occur, adequate spacer such as Ru or Ir etc. [12] might show a much more profound oscillation.

In the second control experiment, we replaced the pure Pt spacer with Pt(0.9)/Ru(t) where the Pt(0.9) serves to maintain robust PMA. According to theoretical predictions, since DMI originated from an additional term in RKKY formulation, a high RKKY strength mediator such as Ru should also bring about significant oscillatory behavior in IL-DMI. To confirm that the Ru spacer do not contribute any artifacts to H_{DMI} measurement arising from the conventional RKKY mechanism, the control multilayer stack is prepared without introducing symmetry breaking. From Fig. 4-14(b), the aligning in-plane field during measurement (which might create parallel components in $\boldsymbol{M}_{\mathrm{Co}}$ and $\boldsymbol{M}_{\mathrm{CoFeB}}$) generates negligible H_{DMI}, excluding contributions from RKKY.

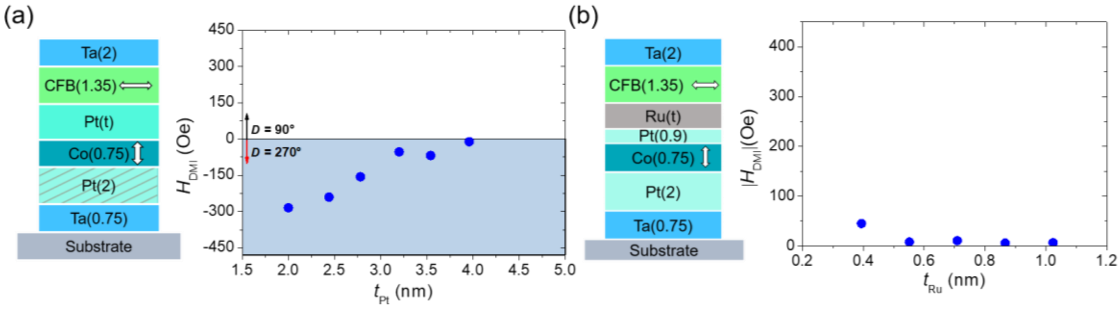

Fig. 4-14 (a) H_{DMI} response in a type-T system, where the mediating spacer is a simple Pt layer. The buffer Pt is wedge deposited to generate symmetry breaking. Note this structure is similar to the ones from the previous sections, just emphasizing the t_{Pt} dependence. (b) A control experiment where the mediating spacer is Pt(0.9)/Ru(t). Without the Pt buffer wedge, the $|H_{\mathrm{DMI}}|$ magnitude is fairly low with random $\boldsymbol{D}$ directions, excluding the possibility of a symmetric contribution (i.e. conventional RKKY mediated by Ru).

Now, when the symmetry breaking is reintroduced (as shown in Fig. 4-15(a) top), a definitive damped oscillatory IL-DMI is observed, as reported in Fig. 4-15(b). The exchange coupling is obviously demonstrated to oscillate across zero ($\boldsymbol{D}$ can and only can take either 90° or 270°), in stark contrast to previous attempts, as well as the case of pure Pt spacer. Moreover, the oscillation can be well fitted by $D \propto \sin(2\pi t_{\mathrm{Ru}}/\lambda_F + \phi)/t_{\mathrm{Ru}}$, where a oscillation period $\lambda_F \approx 9.6$ Å is extracted. This nicely agrees with the reported 11.5 Å in the RKKY scenario from the seminal work by Parkin et al. [122]. We additionally prepared a series of SAF samples (structure shown in Fig. 4-15(a) bottom) with varying Ru spacer thicknesses and captured the resultant RKKY effective field H_{RKKY}, plotted alongside IL-DMI data in Fig. 4-15(b). The strength of RKKY in the FM region cannot be determined from the hysteresis, still, the clear overlapping of the RKKY and IL-DMI's Ru thickness dependences show good self-consistency. One can see that the two AFM regions occur at roughly Ru = 0.7 ~ 1 nm and 1.5 to 1.9 nm (corresponds to $\boldsymbol{D}$ = 270° in the IL-DMI case), while other thicknesses show FM coupling ($\boldsymbol{D}$ = 90° in the IL-DMI case). Note that even though the extracted λ_F of 9.6 Å is fairly close to the value reported over 30 years ago, there's a horizontal shift (around 0.4 nm in the negative t_{Ru} direction) in the AFM to FM transition (or $\boldsymbol{D}$ = 90°/270° in the case of IL-DMI) when comparing Fig. 4-15(b) with (c). This is attributed to the ϕ term in the fitting function, which might be due to the inevitable existence of Pt adjacent to the Ru layer, possibly modifying the electron hybridization of the long-range superexchange.

Overall, these results are the first definitive experimental confirmation connecting IL-DMI (perhaps DMI in general) to the RKKY mechanism, where RKKY spacers are required to generate damped oscillation in IL-DMI. In practical implementation, it provides an alternative approach to better harnessing IL-DMI, similar to how RKKY is exploited to generate SAF structures. For example, the switching polarity in current-induced SOT switching (as reported in section 2.3 and 4.3) can now be controlled by the Ru spacer thickness rather than by the symmetry breaking direction.

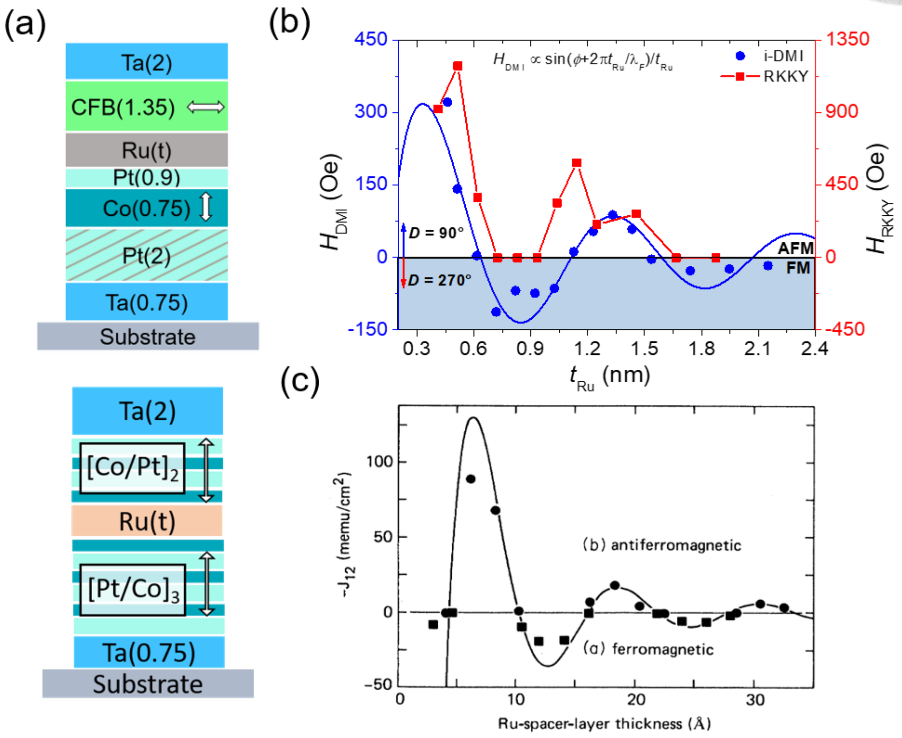

Fig. 4-15 Oscillatory IL-DMI mediated by a Ru spacer. (a) Top: structure of the type-T system with a Pt(0.9)/Ru(t) spacer, where wedged Pt buffer provides symmetry breaking. Bottom: PMA SAF structure with a Ru spacer to capture the conventional RKKY behavior as a function of Ru thickness. (b) Oscillatory IL-DMI observed in the type-T system (blue data set). Its thickness dependence is well fitted by $D \propto \sin(2\pi t_{\mathrm{Ru}}/\lambda_F + \phi)/t_{\mathrm{Ru}}$ as shown by the blue curve where an oscillation period of 0.96 nm is extracted. The Ru's thickness dependence of RKKY is also reported as shown by the red data set. The good overlap between the IL-DMI and RKKY's thickness dependence clearly shows they share a similar oscillation period, as predicted by theoretical calculations. (c) The seminal work by Parkin et al. on the RKKY exchange strength with Ru thickness. Reprinted from [122].

4.4 Brief Conclusions

In this chapter, we started by observing the tunable and linear combinatory strength of H_{DMI} in both type-T and SAF systems. In particular, identical wedge conditions applied on distinct layers contribute opposite $\boldsymbol{D}$ polarities. These results serve as the prime inspiration to the development of our proposed shifted Fert-Lévy three site model. This model, based on the atomic shift induced by the OAD process, successfully explains the linear combinatory contribution to $\boldsymbol{D}$ from individual layers, and the monotonic increasing $\boldsymbol{D}$ magnitude at elevated deposition angles. On top of this, the negligible IL-DMI induced from magnetic anisotropy engineering from section 3.2 also supports the notion that the origin of IL-DMI is structurally related.

Furthermore, by incorporating a standard RKKY spacer, Ru, into the mediating spacer, damped oscillatory IL-DMI magnitude and polarity is observed in which the thickness evolution of $\boldsymbol{D}$ is well fitted by theoretical predictions. This observation directly confirmed the shared origin of RKKY and DMI due to these two interactions sharing an identical oscillation period. This behavior also contrasts the unitary behavior in structures with pure Pt spacer, analogous to the “no antiferromagnetic coupling” of Pt in the RKKY scenario [12].

I believe my results in this chapter not only enriches the physical understanding of IL-DMI, but also provides numerous pathways to utilize this effect, either by azimuthal engineering, or by exploiting the oscillating IL-DMI when mediated by proper spacers such as Ru. For example, the current-induced SOT switching’s switching polarity can be controlled by the combination of these pathways.

doi:10.6342/NTU202404434

Chapter 5 CONCLUSIONS

The central focus of this thesis is the investigations into various characteristics of the IL-DMI. These findings hold significant potential for application in future SOT or STT-MRAM devices (or even in potential 3D spin logics), akin to the indispensable role RKKY effect now serves in the design of cutting-edge magnetic memory technology.

In the initial section, by using oblique angle deposition in a type-T magnetic system with orthogonal magnetizations, we first observed IL-DMI, in which the antisymmetric effective fields in the form of a cross product between the two magnetizations are confirmed thru an angle-dependent field-sweep procedure. The reciprocity of IL-DMI is confirmed by individually focusing on the PMA or IMA layer's hysteresis behavior, captured by electrical and optical techniques, respectively, and with mutually confirming energy density. Notably, the IL-DMI's characteristic $\boldsymbol{D}$ vector is determined by the symmetry-breaking direction as dictated by the atom flow orientation from the wedge deposition, agreeing with theoretical predictions. Furthermore, we demonstrate potential usage of IL-DMI in practical devices by achieving field-free switching of a PMA layer. The critical role of IL-DMI in this process is first experimentally confirmed by capturing the coherent switching behavior of both PMA and IMA layers.

In the second section, it is revealed that due to the oblique angle deposition process used to create wedge structures, IL-DMI and tilted magnetic anisotropy coexist in our samples. Their repetitive effective fields are separated by exploiting the saturating H_{DMI} when the IMA magnetization is fully aligned by an in-plane field. IL-DMI and tilted magnetic anisotropy's respective contributions to field-free switching behavior are further scrutinized. It's observed that H_{DMI}'s magnitude reduces as the $[\mathrm{Pt/Co}]_n$ stacking

doi:10.6342/NTU202404434

number, n, increases, in contrast to the gradually increasing tilting angle of the tilted magnetic anisotropy. This trend is in good coherence with the reduced switching percentage of the PMA layer as n increases, suggesting that field-free switching is governed by IL-DMI between the PMA and IMA layers.

In addition to the competition between these two symmetry-breaking effects, the possibility of using an in-situ H_{ext} during sample growth to generate sufficient symmetry-breaking is explored. Contrary to previous reports, our results reveal that while both oblique angle deposition and H_{ext} application during growth induce deterministic UMA in the IMA layer, the corresponding IL-DMI strength from the in-situ H_{ext} is extremely weak and notably possesses random $\boldsymbol{D}$ directions. It's proposed that UMA could merely be a byproduct of H_{ext} and, therefore, limited causality exists between UMA and IL-DMI generation. These results call into question the feasibility of using in-situ H_{ext} to generate IL-DMI. Future investigations are needed to further clarify the underlying mechanisms.

Some of the more important discoveries are made in the last part of my research. By individually focusing on different layers grown with oblique angle deposition, we revealed the overall magnitude and direction of IL-DMI is dictated by the linear combination of individual contributions from discrete layers. This trait is effectively leveraged through adequately designed wedge combinations for tuning and maximizing of the IL-DMI strength. Most crucially, we developed a toy model by modifying the Fert-Lévy three site model, and by incorporating the physical picture of the template effect and self-shadow effect, our toy model effectively accounts for the opposite $\boldsymbol{D}$ directions from different wedged layers, and adequately incorporates the additivity of contributions from discrete layers. In addition, our model predicts a monotonic increase of the IL-DMI magnitude as the atomic shift rises, which is experimentally confirmed by varying the deposition angles. Leveraging these results, I demonstrated a "self-counter wedge"

doi:10.6342/NTU202404434

method to achieve improved uniformity in field-free switching characteristics, showcasing improvement that's beneficial for potential industrial adoption.

Last but certainly not least, by adding a Ru layer into the spacer, we experimentally observed damped oscillation of IL-DMI, where the ***D*** direction switches periodically with Ru thickness. The extracted oscillation period is ≈ 0.96 nm, in good agreement with the 1.15 nm reported in the 1990s on RKKY interaction. This result is a direct confirmation that IL-DMI is indeed an additional term of RKKY, a call out to distant theoretic predictions made by Smith, Fert and Lévy, and also serves as an alternative pathway to harness the strength and polarity of IL-DMI by spacer thickness, alongside wedge control.

Overall, this thesis reveals advancements in the understanding of the IL-DMI. Innovative pathways to controlling this novel effect are developed while simultaneously providing a comprehensive overview of the physical mechanism that generates IL-DMI. It'd be most exciting to see whether these advancements in IL-DMI could be employed in future spintronic devices. An overview of these discoveries is benchmarked in Table 2.

Spacer system	Symmetry breaking	***D*** direction	Exchange strength	comment
Double PMA			H_{DMI} (Oe) / H_{in} = 200 Oe	
Ru	Counter-wedge growth	⊥Symmetry breaking, unitary	270	***D*** engineering strategies, Field-free switching, improved homogeneity
Type-T			E_{DMI} (μJ/m^2)	
Pt	Counter-wedge growth	⊥Symmetry breaking, unitary	28.4	***D*** engineering strategies, Field-free switching
Pt	Wedge growth	⊥Symmetry breaking, unitary	13.1	*D* vs. tilted anisotropy
Pt/Ru	Wedge growth	⊥Symmetry breaking, oscillatory	31.2	RKKY type ***D*** oscillation

Table 2 Benchmarking my works on IL-DMI.

doi:10.6342/NTU202404434

Chapter 6 Appendix: Sample Preparations

6.1 Magnetron Sputtering

Throughout this work, the magnetron sputtering technique is employed to deposit thin films onto the Si/SiO_2 substrate. Magnetron sputtering is a physical vapor deposition technique, widely adopted in industry to prepare nanometer thick thin films due to its ability to produce homogeneous, precise films. Within this process, Ar working gas within the chamber is ionized by a voltage between the target and the substrate, forming Ar plasma. The Ar^+ ions then strike the target material, ejecting atoms to be sputtered onto the substrate to form thin films, as graphically depicted in Fig. 6-1(a) (top). Importantly, the addition of strong magnets in magnetron sputtering creates magnetic field lines that guide the trajectory of electrons (therefore the plasma) released by the cathode due to the applied voltage to be confined to the region near the target, therefore increasing the sputtering efficiency (Fig. 6-1(a) (bottom).

Apart from these standard practices of operating the sputtering process, the in-plane symmetry breaking is achieved by disabling the sample holder's rotation during the deposition of specific layers. This can be done via the rotation motor's interface, and by taking into account the sputter gun's relative orientation with regard to the substrate, a clearly defined wedge deposition direction can be well controlled, as depicted in Fig. 6-1(b). In addition, the incident angle θ_{incident} between the sputter atom flow and the substrate's plane normal can be tuned by the lift control that facilitates the up-and-down movement of the sample holder. This provides a θ_{incident} tuning range of 20° to 70° (as shown in Fig. 6-1(b)), though the sputter rate must be individually calibrated for each

θ_{incident} due to the varied distance between the target guns and the substrate.

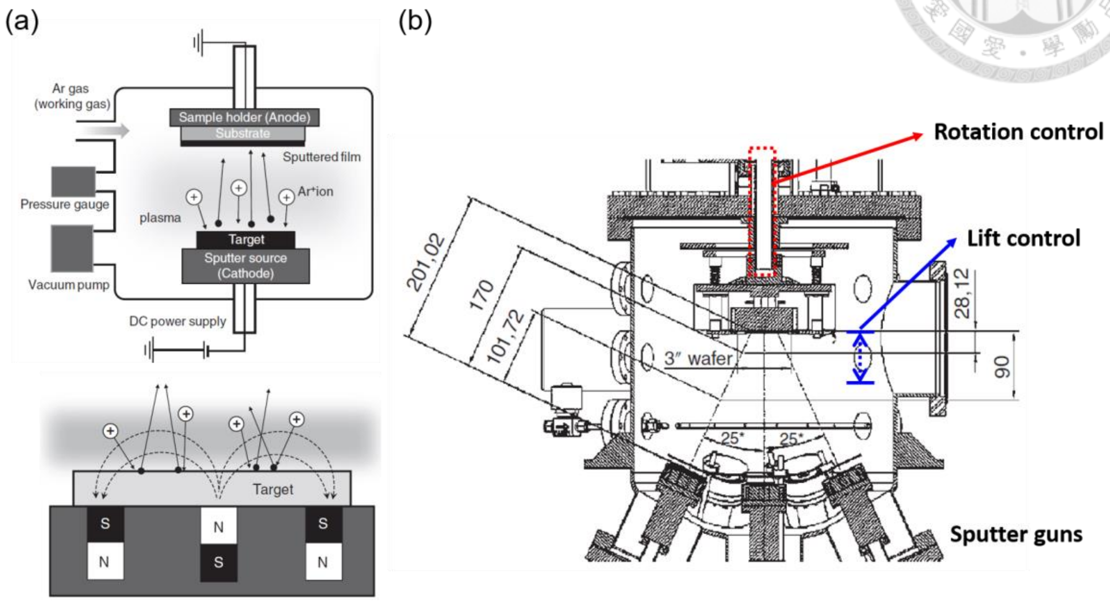

Fig. 6-1 (a) Top: demonstration of the basic workings of a typical magnetron sputtering system. Bottom: The magnetic field lines created from magnets under the sputter target (thus “magnetron”) guides the trajectory of the Ar plasma, making the plasma more localized near the target, thus increasing deposition efficiency. Adopted from [2].(b) Schematics of the multi-gun sputtering system utilized to grow the various samples used throughout this thesis. By changing two key parameters, the relative azimuthal orientation between specific sputter target (predominantly Pt) and the Hall bar devices, and the incident angle can be tuned by the rotational control and lift control, respectively.

6.2 Photolithography and device patterns

Aside from the sputtering procedure, the actual devices are patterned via photolithography lift-off process. Photolithography is at the heart of numerous industries such as semiconductors, microelectronics or micro electro mechanical systems (MEMS). Photolithography starts by coating a substrate with a light-sensitive photoresist, which can be either positive or negative. Exposure to light causes the exposed photoresist to undergo chemical reaction. In the case of a positive photoresist, the bonds of the polymer in the exposed region break down and becomes more soluble and could therefore be washed away via a developer solution. On the other hand, the materials within a negative photoresist undergoes a polymerize process after exposure to light, while the unexposed region can be washed away by the developer solution. Within this thesis, the sample geometry is always patterned via a negative photoresist. The schematics of the core pattern of a standard Hall bar device is illustrated in Fig. 6-2(b), while a complete device geometry is sketched in Fig. 6-2(c) where the pattern of the outer electrode pads is also included.

The graphical representation of the photolithography lift-off process is illustrated in Fig. 6-2(a), and the preparation flow is as follows:

1. **Substrate cleaning:** Broken wafer typically with a dimension of 1 × 1 cm is cleaned by ultrasonic vibration while immersed in isopropanol. It’s then pre-baked at 100° C for 100 sec to remove possible water molecules.
2. **Spin coating:** the negative photoresist is coated by a spin coater. This is a two-step process where a 1000 rpm rotation is applied for 10 seconds, followed by a 3000 rotation for 30 seconds. The thickness of the spin coated photoresist is in the order

doi:10.6342/NTU202404434

of several μm.

3. **UV light exposure:** The thin film coated with photoresist first undergoes the prebake process of 100° C for 100 seconds to remove the solvent in the photoresist. Then, UV light exposure is performed, while using a photomask to pattern the desired geometry (Fig. 6-2(c)). The UV wavelength is ~360 nm, and the exposure time ranges from 2 to 5 seconds, depending on the instrument conditions.
4. **Development:** Using a developer (TMAH 2.38%), the photoresist of the unexposed area is washed away in about 30 seconds. This step corresponds to the situation as described by Fig. 6-2(b) right after photoresist patterning. After this step, it's now ready to fill materials into the lift-off pattern via sputtering.
5. **Sputter growth:** Deposition is done by directly deposition onto the substrates with pre-fabricated lift-off patterns, where the empty Hall bar region can be filled.
6. **Photoresist stripping:** After the sputter growth step, the whole film is uniformly deposited with materials (as shown in Fig. 6-2(a) sputter deposition). By placing the sample in Acetone which dissolves all photoresist, the materials that are grown on top of the photoresist will be removed as well, leaving our desired Hall bar patterns intact on the substrate.

After finishing the photolithography and sputtering process, the remaining pattern is a set of rotary Hall bars as shown in Fig. 6-2(c). These patterns are the basis for most measurements within this thesis, performed by 4-point probe measurements where the probes are placed on the electrode pads (olive colored).

doi:10.6342/NTU202404434

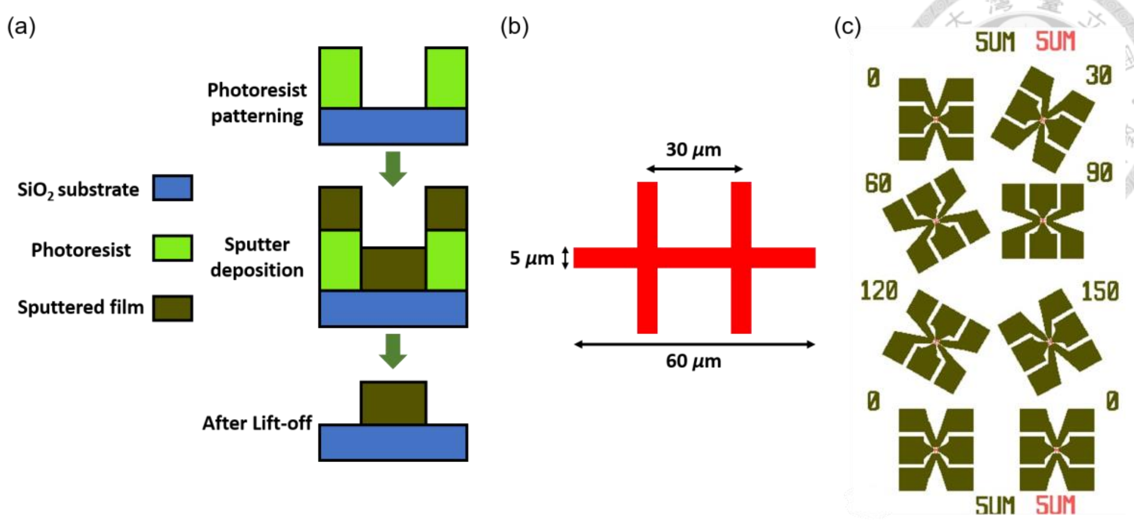

Fig. 6-2 Schematics of the Hall bar devices fabricated from photolithography processes + sputtering. (a) Graphical representation of the photolithography (lift-off) procedure to prepare samples, in conjunction with sputter deposition. (b) The central Hall bar (cross) device geometry. (c) Rotating devices with 30 degrees intervals prepared by the lift-off process described in (b). Note that the Hall bars can be seen at the center of individual devices (red colored), and the outer pads (olive colored) serve as electrode pads for 4-point probe measurements.

REFERENCE

[1] C. M. Hurd, Varieties of magnetic order in solids, Contemp. Phys. **23**, 469 (2006).

[2] D. T. Denny and P. Chi-Feng, Magnetism and Magnetic Materials, (2021)

[3] S. Blundell, Magnetism in condensed matter, (2001)

[4] V. Chaudhary and R. V. Ramanujan, Magnetocaloric Properties of Fe-Ni-Cr Nanoparticles for Active Cooling, Sci. Rep. **6**, 35156 (2016).

[5] R. O'handley, Modern magnetic materials, (2000)

[6] J. B. Goodenough, Theory of the Role of Covalence in the Perovskite-Type Manganites[La, M(II)]MnO3, Phys. Rev. **100**, 564 (1955).

[7] M. A. Ruderman and C. Kittel, Indirect Exchange Coupling of Nuclear Magnetic Moments by Conduction Electrons, Phys. Rev. **96**, 99 (1954).

[8] T. Kasuya, A Theory of Metallic Ferro- and Antiferromagnetism on Zener's Model, Prog. Theor. Phys. **16**, 45 (1956).

[9] K. Yosida, Magnetic Properties of Cu-Mn Alloys, Phys. Rev. **106**, 893 (1957).

[10] S. H. Schoenmaker, The interlayer Dzyaloshinskii-Moriya interaction, 2021.

[11] J. Wei, X. Wang, B. Cui, C. Guo, H. Xu, Y. Guang, Y. Wang, X. Luo, C. Wan, J. Feng *et al.*, Field-Free Spin–Orbit Torque Switching in Perpendicularly Magnetized Synthetic Antiferromagnets, Adv. Funct. Mater. **32** (2021).

[12] S. S. Parkin, Systematic variation of the strength and oscillation period of indirect magnetic exchange coupling through the 3d, 4d, and 5d transition metals, Phys. Rev. Lett. **67**, 3598 (1991).

[13] S. Yuasa, Introduction to Magnetic Random-Access Memory, (2017), p. 29.

[14] I. Dzyaloshinsky, A thermodynamic theory of ‘weak’ ferromagnetism of antiferromagnetics, J. Phys. Chem. Sol. **4**, 241 (1957).

doi:10.6342/NTU202404434

[15] T. Moriya, Anisotropic Superexchange Interaction and Weak Ferromagnetism, Phys. Rev. **120**, 91 (1960).

[16] A. Fert, M. Chshiev, A. Thiaville, and H. Yang, From Early Theories of Dzyaloshinskii–Moriya Interactions in Metallic Systems to Today's Novel Roads, J. Phys. Soc. Jpn. **92**, 081001 (2023).

[17] D. A. Smith, New mechanisms for magnetic anisotropy in localised S-state moment materials, J. Magn. Magn. Mater. **1**, 214 (1976).

[18] K. Wang, K. Ren, Y. Cheng, S. Chen, and G. Zhang, The impacts of molecular adsorption on antiferromagnetic MnPS3 monolayers: enhanced magnetic anisotropy and intralayer Dzyaloshinskii–Moriya interaction, Materials Horizons **9**, 2384 (2022).

[19] J. C. Slonczewski, Current-driven excitation of magnetic multilayers, J. Magn. Magn. Mater. **159**, L1 (1996).

[20] J. C. Sankey, Y.-T. Cui, J. Z. Sun, J. C. Slonczewski, R. A. Buhrman, and D. C. Ralph, Measurement of the spin-transfer-torque vector in magnetic tunnel junctions, Nat. Phys. **4**, 67 (2008).

[21] I. M. Miron, K. Garello, G. Gaudin, P.-J. Zermatten, M. V. Costache, S. Auffret, S. Bandiera, B. Rodmacq, A. Schuhl, and P. Gambardella, Perpendicular switching of a single ferromagnetic layer induced by in-plane current injection, Nature **476**, 189 (2011).

[22] S. Emori, U. Bauer, S. M. Ahn, E. Martinez, and G. S. Beach, Current-driven dynamics of chiral ferromagnetic domain walls, Nat. Mater. **12**, 611 (2013).

[23] S. S. P. Parkin, M. Hayashi, and L. Thomas, Magnetic Domain-Wall Racetrack Memory, Science **320**, 190 (2008).

[24] S. Parkin and S. H. Yang, Memory on the racetrack, Nat. Nanotechnol. **10**, 195 (2015).

[25] A. Fert, V. Cros, and J. Sampaio, Skyrmions on the track, Nat. Nanotechnol. **8**, 152

doi:10.6342/NTU202404434

(2013).

[26] F. Kammerbauer, F. Freimuth, R. Frömter, Y. Mokrousov, and M. Kläui, Dzyaloshinskii–Moriya Interaction and Its Current-Induced Manipulation, J. Phys. Soc. Jpn. **92** (2023).

[27] N. Nagaosa, J. Sinova, S. Onoda, A. H. MacDonald, and N. P. Ong, Anomalous Hall effect, Rev. Mod. Phys. **82**, 1539 (2010).

[28] M. Hayashi, J. Kim, M. Yamanouchi, and H. Ohno, Quantitative characterization of the spin-orbit torque using harmonic Hall voltage measurements, Phys. Rev. B **89**, 144425 (2014).

[29] M.-H. Nguyen and C.-F. Pai, Spin–orbit torque characterization in a nutshell, APL Materials **9** (2021).

[30] D. Maryenko, A. S. Mishchenko, M. S. Bahramy, A. Ernst, J. Falson, Y. Kozuka, A. Tsukazaki, N. Nagaosa, and M. Kawasaki, Observation of anomalous Hall effect in a non-magnetic two-dimensional electron system, Nat. Comm. **8**, 14777 (2017).

[31] C. O. Avci, Current-induced effects in ferromagnetic heterostructures due to spin-orbit coupling, 2015.

[32] M. Manfrini, Spin orbit torques in magnetic materials, 2017.

[33] A. Hoffmann, Spin Hall Effects in Metals, IEEE Transactions on Magnetics **49**, 5172 (2013).

[34] C. Stamm, C. Murer, M. Berritta, J. Feng, M. Gabureac, P. M. Oppeneer, and P. Gambardella, Magneto-Optical Detection of the Spin Hall Effect in Pt and W Thin Films, Phys. Rev. Lett. **119**, 087203 (2017).

[35] T. Tanaka, H. Kontani, M. Naito, T. Naito, D. S. Hirashima, K. Yamada, and J. Inoue, Intrinsic spin Hall effect and orbital Hall effect in4dand5dtransition metals, Phys. Rev. B **77** (2008).

doi:10.6342/NTU202404434

[36] L. Liu, C.-F. Pai, Y. Li, H. W. Tseng, D. C. Ralph, and R. A. Buhrman, Spin-Torque Switching with the Giant Spin Hall Effect of Tantalum, Science **336**, 555 (2012).

[37] C. O. Avci, K. Garello, A. Ghosh, M. Gabureac, S. F. Alvarado, and P. Gambardella, Unidirectional spin Hall magnetoresistance in ferromagnet/normal metal bilayers, Nat. Phys. **11**, 570 (2015).

[38] Y.-T. Liu, T.-Y. Chen, T.-H. Lo, T.-Y. Tsai, S.-Y. Yang, Y.-J. Chang, J.-H. Wei, and C.-F. Pai, Determination of Spin-Orbit-Torque Efficiencies in Heterostructures with In-Plane Magnetic Anisotropy, Phys. Rev. Appl. **13**, 044032 (2020).

[39] Y.-T. Liu, Y.-H. Huang, C.-C. Huang, Y.-C. Li, C.-L. Cheng, and C.-F. Pai, Field-Free Type-x Spin-Orbit-Torque Switching by Easy-Axis Engineering, Phys. Rev. Appl. **18**, 034019 (2022).

[40] M. Ali, Growth And Study Of Magnetostrictive FeSiBC Thin Films For Device Applications, (1999).

[41] Z. Q. Qiu and S. D. Bader, Surface magneto-optic Kerr effect, Review of Scientific Instruments **71**, 1243 (2000).

[42] D. A. Allwood, G. Xiong, M. D. Cooke, and R. P. Cowburn, Magneto-optical Kerr effect analysis of magnetic nanostructures, J. Phys. D: Appl. Phys. **36**, 2175 (2003).

[43] J. Hamrle, Magneto-optical Kerr effect (MOKE), 17 (2014).

[44] M. Montazeri, P. Upadhyaya, M. C. Onbasli, G. Q. Yu, K. L. Wong, M. R. Lang, Y. B. Fan, X. Li, P. K. Amiri, R. N. Schwartz *et al.*, Magneto-optical investigation of spin-orbit torques in metallic and insulating magnetic heterostructures, Nat. Comm. **6** (2015).

[45] H. Huang, H. Wu, T. Yu, Q. Pan, B. Dai, A. Razavi, K. Wong, B. Cui, S. K. Chong, and D. Wu, Electrical and optical characterizations of spin-orbit torque, Appl. Phys. Lett. **118**, 072405 (2021).

[46] A. Fert and P. M. Levy, Role of Anisotropic Exchange Interactions in Determining

the Properties of Spin-Glasses, Phys. Rev. Lett. **44**, 1538 (1980).

[47] G. Yu, P. Upadhyaya, K. L. Wong, W. Jiang, J. G. Alzate, J. Tang, P. K. Amiri, and K. L. Wang, Magnetization switching through spin-Hall-effect-induced chiral domain wall propagation, Phys. Rev. B **89**, 104421 (2014).

[48] T. P. Dao, M. Muller, Z. Luo, M. Baumgartner, A. Hrabec, L. J. Heyderman, and P. Gambardella, Chiral Domain Wall Injector Driven by Spin-Orbit Torques, Nano Lett. **19**, 5930 (2019).

[49] A. Soumyanarayanan, M. Raju, A. L. Gonzalez Oyarce, A. K. C. Tan, M. Y. Im, A. P. Petrovic, P. Ho, K. H. Khoo, M. Tran, C. K. Gan *et al.*, Tunable room-temperature magnetic skyrmions in Ir/Fe/Co/Pt multilayers, Nat. Mater. **16**, 898 (2017).

[50] C. Moreau-Luchaire, S. C. Mouta, N. Reyren, J. Sampaio, C. A. Vaz, N. Van Horne, K. Bouzehouane, K. Garcia, C. Deranlot, P. Warnicke *et al.*, Additive interfacial chiral interaction in multilayers for stabilization of small individual skyrmions at room temperature, Nat. Nanotechnol. **11**, 444 (2016).

[51] J. H. Franken, M. Herps, H. J. Swagten, and B. Koopmans, Tunable chiral spin texture in magnetic domain-walls, Sci. Rep. **4**, 5248 (2014).

[52] E. Y. Vedmedenko, P. Riego, J. A. Arregi, and A. Berger, Interlayer Dzyaloshinskii-Moriya Interactions, Phys. Rev. Lett. **122**, 257202 (2019).

[53] Y.-H. Huang, C.-C. Huang, W.-B. Liao, T.-Y. Chen, and C.-F. Pai, Growth-Dependent Interlayer Chiral Exchange and Field-Free Switching, Phys. Rev. Appl. **18**, 034046 (2022).

[54] A. N. Bogdanov and U. K. Rossler, Chiral symmetry breaking in magnetic thin films and multilayers, Phys. Rev. Lett. **87**, 037203 (2001).

[55] M. Bode, M. Heide, K. von Bergmann, P. Ferriani, S. Heinze, G. Bihlmayer, A. Kubetzka, O. Pietzsch, S. Blugel, and R. Wiesendanger, Chiral magnetic order at surfaces

doi:10.6342/NTU202404434

driven by inversion asymmetry, Nature **447**, 190 (2007).

[56] S. Heinze, K. von Bergmann, M. Menzel, J. Brede, A. Kubetzka, R. Wiesendanger, G. Bihlmayer, and S. Blügel, Spontaneous atomic-scale magnetic skyrmion lattice in two dimensions, Nat. Phys. **7**, 713 (2011).

[57] J. Y. Chauleau, W. Legrand, N. Reyren, D. Maccariello, S. Collin, H. Popescu, K. Bouzehouane, V. Cros, N. Jaouen, and A. Fert, Chirality in Magnetic Multilayers Probed by the Symmetry and the Amplitude of Dichroism in X-Ray Resonant Magnetic Scattering, Phys. Rev. Lett. **120**, 037202 (2018).

[58] D. S. Han, K. Lee, J. P. Hanke, Y. Mokrousov, K. W. Kim, W. Yoo, Y. L. W. van Hees, T. W. Kim, R. Lavrijsen, C. Y. You *et al.*, Long-range chiral exchange interaction in synthetic antiferromagnets, Nat. Mater. **18**, 703 (2019).

[59] S. Liang, R. Chen, Q. Cui, Y. Zhou, F. Pan, H. Yang, and C. Song, Ruderman-Kittel-Kasuya-Yosida-Type Interlayer Dzyaloshinskii-Moriya Interaction in Synthetic Magnets, Nano Lett. **23**, 8690 (2023).

[60] Z. Wang, P. Li, M. Fattouhi, Y. Yao, Y. L. W. Van Hees, C. F. Schippers, X. Zhang, R. Lavrijsen, F. Garcia-Sanchez, E. Martinez *et al.*, Field-free spin-orbit torque switching of synthetic antiferromagnet through interlayer Dzyaloshinskii-Moriya interactions, Cell Rep. **4**, 101334 (2023).

[61] K. Wang, L. Qian, S.-C. Ying, and G. Xiao, Spin-orbit torque switching of chiral magnetization across a synthetic antiferromagnet, Commun. Phys. **4**, 10 (2021).

[62] W. He, C. Wan, C. Zheng, Y. Wang, X. Wang, T. Ma, Y. Wang, C. Guo, X. Luo, M. E. Stebliy *et al.*, Field-Free Spin-Orbit Torque Switching Enabled by the Interlayer Dzyaloshinskii-Moriya Interaction, Nano Lett. **22**, 6857 (2022).

[63] F. S. Gao, S. Q. Liu, R. Zhang, J. H. Xia, W. Q. He, X. H. Li, X. M. Luo, C. H. Wan, G. Q. Yu, G. Su *et al.*, Experimental evidence of the oscillation behavior of the

doi:10.6342/NTU202404434

interlayer DMI effect, Appl. Phys. Lett. **123**, 192401 (2023).

[64] A. Fernandez-Pacheco, E. Vedmedenko, F. Ummelen, R. Mansell, D. Petit, and R. P. Cowburn, Symmetry-breaking interlayer Dzyaloshinskii-Moriya interactions in synthetic antiferromagnets, Nat. Mater. **18**, 679 (2019).

[65] C. O. Avci, C. H. Lambert, G. Sala, and P. Gambardella, Chiral Coupling between Magnetic Layers with Orthogonal Magnetization, Phys. Rev. Lett. **127**, 167202 (2021).

[66] C.-F. Pai, M. Mann, A. J. Tan, and G. S. D. Beach, Determination of spin torque efficiencies in heterostructures with perpendicular magnetic anisotropy, Phys. Rev. B **93**, 144409 (2016).

[67] J. Torrejon, J. Kim, J. Sinha, S. Mitani, M. Hayashi, M. Yamanouchi, and H. Ohno, Interface control of the magnetic chirality in CoFeB/MgO heterostructures with heavy-metal underlayers, Nat. Comm. **5**, 4655 (2014).

[68] B. Cui, C. Song, G. Y. Wang, Y. Y. Wang, F. Zeng, and F. Pan, Perpendicular magnetic anisotropy in CoFeB/X (X=MgO, Ta, W, Ti, and Pt) multilayers, J. Alloys Compd. **559**, 112 (2013).

[69] M. Akyol, Origin of Interfacial Magnetic Anisotropy in Ta/CoFeB/MgO and Pt/CoFeB/MgO Multilayer Thin Film Stacks, J. Supercond. Nov. Magn. **32**, 457 (2019).

[70] P. F. Carcia, Perpendicular magnetic anisotropy in Pd/Co and Pt/Co thin-film layered structures, J. Appl. Phys. **63**, 5066 (1988).

[71] N. Nakajima, T. Koide, T. Shidara, H. Miyauchi, H. Fukutani, A. Fujimori, K. Iio, T. Katayama, M. Nývlt, and Y. Suzuki, Perpendicular Magnetic Anisotropy Caused by Interfacial Hybridization via Enhanced Orbital Moment in Co/Pt Multilayers: Magnetic Circular X-Ray Dichroism Study, Phys. Rev. Lett. **81**, 5229 (1998).

[72] C.-C. Huang, C.-C. Tsai, W.-B. Liao, T.-Y. Chen, and C.-F. Pai, Deep learning for spin-orbit torque characterizations with a projected vector field magnet, Phys. Rev. Res.

4, 033040 (2022).

[73] R. Shindou, J.-i. Ohe, R. Matsumoto, S. Murakami, and E. Saitoh, Chiral spin-wave edge modes in dipolar magnetic thin films, Phys. Rev. B **87**, 174402 (2013).

[74] K. S. Ryu, L. Thomas, S. H. Yang, and S. Parkin, Chiral spin torque at magnetic domain walls, Nat. Nanotechnol. **8**, 527 (2013).

[75] C.-Y. Hu, Y.-F. Chiu, C.-C. Tsai, C.-C. Huang, K.-H. Chen, C.-W. Peng, C.-M. Lee, M.-Y. Song, Y.-L. Huang, S.-J. Lin *et al.*, Toward 100% Spin–Orbit Torque Efficiency with High Spin–Orbital Hall Conductivity Pt–Cr Alloys, ACS Appl. Electron. Mater. **4**, 1099 (2022).

[76] V. M. P, K. R. Ganesh, and P. S. A. Kumar, Spin Hall effect mediated current-induced deterministic switching in all-metallic perpendicularly magnetized Pt/Co/Pt trilayers, Phys. Rev. B **96**, 104412 (2017).

[77] H. J. Kim, K. W. Moon, B. X. Tran, S. Yoon, C. Kim, S. Yang, J. H. Ha, K. An, T. S. Ju, J. I. Hong *et al.*, Field-Free Switching of Magnetization by Tilting the Perpendicular Magnetic Anisotropy of Gd/Co Multilayers, Adv. Funct. Mater. **32**, 2112561 (2022).

[78] H. F. Ding, S. Pütter, H. P. Oepen, and J. Kirschner, Experimental method for separating longitudinal and polar Kerr signals, J. Magn. Magn. Mater. **212**, 5 (2000).

[79] C.-Y. Hu, W.-D. Chen, Y.-T. Liu, C.-C. Huang, and C.-F. Pai, The Central Role of Tilted Anisotropy for Field-Free Spin-Orbit Torque Switching of Perpendicular Magnetization, arXiv e-prints, arXiv:2306.06357 (2023).

[80] S. Emori, E. Martinez, K.-J. Lee, H.-W. Lee, U. Bauer, S.-M. Ahn, P. Agrawal, D. C. Bono, and G. S. D. Beach, Spin Hall torque magnetometry of Dzyaloshinskii domain walls, Phys. Rev. B **90** (2014).

[81] J. Ryu, R. Thompson, J. Y. Park, S.-J. Kim, G. Choi, J. Kang, H. B. Jeong, M. Kohda, J. M. Yuk, J. Nitta *et al.*, Efficient spin–orbit torque in magnetic trilayers using

doi:10.6342/NTU202404434

all three polarizations of a spin current, Nat. Electron. **5**, 217 (2022).

[82] H. Wu, J. Zhang, B. Cui, S. A. Razavi, X. Che, Q. Pan, D. Wu, G. Yu, X. Han, and K. L. Wang, Field-free approaches for deterministic spin–orbit torque switching of the perpendicular magnet, Mater. Futures **1** (2022).

[83] W. L. Yang, Z. R. Yan, Y. W. Xing, C. Cheng, C. Y. Guo, X. M. Luo, M. K. Zhao, G. Q. Yu, C. H. Wan, M. E. Stebliy *et al.*, Role of an in-plane ferromagnet in a T-type structure for field-free magnetization switching, Appl. Phys. Lett. **120**, 122402 (2022).

[84] H. Wu, J. Nance, S. A. Razavi, D. Lujan, B. Dai, Y. Liu, H. He, B. Cui, D. Wu, K. Wong *et al.*, Chiral Symmetry Breaking for Deterministic Switching of Perpendicular Magnetization by Spin–Orbit Torque, Nano Lett. **21**, 515 (2021).

[85] F. Wang, X. Zhang, Z. Zhang, and Y. Liu, Deterministic magnetization switching by spin–orbit torque in a ferromagnet with tilted magnetic anisotropy: A macrospin modeling, J. Magn. Magn. Mater. **527**, 167757 (2021).

[86] C.-Y. Hu, W.-D. Chen, Y.-T. Liu, C.-C. Huang, and C.-F. Pai, The central role of tilted anisotropy for field-free spin–orbit torque switching of perpendicular magnetization, NPG Asia Mater. **16** (2024).

[87] Y. C. Lau, D. Betto, K. Rode, J. M. Coey, and P. Stamenov, Spin-orbit torque switching without an external field using interlayer exchange coupling, Nat. Nanotechnol. **11**, 758 (2016).

[88] Y. W. Oh, S. H. Chris Baek, Y. M. Kim, H. Y. Lee, K. D. Lee, C. G. Yang, E. S. Park, K. S. Lee, K. W. Kim, G. Go *et al.*, Field-free switching of perpendicular magnetization through spin-orbit torque in antiferromagnet/ferromagnet/oxide structures, Nat. Nanotechnol. **11**, 878 (2016).

[89] A. van den Brink, G. Vermijs, A. Solignac, J. Koo, J. T. Kohlhepp, H. J. M. Swagten, and B. Koopmans, Field-free magnetization reversal by spin-Hall effect and exchange

doi:10.6342/NTU202404434

bias, Nat. Comm. **7**, 10854 (2016).

[90] L. Liu, C. Zhou, X. Shu, C. Li, T. Zhao, W. Lin, J. Deng, Q. Xie, S. Chen, J. Zhou *et al.*, Symmetry-dependent field-free switching of perpendicular magnetization, Nat. Nanotechnol. **16**, 277 (2021).

[91] S. Fukami, T. Anekawa, C. Zhang, and H. Ohno, A spin-orbit torque switching scheme with collinear magnetic easy axis and current configuration, Nat. Nanotechnol. **11**, 621 (2016).

[92] T.-Y. Tsai, T.-Y. Chen, C.-T. Wu, H.-I. Chan, and C.-F. Pai, Spin-orbit torque magnetometry by wide-field magneto-optical Kerr effect, Sci. Rep. **8**, 5613 (2018).

[93] N. Murray, W.-B. Liao, T.-C. Wang, L.-J. Chang, L.-Z. Tsai, T.-Y. Tsai, S.-F. Lee, and C.-F. Pai, Field-free spin-orbit torque switching through domain wall motion, Phys. Rev. B **100**, 104441 (2019).

[94] E. Y. Vedmedenko, R. K. Kawakami, D. D. Sheka, P. Gambardella, A. Kirilyuk, A. Hirohata, C. Binek, O. Chubykalo-Fesenko, S. Sanvito, B. J. Kirby *et al.*, The 2020 magnetism roadmap, J. Phys. D: Appl. Phys. **53** (2020).

[95] Z. Luo, A. Hrabec, T. P. Dao, G. Sala, S. Finizio, J. Feng, S. Mayr, J. Raabe, P. Gambardella, and L. J. Heyderman, Current-driven magnetic domain-wall logic, Nature **579**, 214 (2020).

[96] T. P. D. Zhaochu Luo, AlešHrabec, Jaianth Vijayakumar, Armin Kleibert, Manuel Baumgartner, Eugenie Kirk, Jizhai Cui, Tatiana Savchenko, Gunasheel Krishnaswamy, Laura J. Heyderman, Pietro Gambardella, Chirally couped nanomagnets, Science **363** (2019).

[97] Y.-C. Li, Y.-H. Huang, C.-C. Huang, Y.-T. Liu, and C.-F. Pai, Field-Free Switching in Symmetry-Breaking Multilayers: The Critical Role of Interlayer Chiral Exchange, Phys. Rev. Appl. **20**, 024036 (2023).

[98] J. Torrejon, F. Garcia-Sanchez, T. Taniguchi, J. Sinha, S. Mitani, J.-V. Kim, and M. Hayashi, Current-driven asymmetric magnetization switching in perpendicularly magnetized CoFeB/MgO heterostructures, Phys. Rev. B **91** (2015).

[99] H. Masuda, T. Seki, Y. Yamane, R. Modak, K.-i. Uchida, J. i. Ieda, Y.-C. Lau, S. Fukami, and K. Takanashi, Large Antisymmetric Interlayer Exchange Coupling Enabling Perpendicular Magnetization Switching by an In-Plane Magnetic Field, Phys. Rev. Appl. **17**, 054036 (2022).

[100] K. P. T. J. Klemmer, Seed layer control for tilted magnetic recording media, Appl. Phys. Lett. **88**, 162507 (2006).

[101] C. Li, G. Chai, C. Yang, W. Wang, and D. Xue, Tunable zero-field ferromagnetic resonance frequency from S to X band in oblique deposited CoFeB thin films, Sci. Rep. **5**, 17023 (2015).

[102] Y. H. Huang, J. H. Han, W. B. Liao, C. Y. Hu, Y. T. Liu, and C. F. Pai, Tailoring Interlayer Chiral Exchange by Azimuthal Symmetry Engineering, Nano Lett. **24**, 649 (2024).

[103] J. A. Arregi, P. Riego, A. Berger, and E. Y. Vedmedenko, Large interlayer Dzyaloshinskii-Moriya interactions across Ag-layers, Nat. Comm. **14**, 6927 (2023).

[104] S. Chen, D. Li, B. Cui, L. Xi, M. Si, D. Yang, and D. Xue, Temperature dependence of spin–orbit torques in Pt/Co/Pt multilayers, J. Phys. D: Appl. Phys. **51** (2018).

[105] F. Kammerbauer, W. Y. Choi, F. Freimuth, K. Lee, R. Fromter, D. S. Han, R. Lavrijsen, H. J. M. Swagten, Y. Mokrousov, and M. Klaui, Controlling the Interlayer Dzyaloshinskii-Moriya Interaction by Electrical Currents, Nano Lett. **23**, 7070 (2023).

[106] A. Barranco, A. Borras, A. R. Gonzalez-Elipe, and A. Palmero, Perspectives on oblique angle deposition of thin films: From fundamentals to devices, Prog. Mater. Sci.

doi:10.6342/NTU202404434

76, 59 (2016).

[107] H. Hajihoseini, M. Kateb, S. Ingvarsson, and J. T. Gudmundsson, Oblique angle deposition of nickel thin films by high-power impulse magnetron sputtering, Beilstein J. Nanotechnol **10**, 1914 (2019).

[108] L. González-García, I. González-Valls, M. Lira-Cantu, A. Barranco, and A. R. González-Elipe, Aligned TiO2 nanocolumnar layers prepared by PVD-GLAD for transparent dye sensitized solar cells, Energy Environ. Sci. **4** (2011).

[109] T. C. Chuang, C. F. Pai, and S. Y. Huang, Cr-induced Perpendicular Magnetic Anisotropy and Field-Free Spin-Orbit-Torque Switching, Phys. Rev. Appl. **11**, 016005 (2019).

[110] H. Chu, S. Song, C. Li, and D. Gibson, Surface Enhanced Raman Scattering Substrates Made by Oblique Angle Deposition: Methods and Applications, Coatings **7** (2017).

[111] K. Garello, I. M. Miron, C. O. Avci, F. Freimuth, Y. Mokrousov, S. Blugel, S. Auffret, O. Boulle, G. Gaudin, and P. Gambardella, Symmetry and magnitude of spin-orbit torques in ferromagnetic heterostructures, Nat Nanotechnol **8**, 587 (2013).

[112] R. H. Koch, J. A. Katine, and J. Z. Sun, Time-resolved reversal of spin-transfer switching in a nanomagnet, Phys. Rev. Lett. **92**, 088302 (2004).

[113] B. Dieny and M. Chshiev, Perpendicular magnetic anisotropy at transition metal/oxide interfaces and applications, Rev. Mod. Phys. **89** (2017).

[114] W.-B. Liao, T.-Y. Chen, Y.-C. Hsiao, and C.-F. Pai, Pulse-width and temperature dependence of memristive spin–orbit torque switching, Appl. Phys. Lett. **117** (2020).

[115] S. Jaiswal, K. Lee, J. Langer, B. Ocker, M. Kläui, and G. Jakob, Tuning of interfacial perpendicular magnetic anisotropy and domain structures in magnetic thin film

doi:10.6342/NTU202404434

multilayers, J. Phys. D: Appl. Phys. **52** (2019).

[116] T. Liu, J. W. Cai, and L. Sun, Large enhanced perpendicular magnetic anisotropy in CoFeB/MgO system with the typical Ta buffer replaced by an Hf layer, AIP Advances **2** (2012).

[117] T.-C. Wang, T.-Y. Chen, C.-T. Wu, H.-W. Yen, and C.-F. Pai, Comparative study on spin-orbit torque efficiencies from W/ferromagnetic and W/ferrimagnetic heterostructures, Phys. Rev. Mater. **2** (2018).

[118] W.-B. Liao, T.-Y. Chen, Y. Ferrante, S. S. P. Parkin, and C.-F. Pai, Current-Induced Magnetization Switching by the High Spin Hall Conductivity α-W, Phys. Status Solidi RRL **13** (2019).

[119] W. Skowroński, Ł. Karwacki, S. Ziętek, J. Kanak, S. Łazarski, K. Grochot, T. Stobiecki, P. Kuświk, F. Stobiecki, and J. Barnaś, Determination of Spin Hall Angle in Heavy-Metal/Co−Fe−B-Based Heterostructures with Interfacial Spin-Orbit Fields, Phys. Rev. Appl. **11** (2019).

[120] X. W. Zhou and H. N. G. Wadley, Atomistic simulation of the vapor deposition of Ni/Cu/Ni multilayers: Incident adatom angle effects, J. Appl. Phys. **87**, 553 (2000).

[121] C. Sun, Y. Jiao, C. Zuo, X. Hu, Y. Tao, F. Jin, W. Mo, Y. Hui, J. Song, and K. Dong, Field-free switching of perpendicular magnetization through spin-orbit torque in FePt/[TiN/NiFe](5) multilayers, Nanoscale **13**, 18293 (2021).

[122] S. S. Parkin and D. Mauri, Spin engineering: Direct determination of the Ruderman-Kittel-Kasuya-Yosida far-field range function in ruthenium, Phys. Rev. B **44**, 7131 (1991).